An Approach to NLO QCD Analysis of the Semi-Inclusive DIS Data with the Modified Jacobi Polynomial Expansion Method[¶]

A. N. Sissakian, O. Yu. Shevchenko*, and O. N. Ivanov

Joint Institute for Nuclear Research, Dubna, 141980 Russia
**e-mail: shev@mail.cern.ch*
Received May 17, 2005; in final form, June 6, 2005

The modification of the Jacobi polynomial expansion method (MJEM) is proposed on the basis of the application of the truncated moments instead of the full ones. This allows us to reconstruct the local quark helicity distributions with high precision even for the narrow Bjorken x region accessible for measurement, using as an input only the four first moments extracted from the data in the next to leading order QCD. The variational (extrapolation) procedure is also proposed allowing us to reconstruct the distributions outside the accessible Bjorken x region using the distributions obtained with MJEM in the accessible region. The numerical calculations encourage one that the proposed variational (extrapolation) procedure could be applied to estimate the full first (especially important) quark moments. © 2005 Pleiades Publishing, Inc.

PACS numbers: 13.60.Hb, 13.85.Ni, 13.88.+e

The extraction of the quark helicity distributions is one of the main tasks of the semi-inclusive deep inelastic scattering (SIDIS) experiments (HERMES [1], COMPASS [2]) with a polarized beam and target. At the same time, it was argued in [3] that to obtain reliable distributions at the relatively low average Q^2 available to the modern SIDIS experiments,[1] the leading order (LO) analysis is not sufficient and the next to leading order (NLO) analysis is necessary. In [4], a procedure allowing the direct extraction from the SIDIS data of the first moments of the quark helicity distributions in NLO QCD was proposed. However, in spite of the special importance of the first moments, it is certainly very desirable to have a procedure of reconstruction in NLO QCD of the polarized densities themselves. However, it is extremely difficult to extract the local in x_B distributions directly, because of the double convolution product entering the NLO QCD expressions for semi-inclusive asymmetries (see [4] and references therein). On the other hand, operating just as in [4], one can directly extract not only the first moments but also the Mellin moments of any required order. The simple extension of the procedure proposed in [4] gives for the *n*th moments $\Delta_n q \equiv \int_0^1 dx\, x^{n-1} q(x)$ of the valence distribu-

tions the equations

$$
\Delta_n u_V = \frac{1}{5} \frac{\mathcal{A}_p^{(n)} + \mathcal{A}_d^{(n)}}{L_{(n)1} - L_{(n)2}}; \quad \Delta_n d_V = \frac{1}{5} \frac{4\mathcal{A}_d^{(n)} - \mathcal{A}_p^{(n)}}{L_{(n)1} - L_{(n)2}}, \quad (1)
$$

where all the quantities in the right-hand side are the same as in [4] (see Eqs. (18)–(23)) with the replacement of

$$
\int_0^1 dx \quad \text{by} \quad \int_0^1 dx\, x^{n-1}.
$$

It should be noticed that, in reality, one can measure the asymmetries only in the restricted x_B region $0 < a < x < b < 1$, so that the approximate equations for the truncated moments

$$
\Delta_n' q \equiv \int_a^b dx\, x^{n-1} \Delta q(x) \quad (2)
$$

of the valence distributions have the form (1) with the replacement of the full integrals by the sums over bins covering the accessible x_B region $a < x < b$, so that

$$
\mathcal{A}_p^{(n)} \simeq \sum_{i=1}^{N_{\text{bins}}} x^{n-1} \Delta x_i A_p^{\pi^+ - \pi^-}(x_i)\Big|_Z (4u_V - d_V)(x_i)
$$
$$
\times \int_Z^1 dz_h \Big[1 + \otimes \frac{\alpha_s}{2\pi} \tilde{C}_{qq} \otimes \Big](D_1 - D_2), \quad (3)
$$

---

and analogously for $\mathcal{A}_d^{(n)}$.

Thus, one can directly extract from the data the nth Mellin moments of valence distributions. The question arises: is it sufficient to reconstruct the local in x_B distributions?

There exist several methods allowing us to reconstruct the local in x_B quantities (such as structure functions, polarized and unpolarized quark distributions, etc.) knowing their nth Mellin moments. All of them use the expansion of the local quantity in a series over the orthogonal polynomials (Bernstein, Legendre, Jacobi, etc.). The most successful in applications (reconstruction of the local distributions from the evolved with GLAP moments and investigation of Λ_{QCD}) occurred the Jacobi polynomial expansion method (JEM) proposed in the pioneer work by Parisi and Sourlas [5] and elaborated[2] in [6, 7]. Within JEM, the local in x_B functions (structure functions or quark distributions) are expanded in the double series over the Jacobi polynomials and Mellin moments—see Eq. (A.1) in the Appendix. For what follows, it is of importance that the moments entering Eq. (A.1) are the full moments, i.e., the integrals over the entire x_B region $0 < x < 1$: $M[j] = \int_0^1 dx\, x^{j-1} F(x)$. Until now, nobody investigated the question of the applicability of JEM to the rather narrow x_B region available to the modern polarized SIDIS experiments. Consequently, let us try to apply JEM to the reconstruction of $\Delta u_V(x)$ and $\Delta d_V(x)$ in the narrow x_B region[3] $a = 0.023 < x < b = 0.6$ available to HERMES and to investigate if it is possible to safely replace the full moments by the truncated ones. To this end, we perform the simple test. We choose[4] GRSV2000NLO (symmetric sea) parameterization [9] at $Q^2 = 2.5$ GeV^2. Integrating the parameterization over the HERMES x_B region, we then calculate twelve truncated moments of the u and d valence distributions given by Eq. (2) with $a = 0.023$, $b = 0.6$. Substituting these moments in the expansion (A.1) with $N_{max} = 12$, we look for optimal values of the parameters α and β corresponding to the minimal deviation of the reconstructed curves for $\Delta u_V(x)$ and $\Delta d_V(x)$ from the input (reference) curves corresponding to the input parameterization. To find these optimal values α_{opt} and β_{opt}, we

---

[2] JEM with respect to polarized quark densities was first applied in [8].
[3] We choose here the most narrow HERMES x_B region where the difference between JEM and its modification MJEM (see below) application becomes especially impressive. However, even with the wider x_B region (for example, the COMPASS [2] region $0.003 < x < 0.7$), it is of importance to avoid the additional systematical errors caused by the replacement of the full (unaccessible) moments in JEM (A.1) by the accessible truncated moments.
[4] Certainly, one can choose for testing any other parameterization.

use the program MINUIT [10]. To control the quality of the reconstruction, we introduce the parameter

$$\nu = \frac{\int_a^b dx \left| F_{\text{reconstructed}}(x) - F_{\text{reference}}(x) \right|}{\left| \int_a^b dx\, F_{\text{reference}} \right|} \times 100\%, \quad (4)$$

where $F_{\text{reference}}(x)$ corresponds to the input parameterization and $F_{\text{reconstructed}}(x) \equiv F_{N_{max}}(x)$ in Eq. (A.1) from the Appendix. The comparison of the reconstructed and input (reference) curves shows that, even for a such a high number of moments used, $N_{max} = 12$, they strongly differ from each other: $\nu|_{JEM} = 6.24\%$ for Δu_V and $\nu|_{JEM} = 5.52\%$ for Δd_V. Thus, the substitution of truncated moments instead of exact ones in expansion (A.1) is a rather crude approximation (at least for the HERMES x_B region). Fortunately, it is possible to modify the standard JEM in a such way that the new series contains the truncated moments instead of the full ones. The new expansion looks as (see the Appendix)

$$F(x) \simeq F_{N_{max}}(x) = \left(\frac{x-a}{b-a}\right)^\beta \left(1 - \frac{x-a}{b-a}\right)^\alpha$$

$$\times \sum_{n=0}^{N_{max}} \Theta_n^{(\alpha, \beta)}\left(\frac{x-a}{b-a}\right) \sum_{k=0}^{n} c_{nk}^{(\alpha, \beta)} \frac{1}{(b-a)^{k+1}} \quad (5)$$

$$\times \sum_{l=0}^{k} \frac{k!}{l!(k-l)!} M'[l+1](-a)^{k-l},$$

where we introduce the notation (c.f., Eq. (2))

$$M'[j] \equiv M'_{[a, b]}[j] \equiv \int_a^b dx\, x^{j-1} F(x) \quad (6)$$

for the moments truncated to the x_B region accessible for measurement. It is of great importance that, now, in the expansion, not the full (unavailable) but the truncated (accessible) moments enter. Thus, having at our disposal the first few truncated moments extracted in NLO QCD (see Eqs. (1)) and using MJEM (Eq. (5)), one can reconstruct the local distributions in the x_B region accessible for measurement.

Let us check how well MJEM works. To this end, let us repeat the simple exercises with reconstruction of the known GRSV2000NLO (symmetric sea) parameterization and compare the results of the $\Delta u_V(x)$ and $\Delta d_V(x)$ reconstruction with the usual JEM and with the proposed MJEM. To control the quality of the reconstruc-

tion, we again use[5] the parameter ν given by Eq. (4), where now $F_{\mathrm{reconstructed}}(x) \equiv F_{N_{\max}}(x)$ in Eq. (5). We performed the reconstruction with both a very high number of moments $N_{\max} = 12$ and a small number of moments $N_{\max} = 4$. Notice that the last choice ($N_{\max} = 4$) is especially important because of the peculiarities of the data on the asymmetries provided by the SIDIS experiments. Indeed, the number of moments used should be as small as possible because, first, the relative error $|\delta(M'[j])/M'[j]|$ on $M'[j]$ becomes higher with an increase of j and, second, the high moments become very sensitive to the replacement of integration by the sum over the bins. The results of the $\Delta u_V(x)$ and $\Delta d_V(x)$ reconstruction with MJEM for $N_{\max} = 12$ demonstrate that, in contrast to the usual JEM, MJEM gives excellent agreement between the reference and reconstructed curves: $\nu|_{\mathrm{MJEM}} = 0.06\%$ for $\Delta u_V(x)$ and $\nu|_{\mathrm{MJEM}} = 0.08\%$ for $\Delta d_V(x)$.

In the case of $N_{\max} = 4$, the difference in the quality of the reconstruction between JEM and MJEM (see Fig. 1) becomes especially impressive.[6] While for standard JEM the reconstructed and reference curves strongly differ from each other, the respective curves for MJEM are in good agreement. Thus, one can conclude that dealing with the truncated (available for measurement) x_B region, one should apply, instead of the usual JEM, the proposed modified JEM to obtain reliable results on the local distributions.

Until now, we looked for the optimal values of the parameters α and β entering MJEM using the explicit form of the reference curve (input parameterization). Certainly, in reality, we do not have any reference curve to be used for the optimization. However, one can extract the first few moments from the data in NLO QCD (see Eqs. (1)). Thus, we need some criterion of MJEM optimization that could be used for optimization of α and β, only the known (extracted) moments entering MJEM.

At first sight, it seems to be natural to find the optimal values of α and β minimizing the difference reconstructed with MJEM (5) and the input moments[7] entering
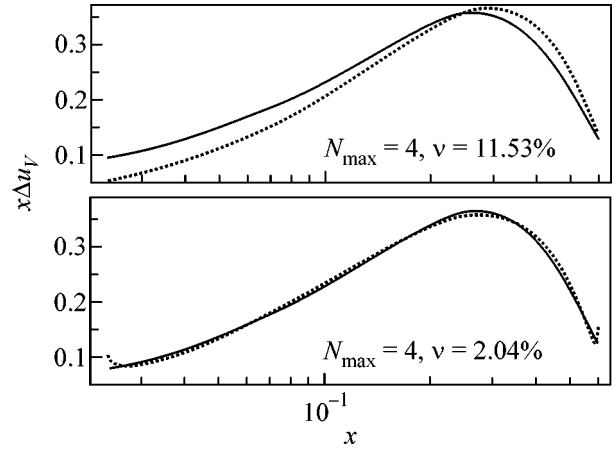

Fig. 1. Comparison of the quality of the $\Delta u_V(x)$ reconstruction with the usual JEM (top) and with MJEM (bottom). The solid lines correspond to the input (reference) parameterization. The dotted lines correspond to the distributions reconstructed with JEM (top) and with MJEM (bottom).

the MJEM expansion (5) moments. However, it is easy to prove[8] that this difference is identically equal to zero:

$$M'_{[a, b]}[n]\big|_{\mathrm{reconstructed}} \equiv M'_{[a, b]}[n]\big|_{\mathrm{input}}, \quad n \leq N_{\max}, \quad (7)$$

i.e., all the reconstructed moments with $n \leq N_{\max}$ are identically equal to the respective input moments for any α and β. Fortunately, we can use for comparison the reference twice-truncated moments

$$M''[n] \equiv M''_{[a + a', b - b']}[n] \equiv \int_{a + a'}^{b - b'} dx\, x^{n - 1} F(x) \quad (8)$$
$$(a < a + a' < b - b' < b),$$

i.e., the integrals over the region less than the integration region $[a, b]$ for the "once-truncated" moments $M'_{[a, b]}$ entering MJEM (5). The respective optimization criterion can be written in the form

$$\sum_{j = 0}^{N_{\max}} \left| M''_{(\mathrm{reconstructed})}[j] - M''_{(\mathrm{reference})}[j] \right| = \min. \quad (9)$$

The twice truncated reference moments should be extracted in NLO QCD from the data in the same way as the input (entering MJEM (5)) once truncated moments. In reality, one can reconstruct from the data twice-truncated moments using Eq. (1) and remove, for example, the first and/or last bin from the sum in Eq. (3).

Let us now check how well the optimization criterion (9) works. To this end, we again perform a simple numerical test. We choose GRSV2000NLO parameter-

---

[5] Calculating ν, we just cut off the boundary distortions that hold for MJEM in the small vicinities of the boundary points (see the Appendix) and decrease the integration region, respectively. To be more precise, one can apply, after the cutting, some extrapolation to the boundary points. However, practice shows that the results on calculation of ν are practically insensitive to the method of extrapolation, since the widths of the boundary distortion regions are very small (less than 10^{-3}).

[6] For Δd_V, we obtained an even more impressive difference between the JEM and MJEM application with $N_{\max} = 4$: $\nu|_{\mathrm{JEM}} = 13.33\%$, while $\nu|_{\mathrm{MJEM}} = 1.2\%$.

[7] In practice, one should reconstruct these input moments from the data using Eqs. (1). The reference "twice-truncated" moments (8) should be reconstructed from the data in the same way.

[8] It can be proved by analogy with the case of the usual JEM, where Eq. (7) with $[a, b] = [0, 1]$ holds (see, for example, [7]).

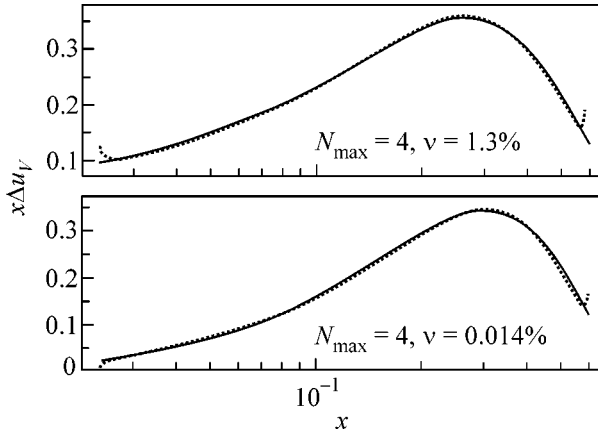**Fig. 2.** The results of Δu_V reconstruction for GRSV2000**NLO** parametrization for both symmetric (top) and broken sea (bottom) scenarios. The solid line corresponds to the reference curve (input parameterization). The dotted line is reconstructed with MJEM and criterion (9) inside the region accessible for measurement ([0.023, 0.6] here). The optimal values of α and β are $\alpha_{opt} = -0.15555$, $\beta_{opt} = -0.097951$ and $\alpha_{opt} = -0.209346$, $\beta_{opt} = 0.153417$ for the symmetric and broken sea scenarios, respectively.

Fig. 3. The results of Δu_V reconstruction in the region $[a_{min} = 10^{-4}, b_{max} = 1]$ for GRSV2000**NLO** parameterization for both symmetric (up) and broken sea (down) scenarios. The solid line corresponds to the reference curve (input parameterization). The dotted line corresponds to the curve reconstructed in the entire $[a_{min} = 10^{-4}, b_{max} = 1]$ region with the requirement of minimal deviation from the curve (bold solid line) reconstructed with MJEM and criterion (9) inside the region accessible for measurement ([0.023, 0.6] here).

ization at $Q^2 = 2.5$ GeV^2 with both broken and symmetric sea scenarios. We then calculate the first four once-truncated and the first four twice-truncated moments defined by Eqs. (6) and (8) and substitute them in the optimization criterion (9). To find the optimal values of α and β, we use the MINUIT [10] program. The results are presented[9] in Fig. 2. It is seen that the optimization criterion works well for both the symmetric and broken sea scenarios. The deviations of the reconstructed curves from the reference curves (input parameterization) near the boundary points are unavoidable, since MJEM is correctly defined in the entire region (a, b), except for in small vicinities of the boundary points (see the Appendix). Fortunately, these distortions occur in very small vicinities of the boundary points, and the curves are in very good agreement in practically the entire accessible x_B region. Notice that, for the procedure of extrapolation outside the accessible x_B region, one should just cut off these unphysical boundary distortions (see below).

Thus, one can conclude that MJEM can be successfully applied for reconstruction of the local distributions knowing only the first few truncated Mellin moments. Notice, however, that, by construction, MJEM reproduces the local distributions only in the x_B region accessible for measurement. The question arises: could one attempt to reconstruct the local distributions outside the accessible region (i.e., to perform

extrapolation) using the distributions obtained with MJEM as an input? To this end, we propose to solve the following variational task. We apply MJEM, Eq. (5), to the maximally[10] extended x_B region $[a_{min}, b_{max}]$ replacing the moments $M'_{[a_{min}, b_{max}]}[j]$ by $M'_{[a, b]}[j] + \epsilon_j$, where $\epsilon_j (j = 1...4)$ are the free variational parameters (ϵ_j should be considered as unknown "tails" of the full moments). Then, using the MINUIT program [10], one finds the parameters ϵ_j requiring the minimal deviation of the curve reconstructed with ϵ_j from the input (reconstructed with criterion (9)) curve inside the region $[a, b]$ accessible for measurement. The quantities $M'_{[a, b]}[j] + \epsilon_j$ reconstructed in this way should be compared with the reference (obtained by direct integration of the input parameterization) moments $M'_{[a_{min}, b_{max}]}[j]|_{reference}$. In the ideal case (the ideal reconstruction of tails ϵ_j), these quantities would coincide.

Let us test this variational (extrapolation) procedure by a simple numerical exercise. We choose GRSV2000NLO parameterization (for both broken and symmetric sea scenarios) at $Q^2 = 2.5$ GeV^2 as the reference one. Since the allowed [9] x_B region for this parameterization is $[10^{-4}, 1]$, we choose $[a_{min}, b_{max}] = [10^{-4}, 1]$, and, for the truncated region $[a, b]$, we again choose the x_B region $[a, b] = [0.023, 0.6]$ accessible for

---

[9] For Δd_V, we also get very good agreement between the input and reconstructed curves: $\nu = 0.3\%$ and $\nu = 0.07\%$ for the symmetric and broken sea scenarios, respectively.
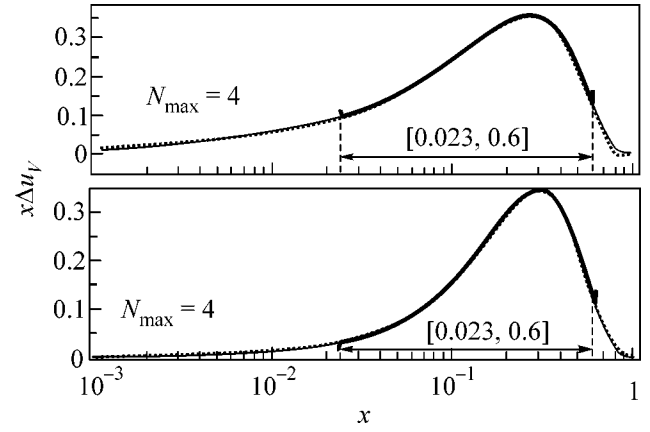
[10] For a moment, we restrict ourselves to the x_B region $[a_{min} = 10^{-4}, b_{max} = 1]$, which is typical for the most known parameterizations on the quark helicity distributions.

HERMES. Notice that, by performing the variational (extrapolation) procedure, we cut off the boundary distortions of the curve (which enters the variational procedure as an input) obtained with MJEM and criterion (9) inside the accessible x_B region.

The results of the variational (extrapolation) procedure application are presented in Fig. 3 and the table. Comparing the reconstructed curve with the input parameterization for $\Delta u_V(x)$ (see Fig. 3), one can see that they are in good agreement. The first four reconstructed moments are also in good agreement with the respective reference (obtained by direct integration of the input parameterization) moments—see the table. For Δd_V, the quality of the reconstruction is also very good for the symmetric sea scenario and a little bit worse[11] in the case of the broken sea scenario. In any case, the reconstructed first moments (the most important for understanding the proton spin structure) are in good agreement with the respective reference moments of both the Δu_V and Δd_V distributions.

Thus, all the numerical tests confirm that the proposed modification of the Jacobi polynomial expansion method, MJEM, allows us to reconstruct with high precision the quark helicity distributions in the x_B region that is accessible for measurement. We consider this to be the main result of this paper. In addition, the numerical calculations encourage one that the proposed variational (extrapolation) procedure based on MJEM could become a reliable extrapolation procedure. Certainly, careful additional investigations are necessary.

First of all, we plan to apply the proposed method to HERMES data on pion production with both proton and deutron targets. As it was shown above, MJEM (rather than the usual JEM) should be applied for reconstruction of the local (in x_B) distributions from NLO QCD extracted moments in all modern semi-inclusive DIS experiments (such as the COMPASS experiment) with the restricted accessible x_B region. Especially, MJEM application becomes absolutely necessary for the rather narrow HERMES x_B region. To extract the valence quark helicity distributions in NLO QCD with the proposed method, we will use the so-called "difference asymmetries" (for the essential advantages of these asymmetries see [4] and references therein), which now are constructed by HERMES. At present, the extended paper with simulations corresponding to HERMES kinematics is in preparation.

Results of the first four moments of Δu_V reconstruction in the region $[a_{\min} = 10^{-4}, b_{\max} = 1]$ for the GRSV2000NLO parameterization for both symmetric (top) and broken sea (bottom) scenarios

n	$M'^{\text{input}}_{[0.023, 0.6]}$	$M'^{\text{output}}_{[10^{-4}, 1]}$	$M'^{\text{reference}}_{[10^{-4}, 1]}$
1	0.749	0.904	0.917
2	0.153	0.164	0.167
3	0.047	0.053	0.055
4	0.017	0.021	0.023
1	0.570	0.609	0.605
2	0.137	0.150	0.149
3	0.044	0.052	0.052
4	0.017	0.023	0.022

APPENDIX

The JEM is the expansion of the x-dependent function (structure function or quark density) in the series over Jacobi polynomials $\Theta_n^{(\alpha, \beta)}(x)$ orthogonal with weight $\omega^{(\alpha, \beta)}(x) = x^\beta (1 - x)^\alpha$ (see [5–7] for details):

$$
F(x) \simeq F_{N_{\max}}(x) = \omega^{(\alpha, \beta)} \sum_{k=0}^{N_{\max}} \Theta_k^{(\alpha, \beta)}(x) \\
\times \sum_{j=0}^{k} c_{kj}^{(\alpha, \beta)} M(j+1),
$$
(A.1)

where $M[j] = \int_0^1 dx\, x^{j-1} F(x)$ and

$$
\int_0^1 dx\, \omega^{(\alpha, \beta)}(x) \Theta_n^{(\alpha, \beta)}(x) \Theta_m^{(\alpha, \beta)}(x) = \delta_{nm}.
$$
(A.2)

The details on the Jacobi polynomials

$$
\Theta_k^{(\alpha, \beta)}(x) = \sum_{j=0}^{k} c_{kj}^{(\alpha, \beta)} x^j
$$
(A.3)

can be found in [5] and [6]. Expansion (A.1) becomes exact when $N_{\max} \longrightarrow \infty$. However, in practice, one truncates series (A.1) retaining only finite number of moments $N_{\max}$ in the expansion. The experience shows [7] that JEM produces good results (for the entire x_B region) even with the small number $N_{\max}$.

The idea of the modified expansion is to reexpand $F(x)$ in the series over the truncated moments $M'_{[a, b]}[j]$

---

[11]The point is that, in the case of the broken sea scenario, the moments of Δd_V are very small quantities and, in addition, $\Delta d_V(x)$ changes its sign at small x_B [9]. Thus, the application of the proposed variational (extrapolation) procedure, in this case, becomes more complicated.

given by Eq. (6), performing the rescaling $x \longrightarrow a + (b - a)x$, which compress the entire region [0, 1] to the truncated region [a, b]. To this end, let us apply the following ansatz[12]

$$F(x) = \left(\frac{x-a}{b-a}\right)^{\beta}\left(1 - \frac{x-a}{b-a}\right)^{\alpha}$$
$$\times \sum_{n=0}^{\infty} \tilde{f}_n \Theta_n^{(\alpha,\beta)}\left(\frac{x-a}{b-a}\right) \tag{A.4}$$

and try to find the coefficients $\tilde{f}_n$. Multiplying both parts of Eq. (A.4) by $\Theta_k^{(\alpha,\beta)}((x-a)/(b-a))$, integrating over x in the limits [a, b] and performing the replacement $t = (x-a)/(b-a)$, one gets

$$\int_a^b dx F(x) \Theta_k^{(\alpha,\beta)}\left(\frac{x-a}{b-a}\right)$$
$$= (b-a) \sum_{n=0}^{\infty} \tilde{f}_n \int_0^1 dt\, t^{\beta}(1-t)^{\alpha} \Theta_n^{(\alpha,\beta)}(t)\Theta_k^{(\alpha,\beta)}(t),$$

so that with the orthogonality condition Eq. (A.2) one obtains

---

[12] Notice that ansatz (A.4) (as well as expansion Eq. (5) itself) is correctly defined inside the entire region (a, b) except for in the small vicinities of the boundary points (absolutely the same situation holds for the usual JEM, Eq. (A.1), applied to the quark distributions in the region (0, 1)). In practice, the respective boundary distortions are just cut off when one performs the extrapolation procedure.

$$\tilde{f}_n = (b-a)^{-1} \int_a^b dx F(x) \Theta_n^{(\alpha,\beta)}\left(\frac{x-a}{b-a}\right). \tag{A.5}$$

Substituting Eq. (A.5) in the expansion (A.4) and using Eq. (A.3), one eventually arrives at Eq. (5) (with $N_{\text{max}} \longrightarrow \infty$) of the main text.

REFERENCES

1. A. Airapetyan *et al.* (HERMES Collab.), Phys. Rev. D **71**, 012003 (2005).

2. G. Baum *et al.* (COMPASS Collab.), *COMPASS: A Proposal for a Common Muon and Proton Apparatus for Structure and Spectroscopy* (1996), CERN-SPSLC-96-14.

3. A. N. Sissakian, O. Yu. Shevchenko, and O. N. Ivanov, Phys. Rev. D **68**, 031502 (2003).

4. A. N. Sissakian, O. Yu. Shevchenko, and O. N. Ivanov, Phys. Rev. D **70**, 074032 (2004).

5. G. Parisi and N. Sourlas, Nucl. Phys. B **151**, 421 (1979).

6. I. S. Barker, C. S. Langensiepen, and G. Shaw, Nucl. Phys. B **186**, 61 (1981); CERN-TH-2988.

7. V. G. Krivokhizhin *et al.*, Z. Phys. C **36**, 51 (1987); JINR-E2-86-564.

8. E. Leader, A. V. Sidorov, and D. B. Stamenov, Int. J. Mod. Phys. A **13**, 5573 (1998).

9. M. Gluck, E. Reya, M. Stratmann, and W. Vogelsang, Phys. Rev. D **63**, 094005 (2001); hep-ph/0011215.

10. F. James and M. Roos, Comput. Phys. Commun. **10**, 343 (1975).

Principle of Forming Bound States of Atoms in a Laser Field

O. N. Gadomsky* and A. G. Glukhov

Ul'yanovsk State University, ul. L'va Tolstogo 42, Ul'yanovsk, 432700 Russia
*e-mail: qed_group@mail.ru
Received May 24, 2005

It has been shown that different regimes of forming bound states of colliding atoms are possible due to their near-field interaction in a laser field. Analysis is performed for room temperature and a weak laser field under the conditions of smooth scanning of the laser radiation frequency in dependence on frequencies of near-field optical resonances. © 2005 Pleiades Publishing, Inc.

PACS numbers: 34.50.Rk, 42.50.Vk

The action of laser radiation on atoms, molecules, or dielectric microparticles provides control over their motion due to the effect of radiation forces on them [1, 2]. To date, radiation forces that are directly caused by laser radiation are analyzed for the case where interparticle distances are much larger than the radiation wavelength, i.e., in the wave zone of radiation. The situation is fundamentally different when particles are spaced by distances comparative to or less than the radiation wavelength. In this case, an additional field caused by the action of atoms on each other in the external-radiation field in the near zone is comparative to the external radiation field. As was shown in [3], the additional field is responsible for significant change in the amplitude, phase, and frequency characteristics of the dipole radiation of interacting atoms. This property of the action of closely approaching atoms on each other was interpreted in [3] as a near-field effect. This effect can be manifested in the optical properties of nanostructure systems (dimers, atomic chains, fullerenes), in Brewster reflection of light from the surface of nonabsorbing dielectrics, and in optical sounding of the surfaces of solids [3].

In addition to the above effects, the action of particles on each other leads to the appearance of a force between the particles. From the physical point of view, the force between two atomic particles arises due to interaction between induced dipole moments. From the quantum-mechanical point of view, the induced dipole moments of atoms arise due to the induction of atomic coherence by the laser field. For dielectric particles, the force is caused by the macroscopic polarization of these particles.

This force can be important in various areas. The force of interaction between atoms and molecules in the laser radiation field is important in laser cooling of atoms in traps, including magneto-optical traps; experiments on Bose–Einstein condensation; atomic force microscopy; etc. The force of interaction between dipole particles and the radiation field is important in control over the motion of microparticles, including control over the spatial location of viruses and bacteria.

In this work, we analyze the dipole-interaction forces between atoms that are caused by continuous quasiresonant laser radiation. The results show that the interaction forces depend strongly on the interatomic distance, polarization, and frequency of the laser field, as well as on the Doppler shift of the frequencies.

The dipole–dipole interaction between atoms in dense ensembles irradiated by the laser field was taken into account in many works [5–9]. In contrast to those works, in this work, we show that optical dimensional resonances play an important role in control over the laser-radiation-induced motion of atoms in dense atomic ensembles. Optical dimensional resonances in a system of immovable atoms were considered in [10–12]. The existence of such resonances was experimentally corroborated in [13], where characteristic maxima were observed in the spectra of anisotropic reflection of light from the arsenic-stabilized gallium-arsenide surface. In our opinion [14], these maxima indicate that optical dimensional resonances exist in arsenic dimers. The appearance of optical dimensional resonances may be expected in various systems consisting of a small number of atoms forming nanostructure systems. In this work, optical dimensional resonances are considered in systems of moving interacting atoms with the inclusion of the Doppler frequency shift. Moreover, in contrast to works [5–9], the motion of atoms in laser fields is considered without a significant change in the population of atomic states and disregarding spontaneous transitions of atoms from excited states to the ground state. As is shown in this work, the effective control over the motion of atoms in dense ensembles can be ensured in weak laser fields due to the tuning of the laser radiation frequency to the dimensional resonance frequency depending on the interatomic distance.

We consider two-level atoms: one of which is at the origin of the coordinates $\mathbf{r}_1 = 0$ and the other, at the point $\mathbf{r}_2 = (0, R, 0)$. The atoms are irradiated by a traveling laser wave with constant amplitude $\mathbf{E}_{0L}$ and frequency ω, which is close to the atomic-transition frequencies ω_{01} and ω_{02}. The electric field strength of this wave has the form

$$\mathbf{E}_L(\mathbf{r}, t) = \mathbf{E}_{0L}\exp(i\mathbf{k}_0\mathbf{r} - i\omega t), \qquad (1)$$

where $\mathbf{k}_0$ is the wavevector of the external wave.

The electric field formed by the laser wave and dipole moments of the atoms at the observation point $\mathbf{r}$ and time t is represented as

$$\mathbf{E}(\mathbf{r}, t) = \mathbf{E}_L(\mathbf{r}, t) + \sum_{j=1}^{2}\operatorname{curl}\operatorname{curl}\frac{\langle\mathbf{d}\rangle_j(t - R_j/c)}{R_j}. \quad (2)$$

Here, the induced dipole moment $\langle\mathbf{d}\rangle_j$ of the jth atom depends on the field at the point where this atom is located, $R_j = |\mathbf{r} - \mathbf{r}_j|$, and c is the speed of light in vacuum. The observation point $\mathbf{r}$ in Eq. (2) may coincide with one of the points $\mathbf{r}_1$ and $\mathbf{r}_2$ or be beyond these points. Differentiation in Eq. (2) is performed with respect to the coordinates of the observation point. We emphasize that the induced dipole moments $\langle\mathbf{d}\rangle_1$ and $\langle\mathbf{d}\rangle_2$ in the near zone are determined only by the electric vector of the electromagnetic field. The effect of the magnetic vector of the field becomes comparable with the effect of the electric vector only in the wave zone, where $k_0R_j \gg 1$.

The Hamiltonian of the system of two atoms has the form

$$
\begin{aligned}
\mathbf{H} = \frac{1}{2}\hbar\sum_{j=1}^{2}\omega_{0j}(\mathbf{I} + \sigma_{3j}) \\
- \frac{1}{2}\sum_{j=1}^{2}(\mathbf{d}_{0j}^*\sigma_{+j}\mathbf{E}_j + \mathbf{d}_{0j}\sigma_{-j}\mathbf{E}_j),
\end{aligned}
\qquad (3)
$$

where $\mathbf{E}_j$ is the electric field strength at the point where the jth atom is located, $\mathbf{d}_{0j}$ is the matrix element of the dipole moment of the jth atom, $\mathbf{I}$ is the identity operator, and $\sigma_{\alpha j}$ ($\alpha = 1, 2, 3, j = 1, 2$) and $\sigma_{\pm j} = (\sigma_{1j} \pm \sigma_{2j})$ are the effective spin operators of the jth atom that satisfy the known commutation relations. In the above notation, the dipole moment operators of the atoms have the form

$$\mathbf{d}_j = \frac{1}{2}(\mathbf{d}_{0j}^*\sigma_{+j} + \mathbf{d}_{0j}\sigma_{-j}). \qquad (4)$$

Using Hamiltonian (3), one may derive the Heisenberg equations of motion for two parts of the dipole moment operators $\mathbf{d}_{+j} = \mathbf{d}_{0j}^*\sigma_{+j}$ and $\mathbf{d}_{-j} = \mathbf{d}_{0j}\sigma_{-j}$, as well as for σ_{3j}. In the resulting equations, the transition to the mean values $s_{\alpha j} = \langle\sigma\rangle_{\alpha j}$ and $\mathbf{s}_{\pm j} = \langle\mathbf{d}\rangle_{\pm j}$ can be made. The form of the equations for the classical field does not change after the transition to mean values.

For further analysis, it is convenient to separate the field oscillations with an optical frequency by setting

$$\mathbf{E}_j = \mathbf{E}_{0j}\exp(-i\omega t), \quad \mathbf{E}_{0j} = \mathbf{E}_{0j}' - i\mathbf{E}_{0j}'', \qquad (5)$$

where $\mathbf{E}_{0j}'$ and $\mathbf{E}_{0j}''$ are, respectively, the real and imaginary parts of the field at the point where the jth atom is located. These quantities are time independent in stationary fields. We define the transformation

$$s_{1j} = u_j\cos\omega t - v_j\sin\omega t, \quad s_{2j} = u_j\sin\omega t - v_j\cos\omega t,$$

$$s_{3j} = w_j, \qquad (6)$$

$$s_{\pm j} = (u_j \pm iv_j)e^{\pm i\omega t}, \quad \mathbf{s}_{\pm j} = \mathbf{d}_{0j}(u_j \pm iv_j)e^{\pm i\omega t},$$

and the functions $\mathbf{X}_j = \mathbf{d}_{0j}(u_j - iv_j)$ and $\mathbf{X}_j^* = \mathbf{d}_{0j}^*(u_j + iv_j)$ determining the induced dipole moments of the atoms. The latter functions satisfy the equations for coupled quantum dipoles, which should be complemented by relaxation terms presenting the natural widths of the atomic transitions. Taking $W_j = 2\gamma_j$ for the total rate of the spontaneous decays of the upper levels, we arrive at the equations of motion for atomic variables in the final form

$$\dot{\mathbf{X}}_j = i\delta_j\mathbf{X}_j - \frac{2i}{\hbar}|\mathbf{d}_{0j}|^2 w_j\mathbf{E}_{0j} - \gamma_j\mathbf{X}_j, \qquad (7\text{a})$$

$$\dot{w}_j = \frac{i}{\hbar}(\mathbf{X}_j^*\mathbf{E}_{0j} - \mathbf{X}_j\mathbf{E}_{0j}^*) - 2\gamma_j(w_j - w_{0j}), \qquad (7\text{b})$$

where $\delta_j = \omega - \omega_{0j}$ is the detuning between the field frequency and the optical atomic-transition frequencies in the jth atom and ω_{0j} is the equilibrium value of ω_j. When deriving Eqs. (7), we take into account that $\mathbf{d}_{0j}(\mathbf{d}_{0j}\mathbf{E}_0) = |\mathbf{d}_{0j}|^2\mathbf{E}_0$ when $\mathbf{d}_{0j} \parallel \mathbf{E}_{0j}$.

Using Eqs. (1), (2), and (6), we represent $\mathbf{E}_{0j}$ in the form

$$\mathbf{E}_{01} = \mathbf{E}_{0L}\exp(i\mathbf{k}_0\mathbf{r}_1) + \frac{1}{2}\hat{G}\mathbf{X}_2\exp(ik_0R),$$

$$\mathbf{E}_{02} = \mathbf{E}_{0L}\exp(i\mathbf{k}_0\mathbf{r}_2) + \frac{1}{2}\hat{G}\mathbf{X}_1\exp(ik_0R),$$

$$(8)$$

where

$$\hat{G} = \begin{pmatrix} -A & 0 & 0 \\ 0 & 2B & 0 \\ 0 & 0 & -A \end{pmatrix}, \quad B = \frac{1}{R^3} - i\frac{k_0}{R^2},$$

$$A = B - \frac{k_0^2}{R}, \quad k_0 = \omega/c.$$

Equations (7) and (8) form a system of coupled equations that enables one to calculate the fields at the points where the atoms are located, as well as the induced dipole moments of the atoms, with the inclusion of the action of the atoms on each other. In what follows, we

use the coordinate system whose origin is at the center of mass of two atoms:

$$\mathbf{r}_1 = \frac{m_2}{m_1 + m_2}\mathbf{r}, \quad \mathbf{r}_2 = -\frac{m_1}{m_1 + m_2}\mathbf{r},$$

$$\mathbf{v}_1 = -\mathbf{v}_2, \quad \mathbf{v}_1 = \frac{m_2}{m_1 + m_2}\mathbf{v}, \qquad (9)$$

where $\mathbf{r} = \mathbf{r}_1 - \mathbf{r}_2$; m_1 and m_2 are the masses of atoms 1 and 2, respectively; and $\mathbf{v} = \dot{\mathbf{r}}$ is the velocity of the relative motion of the atoms.

Let us consider the most interesting case of interaction of the atoms with the stationary-radiation field at times much larger than the spontaneous relaxation time $\tau_{sp} = 1/2\gamma$. For such times, it should be taken into account in Eqs. (7) that

$$\dot{\mathbf{X}}_j = 0, \quad \dot{w}_j = 0, \quad \dot{\mathbf{v}} = 0. \qquad (10)$$

This means that the relaxation processes and processes of inducing dipole moments in the atoms compensate for each other. The condition $\dot{\mathbf{v}} = 0$ means that the center of mass of the atoms moves uniformly. The satisfaction of the condition $\dot{\mathbf{v}} = 0$ in the system of the atoms under thermal equilibrium conditions at a certain temperature T is determined by the number of collisions of an atom with the other atoms of the ideal gas per unit of time $\nu = (N/V)16r_0^2\sqrt{\pi k_B T/m_A}$, where r_0 is the radius of the atom, k_B is the Boltzmann constant, m_A is the mass of the atom, and N/V is the concentration of the atoms. It is necessary that the time interval between two subsequent collisions ν^{-1} be larger than the time τ_{sp}. In this case, Eqs. (7) under conditions (10) are reduced to a system of nonlinear algebraic equations.

We introduce the quantum polarizabilities of the atoms near the isolated resonances ω_{0j} as

$$\alpha_j = -\frac{2|\mathbf{d}_{0j}|^2}{\hbar}\frac{1}{\delta_j + i\gamma_j}. \qquad (11)$$

The stationary solution of Eq. (7a) can be represented in the form

$$X_1^y = -E_{0L}^y w_1\alpha_1 \frac{e^{i\mathbf{k}_0\mathbf{r}_1} - w_2\alpha_2 B e^{i\mathbf{k}_0\mathbf{r}_2}e^{ik_0R}}{1 - w_1w_2B^2\alpha_1\alpha_2e^{2ik_0R}} = \alpha_{\text{eff}}^y(1)E_{0L}^y,$$

$$X_1^{x,z} = -E_{0L}^{x,z} w_1\alpha_1 \frac{e^{i\mathbf{k}_0\mathbf{r}_1} + \frac{1}{2}w_2\alpha_2 A e^{i\mathbf{k}_0\mathbf{r}_2}e^{ik_0R}}{1 - \frac{1}{4}w_1w_2A^2\alpha_1\alpha_2e^{2ik_0R}}$$

$$= \alpha_{\text{eff}}^{x,z}(1)E_{0L}^{x,z}, \qquad (12)$$

$$X_2^y = -E_{0L}^y w_2\alpha_2 \frac{e^{i\mathbf{k}_0\mathbf{r}_2} - w_1\alpha_1 B e^{i\mathbf{k}_0\mathbf{r}_1}e^{ik_0R}}{1 - w_1w_2B^2\alpha_1\alpha_2e^{2ik_0R}} = \alpha_{\text{eff}}^y(2)E_{0L}^y,$$

$$X_2^{x,z} = -E_{0L}^{x,z} w_2\alpha_2 \frac{e^{i\mathbf{k}_0\mathbf{r}_2} + \frac{1}{2}w_1\alpha_1 A e^{i\mathbf{k}_0\mathbf{r}_1}e^{ik_0R}}{1 - \frac{1}{4}w_1w_2A^2\alpha_1\alpha_2e^{2ik_0R}}$$

$$= \alpha_{\text{eff}}^{x,z}(1)E_{0L}^{x,z},$$

where $\hat{\alpha}_{\text{eff}}(j)$ is the nonlinear effective polarizability of the jth atom.

The induced dipole moments of the atoms given by Eqs. (12) depend on w_1 and w_2, i.e., on the differences between the probabilities of observing atoms in the ground and excited states. The quantities w_1 and w_2 generally depend on the fields $\mathbf{E}_{01}$ and $\mathbf{E}_{02}$. Therefore, the effective polarizabilities are nonlinear functions of the external field $\mathbf{E}_{0L}$. However, analysis of the solution shows that there is a region of $\mathbf{E}_{0L}$ where the effective polarizabilities are nearly independent of the laser field $\mathbf{E}_{0L}$. This case corresponds to the linear approximation.

Moving atoms with identical ω_0 and $|\mathbf{d}_0|$ values cease to be identical. Indeed, the linear Doppler effect shifts the photon frequencies when passing from the rest coordinate system to the coordinate system of the atom moving with velocity $\mathbf{v}_j$. Therefore, $\alpha_1 \neq \alpha_2$ and

$$\alpha_1 = -\frac{2|\mathbf{d}_0|^2}{\hbar}\frac{1}{\omega - \mathbf{k}_0\mathbf{v}_1 - \omega_0 + i\gamma},$$

$$\alpha_2 = -\frac{2|\mathbf{d}_0|^2}{\hbar}\frac{1}{\omega + \mathbf{k}_0\mathbf{v}_1 - \omega_0 + i\gamma}. \qquad (13)$$

Substituting Eqs. (13) into Eqs. (12), we find dimensional resonance frequencies at which the effective polarizability of the atoms is maximal. At small distances, where $k_0R \ll 1$, we obtain the following formulas for the frequencies of optical dimensional resonances:

$$\omega_{1,2} = \omega_0 \pm \left[(\mathbf{k}_0\mathbf{v}_1)^2 + w_{10}w_{20}B^2\left(\frac{2|\mathbf{d}_0|^2}{\hbar}\right)^2\right]^{\frac{1}{2}},$$

$$\omega_{3,4} = \omega_0 \pm \left[(\mathbf{k}_0\mathbf{v}_1)^2 + \frac{1}{4}w_{10}w_{20}A^2\left(\frac{2|\mathbf{d}_0|^2}{\hbar}\right)^2\right]^{\frac{1}{2}}. \qquad (14)$$

Thus, in contrast to the case of immovable atoms [11], for moving identical atoms, four linear stationary optical dimensional resonances arise. The widths of these resonances are determined by the natural width of the levels of the isolated atoms belonging to the system. The atoms of the system are considered as isotropic. The action of the atoms on each other in the laser radiation field leads to the anisotropy of the diatomic system, because $\alpha_{\text{eff}}^y(j) \neq \alpha_{\text{eff}}^{x,z}(j)$.

The forces acting on the atoms of the diatomic system are determined by the formulas [2, 3]

$$\mathbf{F}_1 = -\left\langle \frac{\partial \mathbf{V}_1}{\partial \mathbf{r}_1} \right\rangle, \quad \mathbf{F}_2 = -\left\langle \frac{\partial \mathbf{V}_2}{\partial \mathbf{r}_2} \right\rangle, \tag{15}$$

where the angular brackets stand for quantum-mechanical averaging and $\mathbf{V}_1$ and $\mathbf{V}_2$ are the operators of the interaction between the respective atoms and the electric field. According to Eq. (3),

$$V_j = -\frac{1}{2}\sigma_{+j}\mathbf{d}_{0j}^*\mathbf{E}_{0j} - \frac{1}{2}\sigma_{-j}\mathbf{d}_{0j}\mathbf{E}_{0j}^* \tag{16}$$

for the two-level atoms of the system. Here, acting fields $\mathbf{E}_{0j}$ are determined by expressions (8), where $\mathbf{X}_j$ are determined in terms of effective polarizabilities (12) that are functions of the coordinates of the observation points $\mathbf{r}_1$ and $\mathbf{r}_2$. Substituting Eqs. (16) into Eqs. (15) and performing averaging, we arrive at the expressions

$$\mathbf{F}_1 = \frac{1}{2}\sum_{m=x,y,z} X_{1m}^* \frac{\partial E_{01}^m}{\partial \mathbf{r}_1} + \text{c.c.},$$
$$\mathbf{F}_2 = \frac{1}{2}\sum_{m=x,y,z} X_{2m}^* \frac{\partial E_{02}^m}{\partial \mathbf{r}_2} + \text{c.c.}, \tag{17}$$

where

$$X_{jm} = \alpha_{\text{eff}}^m(j)E_{0L}^m. \tag{18}$$

Calculating expressions (17), we can represent the forces $\mathbf{F}_1$ and $\mathbf{F}_2$ as the sum of three partial forces

$$\mathbf{F}_j = \mathbf{F}_j^{(1)} + \mathbf{F}_j^{(2)} + \mathbf{F}_j^{(3)}, \tag{19}$$

where $\mathbf{F}_j^{(1)}$ is directed along the wavevector $\mathbf{k}_0$ of the laser field and the forces $\mathbf{F}_j^{(2)}$ and $\mathbf{F}_j^{(3)}$ are directed along the unit vector $\mathbf{n} = (\mathbf{r}_1 - \mathbf{r}_2)/|\mathbf{r}_1 - \mathbf{r}_2|$ or opposite to it. The forces $\mathbf{F}_j^{(2)}$ and $\mathbf{F}_j^{(3)}$ are called the external- and internal-displacement forces of the atoms in the diatomic system in dependence on the sign of the vector $\mathbf{n}$ in the corresponding terms of Eq. (17).

In the absence of the dipole–dipole interaction, atoms do not affect each other. In this case, only the radiation pressure forces $\mathbf{F}_1^{(1)}$ and $\mathbf{F}_2^{(1)}$, which are determined by quantum polarizabilities (13), are nonzero in Eqs. (17) and (19). When the dipole–dipole interaction is taken into account, the forces $\mathbf{F}_1^{(1)}$ and $\mathbf{F}_2^{(1)}$ can also be called radiation pressure forces, although effective polarizabilities (12) should be used in the expressions for the induced dipole moments in this case.

The directions of the radiation pressure forces coincide with the wavevector $\mathbf{k}_0$ of the external radiation. The dispersion dependence of the radiation pressure forces is determined by the dispersion dependences of the effective polarizabilities of the atoms. This means that, for fixed interatomic distances R, the radiation pressure forces increase considerably when the external-field frequency coincides with the dimensional resonance frequency. The radiation pressure forces are proportional to the electric field strength squared of the external wave. Using the effective polarizabilities of potassium atoms, we calculate the dimensionless radiation pressure force $F_1^{(1)}/2\hbar k_0\gamma$ at the frequency of one of the dimensional resonances. It is seen that this force can be on the order of unity for laser fields $E_{0L} = 10^{-3}$ CGS unit that satisfy the linear-approximation condition $w_j \longrightarrow -1$.

Let us consider the behavior of two moving identical atoms interacting with each other in the laser field for various directions of the propagation of the laser wave with respect to the diatomic-system axis. The dimensionless forces acting on the first and second potassium atoms are approximately twice as strong as the radiation pressure force. This circumstance testifies to a considerable contribution to the dynamics of the atoms from other partial forces, namely, forces of internal and external displacements of the atoms. Moreover, the absolute values of the forces acting on the first and second atoms differ from each other, because moving atoms are not identical and their effective polarizabilities, as is seen in Eqs. (12), have different interatomic-distance dependences due to a difference in the quantum polarizabilities given by Eqs. (13). The acceleration of potassium atoms in the laser field is estimated as follows. In particular, for $F_{1y}/2\hbar k\gamma = 1$, where $k = \omega_0/c$, we obtain the force $F_{1y} = 1.33 \times 10^{-14}$ din and acceleration 0.32×10^9 cm/s². At a fixed velocity of the relative motion of the atoms, the resulting forces F_{1y} and F_{2y} acting on the atoms in the laser field depend strongly on the interatomic distances. In this case, the dependences of these forces on the laser field frequency also changes. This means that the effective control over the motion of the atoms is possible only with a corresponding change in the laser field frequency.

Let us analyze the trajectory of the 2D motion of interacting atoms in the field of a plane laser wave. The potential energy of the atoms in the diatomic system irradiated by the laser radiation field is given by the formulas

$$\langle \mathbf{V}_1 \rangle = -\frac{1}{2}\mathbf{X}_1^*\left(\mathbf{E}_{0L}e^{i\mathbf{k}_0\mathbf{r}_1} + \frac{1}{2}\hat{G}\mathbf{X}_2 e^{ik_0R}\right) + \text{c.c.},$$
$$\langle \mathbf{V}_2 \rangle = -\frac{1}{2}\mathbf{X}_2^*\left(\mathbf{E}_{0L}e^{i\mathbf{k}_0\mathbf{r}_2} + \frac{1}{2}\hat{G}\mathbf{X}_1 e^{ik_0R}\right) + \text{c.c.} \tag{20}$$

At large distances between atoms that are comparable with the laser radiation wavelength, the potential energy of an atom in the system can be both positive and negative in dependence on the detuning from the resonance. In other words, variation in the external-

radiation frequency provides the attraction or repulsion of atoms under the action of laser radiation.

Let us analyze the behavior of the potential energy of the atoms given by Eqs. (20) at small interatomic distances, where $k_0 R \ll 1$. In this case, the potential energies given by Eqs. (20) depend only on the interatomic distance. In the c.m.s. specified by Eqs. (9), the problem of the motion of two atoms at small distances reduces to the problem of the motion of one atom in a central field. As is known [15], the entire trajectory of a particle in the central field lies in one plane. The angular momentum $\mathbf{M}$ is perpendicular to this plane and is a conserving quantity; i.e., $M_x = M = \text{const}$. The complete solution of the problem of the motion of the particle in the central field can be obtained using the conservation laws for the energy E and angular momentum M without writing the equations of motion themselves. Then, following [15], we obtain the formulas

$$t = \int \frac{dr}{\sqrt{\frac{2}{m}[E - U(r)] - \frac{M^2}{m^2 r^2}}} + \text{const}, \qquad (21)$$

$$\varphi = \int \frac{\frac{M}{r^2} dr}{\sqrt{2m[E - U(r)] - \frac{M^2}{r^2}}} + \text{const}, \qquad (22)$$

where $m = m_A/2$ is the reduced mass of the atom, φ and r are the polar coordinates of the atom moving in the ZY plane, and $U(r) = \langle V_1 \rangle + \langle V_2 \rangle$. Formulas (21) and (22) provide the general solution of the problem of motion of interacting atoms. Formula (22) gives the relation between r and φ, i.e., the desired trajectory, whereas formula (21) implicitly determines the distance r of the moving particle from the center as a function of time. The condition

$$U(r) + M^2/2mr^2 = E, \qquad (23)$$

determines the extreme distances $r = R$ from the center for the possible motion region. When equality (23) is valid, the radial velocity $\dot{r}$ vanishes; however, this does not mean that the particle stops, because the angular velocity $\dot{\varphi} = M/mr^2$ does not vanish.

Let us analyze the finite motion of the particle in the region bounded by two circles with radii $r_{\max}$ and $r_{\min}$. In a time interval, when r varies from $r_{\max}$ to $r_{\min}$ and then to $r_{\max}$, the radius-vector of the particle rotates by the angle $\Delta\varphi$, which can be calculated by Eq. (22). The trajectory of the particle may be both closed and open in dependence on the form of the potential energy $U(r)$. Let us determine the potential energy U as a function of the coordinate r assuming that the laser field frequency varies according to formulas (14). Let the laser field polarization coincide with the y axis; i.e., $\mathbf{E}_{0L} \parallel \mathbf{y}_0$, where $\mathbf{y}_0$ is the unit vector of the y coordinate axis.
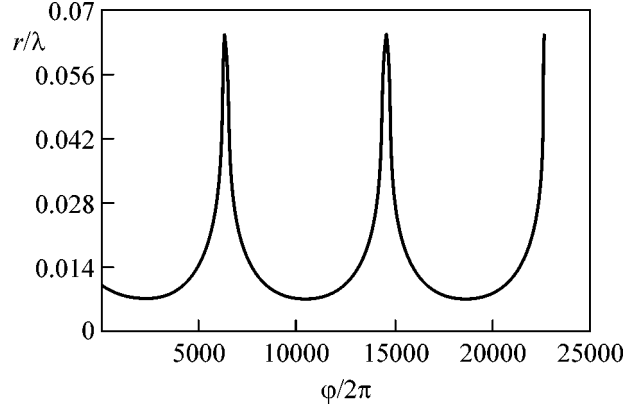

Fig. 1. Trajectory of the finite motion of atoms in the laser field when the potential energy depends on the distance according to law (24). The velocity of atoms entering the finite-motion region is $v = 60$ cm/s, $\mathbf{E}_{0L} \parallel \mathbf{y}_0$, and $E_{0L} = 0.05$ CGS unit. The frequency of the laser field satisfies the dimensional resonance condition $\omega = \omega_0 + B(2d_0^2/\hbar)$. The energy of the diatomic system in the finite-motion region is equal to $E = (m/2)\dot{r}^2 + (M^2/2mr^2) + U(r) = 0.68979 \times 10^{-19}$ erg.; the angular momentum is $M = m^2 v^2 \rho^2$, where $\rho = 0.01\lambda$ is the impact parameter at the initial time; $m = m_A/2$; and m_A is the mass of the potassium atom. The $3S$–$3P$ 5890-Å transition with a natural linewidth of 10 MHz [2] is considered in the potassium atom.

Then, at $\omega - \omega_0 = B(2d_0^2/\hbar)$, from Eq. (20), we obtain the following formula for the potential energy:

$$U(r) = \frac{1}{2} E_{0L}^2 r^3, \qquad (24)$$

where $r = R$ is the relative distance between the atoms. We point to the following properties of the resulting dependence (24). The potential energy of interaction between two moving atoms at $r \ll \lambda$ in the laser field, whose frequency varies in accordance with the interatomic distance, is independent of the velocity of the atoms and corresponds to the repulsion between the atoms. At small interatomic distances such that $r \ll \lambda$, we can consider that $\gamma \ll B(2d_0^2/\hbar)$. Therefore, the potential energy $U(r)$ varies with the distance as r^3. According to Eq. (14) for the other dimensional resonance at the chosen polarization of the laser field, we have $\omega - \omega_0 = -B(2d_0^2/\hbar)$ and the potential energy of the interatomic interaction is determined by the formula

$$U(r) = -2E_{0L}^2 \left(\frac{2d_0^2}{\hbar}\right) \frac{1}{\gamma^2} \frac{1}{r^3}, \qquad (25)$$

which corresponds to the attraction between the atoms.

Figure 1 shows the polar-angle dependence of the dimensionless distance r/λ for the potential energy of the interatomic interaction given by Eq. (24). The tra-
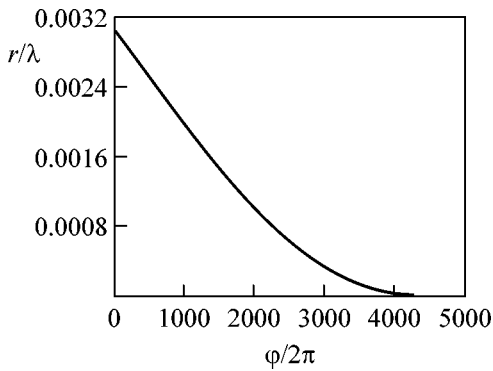
Fig. 2. Trajectory of the finite motion of atoms in the laser field when the attraction potential energy depends on the distance according to law (25) (fall of a particle to the center). The velocity of atoms entering the finite-motion region is $v = 5 \times 10^4$ cm/s, the impact parameter is $\rho = 0.0306\lambda$, $E_{0L} = 5 \times 10^{-3}$ CGS unit, and $E = 0.66 \times 10^{-15}$ erg. The frequency of the laser field satisfies the dimensional resonance condition $\omega = \omega_0 - B(2d_0^2/\hbar)$.

jectory $r(\varphi)$ of the relative motion is represented in the form of a 2D "rosette" consisting of the sequence of circular trajectories.

Another type of the finite motion corresponds to the potential energy given by Eq. (25). In this case, as follows from the inequality

$$\frac{m\dot{r}^2}{2} = E - U(r) - \frac{M^2}{2mr^2} > 0, \qquad (26)$$

very small interatomic distances are possible; i.e., $r \longrightarrow 0$, because $U(r)$ tends to $-\infty$ as $-1/r^n$, where $n = 3$. This case corresponds to the fall of the particle to the center. The minimum distance between the atoms is determined by the laser field frequency in accordance with the dimensional resonance condition $\omega = \omega_0 - B(2d_0^2/\hbar)$. Figure 2 shows the polar-angle dependence of the dimensionless distance for the potential energy given by Eq. (25).

Thus, we have proved that, by smoothly varying the laser radiation frequency according to Eqs. (14) at a fixed laser radiation polarization, one can efficiently control the finite motion of atoms at interatomic distances that are much smaller than the wavelength. Under such conditions in the field of continuous laser radiation, using the distance dependence of the potential energy given by Eq. (25), one can obtain dimers consisting of atoms of an ideal gas at room temperature, and the distance between atoms in dimers is determined by the corresponding laser radiation frequency.

We are grateful to V.G. Minogin for stimulating discussion of certain results of this work.

REFERENCES

1. V. I. Balykin, V. G. Minogin, and V. S. Letokhov, Rep. Prog. Phys. **63**, 1429 (2000).
2. V. G. Minogin and V. S. Letokhov, *Laser Light Pressure on Atoms* (Nauka, Moscow, 1986; Gordon and Breach, New York, 1986).
3. O. N. Gadomsky, Usp. Fiz. Nauk **170**, 1145 (2000) [Phys. Usp. **43**, 1071 (2000)].
4. H. T. Dung, L. Knol, and D.-G. Welsch, Phys. Rev. A **66**, 063810 (2002).
5. V. I. Yukalov, Eur. Phys. J. D **13**, 83 (2001).
6. R. H. Lemberg, Phys. Rev. A **2**, 883 (1970).
7. M. J. Stephen, J. Chem. Phys. **40**, 669 (1964).
8. O. N. Gadomsky, Teor. Mat. Fiz. **106**, 145 (1996).
9. O. N. Gadomsky and K. V. Krutitsky, J. Eur. Opt. Soc. **9**, 343 (1997).
10. O. N. Gadomsky and Yu. Yu. Voronov, Pis'ma Zh. Éksp. Teor. Fiz. **69**, 750 (1999) [JETP Lett. **69**, 804 (1999)].
11. O. N. Gadomsky and A. S. Kunitsin, Zh. Prikl. Spektrosk. **67**, 777 (2000).
12. V. V. Klimov and V. S. Letokhov, Phys. Rev. B **62**, 1639 (2000).
13. V. L. Berkovits, A. V. Gordeeva, and V. A. Kosobukin, Fiz. Tverd. Tela (St. Petersburg) **43**, 985 (2001) [Phys. Solid State **43**, 1018 (2001)].
14. O. N. Gadomsky and K. Yu. Moiseev, Opt. Spektrosk. **92**, 613 (2002) [Opt. Spectrosc. **92**, 560 (2002)].
15. L. D. Landau and E. M. Lifshitz, *Course of Theoretical Physics*, Vol. 1: *Mechanics* (Nauka, Moscow, 1965; Pergamon, New York, 1988).

Translated by R. Tyapaev

Structure of the Superfluid Ground State of an Atomic Fermi Gas Near the Feshbach Resonance

Yu. Kagan and L. A. Maksimov

Russian Research Centre Kurchatov Institute, Moscow, 123182 Russia
e-mail: kagan@kurm.polyn.kiae.su
Received June 6, 2005

The ground state of an atomic Fermi gas near the Feshbach resonance for a negative scattering length is investigated using the variational method. The structure of the superfluid state is formed by two coherently coupled subsystems, viz., the quasimolecular subsystem in a closed channel and the subsystem of atomic pairs in an open channel. The derived system of equations makes it possible to describe the properties of the ground state for arbitrary values of the parameters (in particular, to find the gap in the single-particle Fermi excitation spectrum and the speed of sound characterizing the branch of collective Bose excitations). © *2005 Pleiades Publishing, Inc.*

PACS numbers: 03.75.Kk, 67.60.–g, 74.20.Mn

A new field of research concerning ultracold gases of Fermi atoms and Bose molecules formed on their basis has been formed and developed in recent years. The key role in this research was played by the Feshbach resonance (FR) for the pair interaction of low-energy Fermi particles. The dependence of the position of the resonance on a constant magnetic field B provides a unique opportunity of continuous variation of the effective interaction between particles and its sign reversal (the change in the sign of the scattering length a) by means of varying the field [1].

The research in this field has passed through several stages over a short period of time. At the first stage, the formation of ultracold $^{40}K_2$ [2] and $^6Li_2$ [3–5] molecules in the vicinity of the FR was demonstrated for B values corresponding to a positive scattering length and, hence, to the existence of a true bound state near the dissociation threshold. In both cases, the resonance was in the S scattering channel. For electron-spin-polarized fermions, this presumes the interaction of nonidentical atoms in various hyperfine states.

It was found that molecules formed in such an excited state exist for a relatively long time. Owing to this property, as B varies, a quasi-adiabatic transition may occur from a state with $a < 0$, in which real molecules are not formed, to a state with $a > 0$ and back. The nature of the suppression of the inelastic processes upon collisions with a transition of molecules to deeper levels was consistently explained in [6].

The existence of molecules on the same vibrational level facilitates the conditions for the Bose–Einstein condensation in the formed gas of composite bosons. The condensation of excited molecules in explicit form was observed in a gas of ^{40}K atoms [7] and in a gas of ^6Li atoms [8–10].

In this connection, the study of an atomic Fermi gas near the FR for magnetic fields corresponding to scattering lengths $a < 0$ is of special interest.

Owing to the possibility of choosing the parameters such that a rarefied gas becomes a system of strongly interacting particles in the absence of real molecules, it is particularly interesting to analyze a many-particle superfluid state arising under these conditions. The use of the FR for achieving superfluidity in a gas of ultracold Fermi atoms was discussed in [11, 12]. The rearrangement of the superconducting state upon a transition from weak to strong attraction was considered earlier in [13, 14]. The interaction was of the single-channel type, and the spin configuration remained unchanged (see recent publication [15]). A salient feature of the FR is the two-channel type of the interaction. Particles interact in the continuous spectrum through the formation of an intermediate quasimolecular state in another spin configuration. An instantaneous photography reflects the two-component nature of the system with vapors of particles in the quasimolecular or free state. The two subsystems are involved in dynamic coherent exchange due to which the population of the quasimolecular state that decays in vacuum is constant at the amplitude level in equilibrium. The coherent superposition of quasimolecular states and pairs of atoms in the continuous spectrum ensures the formation of a superfluid state with a unified condensate.

The pattern of such a state was revealed experimentally first in the ^{40}K gas [16] and then in the ^6Li gas [17]. The idea of the experiment involved adiabatic projection of the state with $a < 0$ to a real molecular state with $a > 0$ due to quite fast variation of B, which prevents the formation of a condensate during the transition. Special measurements confirmed the latter assumption (see,

e.g., recent publication [18]). Experimental advances in this field stimulated a number of theoretical works [19–23] in which an attempt was made to describe microscopically a system of strongly interacting Fermi atoms based, however, on certain versions of perturbation theory.

This study is devoted to determining the ground state of the system of interacting Fermi atoms near the FR for $a < 0$ using the variational approach. As a result, it becomes possible to obtain a unified description of the ground state for an arbitrary ratio of the parameters.

The macroscopic variational function Ψ_0 is chosen taking into account that the ground state of the system near the FR is a unified state, which is mainly formed by two coherently coupled subsystems, viz., the subsystem of Fermi atoms in a BCS-type state and the subsystem of Bose quasimolecules in the condensate state. In addition, Ψ_0 contains both a state of quasimolecules with a nonzero momentum of the center of mass ($k \neq 0$) and a state of pairs of atoms with a nonzero total momentum. This form enables the variational procedure to initially involve above-condensate excited states (temperature $T = 0$), which play a significant role in the formation of the ground state of the system in the general case. The resulting system of equations makes it possible, in particular, to find the gap in the single-particle excitation spectrum, as well as the speed of sound characterizing the branch of collective Bose excitations, and, hence, to determine the critical velocity.

In this paper, we will write explicitly the solution of this system of equations for the limiting cases permitting an analytical solution under the assumption that the resonant interaction constant is small. Numerical solution for the general case will be presented in a separate publication.

To make our analysis maximally clear, we consider a homogeneous system. The exchange between the subsystems of Fermi atoms and quasimolecules with the conservation of the total number of atoms is responsible for the existence of a unified chemical potential μ. Then, the generalized Hamiltonian of this system can be written in the form

$$\hat{H}' = \hat{H} - \mu\hat{N}$$
$$= \sum_{p,\sigma}\xi_p\hat{a}_{p\sigma}^+\hat{a}_{p\sigma} + \sum_k \zeta_k\hat{b}_k^+\hat{b}_k + \hat{V} + \hat{V}_a' + \hat{V}_a''. \quad (1)$$

Here, $\hat{a}_{p\sigma}$ is the absorption operator of a Fermi atom in the open channel, where the subscript $\sigma = 1, 2$ identifies the hyperfine state of the atom in the two-component mixture; $\hat{b}_k$ is the absorption operator for quasimolecules; and

$$\xi_p = \hbar^2 p^2/2m - \mu,$$
$$\zeta_k = \zeta_0 + \hbar^2 k^2/4m, \quad \zeta_0 = \varepsilon_0 - 2\mu,$$

where ε_0 is the position of the resonance level in the closed channel and m is the mass of the atom (we disregard the difference in the hyperfine energies in states 1 and 2). The operator

$$\hat{V} = g\sum_{p,k}(\hat{b}_k^+\hat{a}_{k/2-p,2}\hat{a}_{k/2+p,1} + \hat{a}_{k/2+p,1}^+\hat{a}_{k/2-p,2}^+\hat{b}_k) \quad (2)$$

corresponds to the resonant exchange interaction between particles in the open and closed channel. (Hereinafter, we assume that the volume is $\Omega = 1$.)

From the nonresonant interaction between atoms in the open channel, the interaction of pairs with zero total momentum is explicitly separated in Eq. (1):

$$\hat{V}_a' = U_0\sum_{p_1,p_2}\hat{a}_{p_1,1}^+\hat{a}_{-p_1,2}a_{-p_2,2}a_{p_2,1}, \quad (3)$$

$$\hat{V}_a'' = U_0\sum_{p_1,p_2,q\neq0}\hat{a}_{p_1,1}^+a_{q-p_1,2}^+a_{q-p_2,2}a_{p_2,1}. \quad (4)$$

Hamiltonian (1) in fact coincides with that widely used in analysis of gases under the FR conditions (see, e.g., [19–23]). The only difference is that interaction (4), whose role may be significant in the general case, is taken into account. Strictly speaking, the terms describing the nonresonant interaction of atoms with quasimolecules and between quasimolecules are omitted in Hamiltonian (1). However, both these interactions are generated by resonant interaction (2).

We choose the many-particle variational function in the form

$$\Psi_0 = \hat{\Psi}_M\hat{\Psi}_M'\hat{\Psi}_A|0\rangle. \quad (5)$$

The field operator of atoms can be represented in the conventional form

$$\hat{\Psi}_A = \prod_p[u_p + v_p\hat{a}_{p,1}^+\hat{a}_{-p,2}^+].$$

In the coherent representation, the field operator of quasimolecules (under the assumption that the number M_0 of such quasimolecules is large) in the state $k = 0$ has the form

$$\hat{\Psi}_M = e^{-\frac{1}{2}M_0}\exp(\sqrt{M_0}\hat{b}_0^+).$$

A distinguishing feature of the structure of the many-particle variational function given by Eq. (5) is that it includes the states associated with the virtual production of excited quasimolecules. The corresponding operator is represented in the form

$$\hat{\Psi}_M' = \prod_{k\neq0}\left[F_k + G_k\sum_p\hat{b}_k^+\hat{a}_{k/2-p,2}\hat{a}_{k/2+p,1}\right].$$

Note that the sequence of operators appearing in relation (5) is important: operator $\hat{\Psi}_M'$ acts on the state

arising as a result of the action of the operator $\hat{\Psi}_A$ on vacuum. The normalization of function (5) leads to the two relations

$$u_p^2 + v_p^2 = 1, \quad F_k^2 + w_k G_k^2 = 1, \tag{6}$$

where

$$w_k = \sum_p v_{p+k/2}^2 v_{p-k/2}^2. \tag{7}$$

(We assume that the coefficients u_p, v_p, F_k, and G_k are real-valued.)

The variational procedure can be reduced to finding the energy

$$\bar{E} = \langle \Psi_0 | \hat{H}' | \Psi_0 \rangle$$

and to its variation in functions v_p, G_k, and M_0 taking into account relations (6). Taking into account the structure of variational function (5) and the form of Hamiltonian (1), we obtain

$$\bar{E} = 2\sum_p \xi_p v_p^2 + \zeta_0 M_0 + 2\sqrt{M_0} \sum_p g u_p v_p$$

$$+ \sum_{k \neq 0} w_k (\zeta_k G_k^2 + 2g G_k F_k) \tag{8}$$

$$+ U_0 \left(\sum_p u_p v_p \right)^2 + U_0 \left(\sum_p v_p^2 \right)^2.$$

In the unit volume considered here, the value of M_0 is in fact equal to the density of quasimolecules with $k = 0$.

In consistent derivation of formula (8), functions v_p^2 are multiplied by the factor $\exp(-z_p)$, while functions $u_p v_p$ are multiplied by the factor $\exp(-2z_p)$, where $z_p = \sum_k G_k^2 v_p^2 v_{p-k}^2$. Direct computations show that the value of z_p is much smaller than unity (at least, in the range of the parameters we are interested in) and the inclusion of these factors virtually does not affect the results of the variational procedure; we assume that these factors are equal to unity.

By varying v_p, we obtain

$$\frac{\delta \bar{E}}{\delta v_p} = 4\xi_p v_p$$

$$+ \left(u_p - \frac{v_p^2}{u_p} \right) \left[2\sqrt{M_0} g + 2U_0 \sum_{p'} u_{p'} v_{p'} \right]$$

$$+ 4U_0 v_p \sum_{p'} v_{p'}^2 \tag{9}$$

$$+ \sum_{k \neq 0} \frac{\partial w_k}{\partial v_p} \left(\zeta_k G_k^2 + 2g G_k F_k - g w_k \frac{G_k^3}{F_k} \right) = 0.$$

Variation in G_k taking into account relations (6) gives

$$\frac{\delta \bar{E}}{\delta G_k} = \frac{2w_k}{F_k} [\zeta_k G_k F_k + g - 2g w_k G_k^2] = 0. \tag{10}$$

Using this equation and the relation following from Eq. (7),

$$\partial w_k / \partial v_p = 4 v_{p-k}^2 v_p,$$

we can write Eq. (9) in the form

$$2\xi_p' u_p v_p + (1 - 2v_p^2) \left[\sqrt{M_0} g + U_0 \sum_{p'} u_{p'} v_{p'} \right] = 0. \tag{11}$$

Here,

$$\xi_p' = \xi_p + d_p,$$

$$d_p = \sum_{k \neq 0} v_{p-k}^2 g G_k F_k + U_0 \sum_{p'} v_{p'}^2. \tag{12}$$

Finally, by varying M_0, we obtain

$$\zeta_0 + g \frac{1}{\sqrt{M_0}} \sum_p u_p v_p = 0. \tag{13}$$

The extremum defined by conditions (10), (11), and (13) corresponds to the energy minimum under the conditions

$$g u_p v_p < 0, \quad g G_k F_k < 0.$$

Therefore, the first term in relation (12) and the second term in relation (13) are negative. For definiteness, we will henceforth assume that $g > 0$.

Let us introduce the notation

$$\Delta = g\sqrt{M_0} + U_0 \sum_p u_p v_p.$$

Solving Eq. (11) together with relations (6), we arrive at expressions analogous to those in the BCS theory:

$$v_p^2 = \frac{1}{2} \left(1 - \frac{\xi_p'}{E_p} \right), \quad u_p^2 = \frac{1}{2} \left(1 + \frac{\xi_p'}{E_p} \right),$$

$$2u_p v_p = -\frac{\Delta}{E_p}, \quad E_p = \sqrt{\xi_p'^2 + \Delta^2}. \tag{14}$$

The equation for the gap Δ assumes the form

$$\Delta + \frac{1}{2} U_0 \sum_p \frac{\Delta}{E_p} = g\sqrt{M_0}. \tag{15}$$

Equation (13) is also transformed to the form

$$\varepsilon_0 - 2\mu = \frac{1}{2}g\frac{1}{\sqrt{M_0}}\sum_p \frac{\Delta}{E_p}. \tag{16}$$

It is interesting that the role of the virtual excited quasi-molecules in relations (15) and (16) is reduced to renormalization of the atomic spectrum [see Eqs. (12) and (14)].

Solving Eq. (10) with allowance for relations (6), we directly obtain

$$G_k^2 = \frac{1}{2w_k}\left(1 - \sqrt{\frac{\zeta_k^2}{\zeta_k^2 + 4g^2 w_k}}\right). \tag{17}$$

Equations (15) and (16) formally contain the integral diverging at the upper limit. This divergence is associated with the method of the introduction of the parameters ε_0, g, and U_0 in Hamiltonian (1). In the general case, this requires upper cutoff of the region of momenta, in which the interaction is effectively realized. However, in some important cases, such a cutoff appears naturally.

Let us consider the most interesting case, where the resonant interaction ($U_0 = 0$) plays a decisive role. In this case, Eq. (15) assumes the form

$$\Delta_0 = g\sqrt{M_0}. \tag{18}$$

The quantity ε_0 in Hamiltonian (1) corresponds to the position of the resonance level for $g = 0$. However, for $g \neq 0$, the energy of the level is renormalized in the limit of density tending to zero (i.e., in vacuum). This can be seen directly by calculating the scattering amplitude for a pair of atoms (with zero total momentum) in this limit, which is determined by interaction (2). Summing the perturbation series for $E \longrightarrow 0$, we obtain (cf. [23])

$$f(E) = -\frac{\hbar s/\sqrt{m}}{E - \varepsilon_0 + \frac{1}{2}g^2\sum_p \varepsilon_p^{-1} + is\sqrt{E}},$$

$$s = \frac{m^{3/2}}{4\pi\hbar^3}g^2.$$

It can be seen that, for $g \neq 0$, the resonance level energy is renormalized and assumes the following value:

$$\tilde{\varepsilon}_0 = \varepsilon_0 - \frac{1}{2}g^2\sum_p \frac{1}{\varepsilon_p}. $$

In the many-particle problem, it is natural to treat the quantity $\tilde{\varepsilon}_0$ as the actual position of the resonance level. Subtracting $\frac{1}{2}g^2\sum_p \frac{1}{\varepsilon_p}$ from both sides of Eq. (16) and

taking into account relation (18), we obtain

$$\tilde{\varepsilon}_0 - 2\mu = \frac{1}{2}g^2\sum_p\left(\frac{1}{E_p} - \frac{1}{\varepsilon_p}\right). \tag{19}$$

The situation becomes more complicated if the nonresonant interaction is taken into account. However, considering Eqs. (15) and (16) together, we arrive at the following equation that is again free of divergence:

$$\tilde{\varepsilon}_0 - 2\mu = \frac{1}{2}g^2\sum_p\left(\frac{1}{E_p} - \frac{1}{\varepsilon_p}\right) - \frac{g^2}{U_0}\frac{(\Delta - \Delta_0)^2}{\Delta\Delta_0}. \tag{20}$$

Using the familiar relation between the quantity U_0 and the nonresonant scattering length a_{Bg} in order to go beyond the Born approximation (see [24]), Eq. (15) for the gap can be transformed to the form

$$\Delta + \frac{1}{2}\Delta\frac{4\pi\hbar^2}{m}a_{Bg}\sum_p\left(\frac{1}{E_p} - \frac{1}{\varepsilon_p}\right) = g\sqrt{M_0}. \tag{21}$$

For $g = 0$, this equation can be reduced to the equation known in the theory of superconductivity (see [13]). Assuming that the gas parameter is small in the case of a purely nonresonant interaction, the quantity U_0 in Eqs. (20) and (12) can be replaced by $4\pi\hbar^2 a_{Bg}/m$. Solving Eqs. (20), (21), and (17) together and using relations (6), (12), and (14), we derive the expressions for Δ, M_0, and G_k^2 as functions of the chemical potential μ for fixed values of g, a_{Bg}, and $\tilde{\varepsilon}_0$.

The values obtained in this way allow us to determine the number of atoms,

$$N_A = \sum_{p,\sigma}\langle\Psi_0|\hat{a}_{p\sigma}^+\hat{a}_{p\sigma}|\Psi_0\rangle$$

$$= 2\sum_p v_p^2 = \sum_p\left(1 - \frac{\xi_p'}{E_p}\right), \tag{22}$$

and the number of virtually excited molecules,

$$M' = \sum_{k\neq 0}\langle\Psi_0|\hat{b}_k^+\hat{b}_k|\Psi_0\rangle = \sum_{k\neq 0}w_k G_k^2. \tag{23}$$

The relation for the total number of atoms in the system,

$$N_A + 2M_0 + 2M' = N_t, \tag{24}$$

determines the equation for the chemical potential $\mu(N_t)$.

As a consequence, we can find the relative values N_A/N_t, M_0/N_t, and M'/N_t as functions of $\tilde{\varepsilon}_0/2\varepsilon_t$ for a fixed dimensionless parameter

$$\gamma = g\sqrt{N_t}/\varepsilon_t. \tag{25}$$

Here, ε_t is the Fermi energy corresponding to the total density of noninteracting atoms, which is equal to N_t. It should be specially noted that the obtained system of equations is valid only in the interval of $\varepsilon_0/2\varepsilon_t$, where the condition $M_0 \gg 1$ holds.

The following remark is appropriate here. In a strongly interacting many-particle system, the superposition type of the ground state near the FR makes the definitions of "atoms" and "molecules" rather conditional. In fact, these are the projections of the many-particle wave function on the corresponding state.

Here, we write the solution to the obtained system of equations in some limiting cases permitting an analytical description. Let us first assume that $g \longrightarrow 0$ and $U_0 > 0$. In this case, it follows from Eq. (21) that $\Delta = 0$ and from Eq. (17) that $G_k = 0$.

In accordance with Eq. (20), the chemical potential is $\mu = \tilde{\varepsilon}_0/2$ under these conditions for an arbitrary $U_0 \neq 0$. The number of particles in the atomic subsystem is

$$N_A = 2\sum_p \theta(-\xi'_p),$$

where the quantity ξ'_p, in accordance with Eq. (12), is given by

$$\xi'_p = \frac{p^2}{2m} - \frac{1}{2}\tilde{\varepsilon}_0 + \frac{1}{2}U_0 N_A.$$

Taking into account relation (24) and the fact that $M'_{g=0} = 0$, we immediately find that the gas of atoms in the normal state is in equilibrium with the condensate of quasimolecules in the interval

$$0 < \frac{1}{2}\tilde{\varepsilon}_0 < \varepsilon_t + \frac{1}{2}U_0 N_t. \tag{26}$$

At the left boundary, for $\tilde{\varepsilon}_0 \longrightarrow 0$, the number of atoms is $N_A \longrightarrow 0$ and all the particles are in the condensate of quasimolecules. As $\tilde{\varepsilon}_0$ increases, M_0 decreases continuously and $N_A = N_t$ at the right boundary of interval (26); in other words, a purely atomic phase is formed. For $U_0 < 0$, the behavior of M_0 and N_A remains qualitatively the same, but the condensate of quasimolecules disappears earlier (approximately at $\frac{1}{2}\tilde{\varepsilon}_0 \simeq \varepsilon_t - \frac{1}{2}|U_0|N_t$) as ε_0 increases. This shift is some larger due to the emergence of the gap Δ in the atomic spectrum, which can be determined by solving Eq. (21) for $g \longrightarrow 0$.

Let us now consider the solution of the above system of equations in the case where the resonant interaction dominates and omit the terms containing U_0. We consider only g values corresponding to the small dimensionless parameter $\gamma \ll 1$. In this case, in accordance with Eqs. (18) and (25), $\Delta/\varepsilon_t = \gamma\sqrt{M_0/N_t} \ll 1$.

We can directly verify that $|d_p| \sim \gamma^m$, $m \geq 5/2$ in Eq. (12), and disregard the renormalization of the spectrum. Let us begin with the interval $\tilde{\varepsilon}_0 \gg \Delta$. In this case, Eqs. (19) immediately lead to

$$\mu = \frac{1}{2}\tilde{\varepsilon}_0 - \frac{3}{8}\gamma^2(\mu\varepsilon_t)^{1/2}\ln(\mu/\Delta). \tag{27}$$

Expression (22) yields the number of atoms

$$\frac{N_A}{N_t} = \left(\frac{\mu}{\varepsilon_t}\right)^{3/2} + O\left(\frac{\Delta^2}{\mu^2}\right).$$

Calculating w_k (7) and G_k^2 (17) in the limit $\tilde{\varepsilon}_0 \gg \Delta$, we arrive at the following expression for the number (23) of quasimolecules above the condensate:

$$\frac{2M'}{N_t} \simeq \frac{1}{2}\gamma^{3/2}\left(\frac{\mu}{\varepsilon_t}\right)^{9/8}.$$

Using relation (24), we obtain the number of condensate quasimolecules

$$\frac{2M_0}{N_t} \simeq 1 - \left(\frac{\mu}{\varepsilon_t}\right)^{3/2} - \frac{1}{2}\gamma^{3/2}\left(\frac{\mu}{\varepsilon_t}\right)^{9/8}. \tag{28}$$

The value $(\tilde{\varepsilon}_0/2\varepsilon_t)_*$ for which M_0 vanishes can be determined approximately omitting the second term in formula (27):

$$\left(\frac{\tilde{\varepsilon}_0}{2\varepsilon_t}\right)_* \simeq 1 - \frac{4}{3}\gamma^{3/2}. \tag{29}$$

In a narrow interval $\sim\gamma^{3/2}$, the number M' of excited quasimolecules near this boundary is found to be larger than M_0. With decreasing $\tilde{\varepsilon}_0$, the number M_0 of condensate particles increases rapidly and $M_0 \gg M'$.

Let us now find the speed of sound C in the system. In the case of an equilibrium exchange by atoms between the two subsystems, the speed of sound is determined by the thermodynamic relation

$$C^2 = \frac{N_t}{m}\frac{\partial\mu}{\partial N_t}, \tag{30}$$

which is characteristic of one-component systems (see, e.g., [24]). For $g \longrightarrow 0$, we have $C^2 = 0$. This result is a consequence of the passage of Fermi particles under compression to the quasimolecular subsystem leading to the relation $\partial p/\partial\rho = 0$.

A similar effect takes place in an ideal Bose gas at $T < T_c$, when some above-condensate particles overpass to the condensate upon an increase in pressure.

When calculating the derivative $\partial\mu/\partial N_t$, only the dependence of Δ on M_0 in the argument of the logarithm turns out to be significant [inclusion of the dependence

of the second term in relation (27) on μ gives the corrections $\sim\gamma^2$]:

$$\frac{\partial\mu}{\partial N_t} = \frac{3}{16}\gamma^2(\mu\varepsilon_t)^{1/2}\frac{1}{M_0}\frac{\partial M_0}{\partial N_t}.$$

We will use relation (28), omitting the last term on the right-hand side when determining the derivative $\partial M_0/\partial N_t$. The derivative acquires a term proportional to $(1/M_0)(\partial\mu/\partial N_t)$, which plays a significant role near the boundary given by Eq. (29) on the interval where M_0/N_t becomes on the order of γ^2. Returning to definition (30), we derive the general expression for the speed of sound:

$$C^2 = \frac{C_*^2}{1+\left(\dfrac{\mu}{\varepsilon_t}\right)^{1/2}\dfrac{3m}{2\varepsilon_t}C_*^2},$$

$$C_*^2 = \frac{3}{16}\gamma^2\frac{\varepsilon_t}{m}\left(\frac{\mu}{\varepsilon_t}\right)^{1/2}\frac{N_t}{M_0}. \tag{31}$$

Far from boundary (29), we have

$$C^2 = C_*^2. \tag{32}$$

In the limit $\mu \longrightarrow \varepsilon_t$, $M_0 \longrightarrow 0$, we obtain

$$c^2 = \frac{1}{3}\frac{2\varepsilon_t}{m}. \tag{33}$$

It is interesting that the limiting value is reached on the side of the region, where $M_0 \neq 0$ and the nonresonant interaction is absent. Thus, the speed of sound as a function of $\tilde{\varepsilon}_0/2\varepsilon_t$ increases continuously to value (33), which is typical of the collective oscillation of an ensemble of free Fermi particles. For $\gamma^2 \ll 1$, a sharp increase in C^2 to value (33) occurs on a narrow interval $\sim\gamma^2$.

Let us now consider the region $0 < \tilde{\varepsilon}_0 < \Delta$. In this limit, Eq. (19) assumes the form

$$\mu \simeq \frac{1}{2}\tilde{\varepsilon}_0 + 0.8g^2\frac{(2m)^{3/2}}{4\pi^2}\Delta^{1/2}. \tag{34}$$

Accordingly, from relation (22), we obtain

$$\frac{N_A}{N_t} \simeq 0.8\gamma^{3/2}\left(\frac{M_0}{N_t}\right)^{3/4}.$$

Determining M' from (23), we obtain

$$\frac{2M'}{N_t} \simeq \frac{1}{2}\gamma^{21/8}.$$

The resulting values immediately indicate that most particles in this region are in the condensate of quasi-molecules:

$$\frac{2M_0}{N_t} = 1 - \frac{1}{2}\gamma^{3/2} - \frac{1}{2}\gamma^{21/8}.$$

Using relations (30) and (34) for the speed of sound, we obtain

$$C^2 \simeq \frac{\varepsilon_t}{3m}\gamma^{5/2}. \tag{35}$$

It follows from relation (34) that the chemical potential vanishes for

$$\tilde{\varepsilon}_0 \simeq -\gamma^{5/2}\varepsilon_t.$$

To reveal the complete pattern, let us consider the region of negative values of $\tilde{\varepsilon}_0$, assuming that $\Delta \ll |\tilde{\varepsilon}_0|$. Naturally, real molecules dominate in this region. The admixture of atomic states is small:

$$\frac{N_A}{N_t} = \frac{3}{4}\gamma^2\left(\frac{2\varepsilon_t}{\tilde{\varepsilon}_0}\right)^{1/2}\frac{M_0}{N_t}. \tag{36}$$

The behavior of above-condensate molecules is analogous:

$$\frac{2M'}{N_t} \simeq \frac{1}{2}\gamma^3\left(\frac{2\varepsilon_t}{\tilde{\varepsilon}_0}\right)^{3/4}.$$

Accordingly, the number of molecules in the condensate is

$$\frac{2M_0}{N_t} \simeq 1 - \frac{3}{8}\gamma^2\left(\frac{2\varepsilon_t}{\tilde{\varepsilon}_0}\right)^{1/2} - \frac{1}{2}\gamma^3\left(\frac{2\varepsilon_t}{\tilde{\varepsilon}_0}\right)^{3/4}.$$

In this case, Eq. (19) is transformed to the form

$$\mu = \frac{1}{2}\varepsilon_0 + 0.55g^2\frac{m^{3/2}|\mu|^{1/2}}{\pi^2} + \frac{m^{3/2}}{32\pi|\tilde{\varepsilon}_0|^{3/2}}g^4M_0.$$

This relation, together with Eq. (25), leads to the following expression for the speed of sound:

$$C^2 \simeq \frac{3\pi}{256}\gamma^4\frac{\varepsilon_t}{m}\left(\frac{2\varepsilon_t}{|\tilde{\varepsilon}_0|}\right)^{3/2}. \tag{37}$$

A high power of the small parameter appears in this relation, because the interaction between molecules in the given case occurs via virtually produced Fermi atoms whose number is small [see Eq. (36)]. This explains the tendency of C^2 to zero for $|\tilde{\varepsilon}_0| \longrightarrow \infty$. Comparing relations (37), (35), (32), and (33), we see that the speed of sound increases monotonically with $\tilde{\varepsilon}_0$, reaching its maximal value (33).

The superfluidity and critical velocity v_c in the system under investigation are determined simultaneously by the spectrum of single-particle Fermi excitations and collective Bose excitations. Accordingly, v_c assumes the minimum value among the two velocities C and $\min(E_p/p)$ [E_p is defined by Eqs. (14)]. The critical velocity for $\tilde{\varepsilon}_0$ near $2\varepsilon_t$ is determined by Fermi excitations and $v_c \longrightarrow 0$ together with $M_0 \longrightarrow 0$ and $\Delta \longrightarrow 0$ [see Eq. (18)]. As $\tilde{\varepsilon}_0$ decreases, the velocity $\min(E_p/p)$ increases monotonically, while the speed of

sound, on the contrary, decreases. The critical velocity is again determined by single-particle excitations up to $\tilde{\varepsilon}_0/2\varepsilon_t \simeq 1/3$. For smaller $\tilde{\varepsilon}_0/2\varepsilon_t$ values, including the range of negative $\tilde{\varepsilon}_0$ values, the critical velocity is determined by the speed of sound.

REFERENCES

1. E. Tiesinga, B. J. Verhaar, and H. T. C. Stoof, Phys. Rev. A **47**, 4114 (1993).
2. C. A. Regal, G. Ticknor, J. L. Bohn, and D. S. Jin, Nature **424**, 47 (2003).
3. K. E. Strecker, G. B. Partrige, and R. G. Hulet, Phys. Rev. Lett. **91**, 080 406 (2003).
4. S. Jochim *et al.*, Phys. Rev. Lett. **91**, 240402 (2003).
5. J. Cubizolles *et al.*, Phys. Rev. Lett. **91**, 240401 (2003).
6. D. S. Petrov, C. Solomon, and G. V. Shlyapnikov, Phys. Rev. Lett. **93**, 090404 (2004).
7. M. Greiner, C. A. Regal, and D. S. Jin, Nature **426**, 537 (2004).
8. S. Jochim *et al.*, Science **302**, 2101 (2003).
9. M. W. Zwierlein *et al.*, Phys. Rev. Lett. **91**, 250401 (2003).
10. T. Bourdel *et al.*, Phys. Rev. Lett. **93**, 050401 (2004).
11. M. Holland *et al.*, Phys. Rev. Lett. **87**, 120406 (2001).
12. E. Timmermans *et al.*, Phys. Lett. A **285**, 228 (2001).
13. A. J. Leggett, in *Modern Trends in Theory of Condensed Matter* (Springer, Berlin, 1980), p. 13.
14. P. Nozières and S. Schmitt-Rink, J. Low Temp. Phys. **59**, 195 (1985).
15. G. Ortiz and J. Dukelsky, cond-mat/0503664 (2005).
16. C. A. Regal, M. Greiner, and D. S. Jin, Phys. Rev. Lett. **92**, 040403 (2004).
17. M. W. Zwierlein *et al.*, Phys. Rev. Lett. **92**, 120403 (2004).
18. M. W. Zwierlein *et al.*, cond-mat/0412675 (2004).
19. Y. Ohashi and A. Griffin, Phys. Rev. A **67**, 063612 (2003); Phys. Rev. Lett. **89**, 130402 (2002).
20. J. Stajic *et al.*, Phys. Rev. A **69**, 063610 (2004).
21. G. M. Bruun and C. J. Pethick, Phys. Rev. Lett. **92**, 140404 (2004).
22. G. M. Falco and H. T. C. Stoof, Phys. Rev. Lett. **92**, 130401 (2004).
23. A. V. Andreev, V. Gurarie, and L. Radzihovsky, Phys. Rev. Lett. **93**, 130402 (2004).
24. E. M. Lifshitz and L. P. Pitaevskiĭ, *Statistical Physics* (Fizmatlit, Moscow, 2000; Butterworth, Oxford, 1998), Part 2.

Translated by N. Wadhwa

Amplification of Longitudinal Ultrasonic Waves by a Moving Vortex Structure in Type II Superconductors

E. D. Gutliansky

Institute of Physics, Rostov State University, Rostov-on-Don, 344010 Russia

e-mail: gutlian@ip.rsu.ru

Received November 24, 2004; in final form, April 26, 2005

A moving vortex structure can amplify (generate) longitudinal acoustic waves when the velocity of its motion exceeds a certain critical velocity. The critical velocity is determined by the logarithmic derivative of the viscosity coefficient of the vortex structure with respect to the magnetic field and may be much smaller than the speed of sound. In particular, this effect suggests an alternative explanation for the plateau observed in the current–voltage characteristic of superconducting bridges in a perpendicular magnetic field [S.G. Doettinger *et al.*, Phys. Rev. Lett. **73**, 1691 (1994)]. © *2005 Pleiades Publishing, Inc.*

PACS numbers: 72.50.+b, 74.40.+k, 74.60.Ec

It is well known that the interaction of waves propagating in a physical system with objects moving in the same system at a velocity exceeding the phase velocity of waves leads to the amplification of these waves. Examples of such systems are a traveling-wave tube [1] (electromagnetic wave amplification) and a piezoelectric semiconductor (ultrasonic wave amplification [2]). In both cases, the amplification is a result of the interaction of waves with the electron flow. Recently [3], it was shown that the motion of the vortex structure in a superconductor at a velocity greater than the speed of sound can amplify longitudinal ultrasonic waves.

The aim of this study is to demonstrate that a superconductor with a moving vortex structure is a system violating the following common concept: for the observation of wave amplification, it is necessary to have a subsystem moving with a velocity higher than the phase velocity of the waves. Below, it is shown that the amplification (generation) of longitudinal ultrasonic waves in such superconductors can also be observed when the vortex structure moves with velocities much smaller than the wave velocity. This effect suggests a new interpretation of the plateau that is observed in the current–voltage characteristics of superconducting bridges (see, e.g., [4, 5]).

The interaction of ultrasonic waves with a stationary vortex structure has been much investigated [6–15]. In [8, 20], it was shown that an ultrasonic wave may entrain the vortex structure. This phenomenon was also observed experimentally [17–19].

Let us derive the equations of motion for the vortex structure of a superconductor. The gradient-invariant expression for the current $\mathbf{J}_s$ of the superfluid electron liquid in the laboratory frame of reference has the form

$$\mathbf{J}_s = \frac{1}{\lambda_L^2 \mu_0}\left(\frac{\phi_0}{2\pi}\nabla\Phi - \mathbf{A}\right). \tag{1}$$

Here, $\mathbf{\Phi}$ and $\mathbf{A}$ are the phase of the order parameter and the vector potential ($\mathbf{B} = \nabla\times\mathbf{A}$, where $\mathbf{B}$ is the magnetic induction), and λ_L, ϕ_0, and μ_0 are the London penetration depth, the magnetic flux quantum, and the magnetic constant, respectively. Taking the vector product of Eq. (1) by operator ∇, we obtain

$$\nabla\times\mathbf{J}_s = \frac{1}{\lambda_L^2 \mu_0}\left(\frac{\phi_0}{2\pi}\nabla\times\nabla\Phi - \nabla\times\mathbf{A}\right). \tag{2}$$

Let us introduce the induction vector $\mathbf{B}_v$ of the vortex lattice so that its magnitude is equal to $\phi_0 n_v$, where n_v is the two-dimensional vortex density (i.e., the number of vortices per unit area in the plane perpendicular to the vortex lines) and its direction is determined by the vector tangential to the vortex line. In the presence of vortices, the phase of the order parameter is a multivalued function and the phase circulation over a certain closed contour l is determined by the number of vortices passing through the contour:

$$\frac{\phi_0}{2\pi}\int\nabla\Phi d\mathbf{l} = \int\mathbf{B}_v d\mathbf{s},$$

where $\int d\mathbf{s}$ is the integral over the surface spanning the contour l. According to the Stokes theorem, this expression can be represented in the form

$$\frac{\phi_0}{2\pi}\int \nabla \times \nabla \Phi d\mathbf{s} = \int \mathbf{B}_v d\mathbf{s},$$

which, by virtue of the arbitrary choice of the contour, yields $\dfrac{\phi_0}{2\pi}\nabla \times \nabla \Phi = \mathbf{B}_v$. For the subsequent calculation, it is necessary to express Eq. (2) in terms of macroscopic electrodynamics. For this purpose, we write the equation for the total current in the laboratory frame of reference. In view of the accepted assumptions, this equation can be written as

$$\mathbf{J} = \mathbf{J}_s - q n_s \dot{\mathbf{U}}; \tag{3}$$

where $-q n_s \dot{\mathbf{U}}$ is the current caused by the motion of the ionic lattice in the laboratory frame of reference and $\mathbf{U}$ is the strain vector of the ionic lattice.

Substituting Eq. (3) into Eq. (1) with allowance for the Maxwell equations

$$\nabla \times \mathbf{E} = -\partial \mathbf{B}/\partial t, \tag{4}$$

$$\nabla \times \mathbf{H} = \mathbf{j}, \tag{5}$$

after simple transformations, we obtain

$$\mathbf{B} - \lambda_L^2 \nabla^2 \mathbf{B} + \frac{m}{q}\nabla \times \dot{\mathbf{U}} = \mathbf{B}_v. \tag{6}$$

Differentiating Eq. (6) with respect to time and taking into account the continuity equation for $\mathbf{B}_v$,

$$\partial \mathbf{B}_v/\partial t = \nabla \times (\dot{\mathbf{W}} \times \mathbf{B}_v), \tag{7}$$

we reduce Eq. (6) to the form

$$\frac{\partial}{\partial t}\left(-\lambda_L^2 \nabla^2 \mathbf{B} + \mathbf{B} + \frac{m}{q}\nabla \times \dot{\mathbf{U}}\right) = \nabla \times (\dot{\mathbf{W}} \times \mathbf{B}_v), \tag{8}$$

where $\dot{\mathbf{W}}$ is the local velocity of the vortex lattice. This equation was derived earlier in a different way in constructing the theory of the acoustoelectric effect [20].

Below, for definiteness, we consider a homogeneous isotropic superconductor in an external magnetic field that is oriented in the negative direction of the z axis and produces an induction $\mathbf{B}_v = \mathbf{B}_0$ in the superconductor in the absence of the ultrasonic wave. A longitudinal ultrasonic wave propagates in the superconductor in the positive direction of the y axis and has the form $\mathbf{U} = \mathbf{U}_0 \exp(i k y - i \omega t)$, where $\mathbf{k}$ is the wave vector, $\omega = 2\pi f$, and f is the frequency of the ultrasonic wave. The superconductor contains a vortex structure, which moves with a velocity $\mathbf{V}$ in the direction of the ultrasonic wave propagation. The propagating ultrasonic wave causes oscillations of the vortex structure density, ΔB_v, around its equilibrium value $\mathbf{B}_0$ determined by the external

magnetic field. Below, we assume that $\mathbf{B}_0$ is independent of coordinates.[1] Hence, we represent $\mathbf{B}_v$ as the sum $\mathbf{B}_v = \mathbf{B}_0 + \Delta \mathbf{B}_v$, while the local velocity of the moving vortex structure can be represented as $\dot{\mathbf{W}} = \mathbf{V} + \dot{\mathbf{W}}'$, where $\mathbf{V}$ and $\dot{\mathbf{W}}'$ are the constant (the velocity of the vortex structure moving as a whole) and variable components of the vortex structure, respectively. Substituting these definitions into Eq. (8) and taking into account that the subsequent consideration refers to harmonic waves, we obtain

$$\mathbf{B} - \lambda_L^2 \nabla^2 \mathbf{B} = -\frac{m}{q}\nabla \times \dot{\mathbf{U}} + \nabla \times (\mathbf{W}' \times \mathbf{B}_0)$$
$$+ \frac{1}{-i\omega}\nabla \times (\mathbf{V} \times \Delta \mathbf{B}_v). \tag{9}$$

Solving Eq. (9) for $\mathbf{B}$ and using Eq. (5), we arrive at the expression for the total current induced by the motion of the vortex structure and by the oscillations of the ionic lattice of the superconductor:

$$\mathbf{J} = \frac{1}{\mu_0(1 + (\lambda_L k)^2)}$$
$$\times \left[(\mathbf{W}' \times \mathbf{B}_0)k^2 - \frac{1}{i\omega}(\mathbf{V} \times \Delta \mathbf{B}_v)k^2\right]. \tag{10}$$

Now, let us write the local equation of motion for the vortex structure (we ignore the inertial mass of a vortex) by deriving it from the force balance condition $\mathbf{F}_{fr} = \mathbf{F}_L$, where $\mathbf{F}_L = \mathbf{J}_s' \times \mathbf{B}_v$ is the Lorentz force, $\mathbf{F}_{fr} = \eta(\dot{\mathbf{W}} - \dot{\mathbf{U}}) - \tilde{\eta}(\dot{\mathbf{W}} - \dot{\mathbf{U}}) \times \mathbf{B}_v$ is the friction force between the vortex structure and the crystal lattice of the superconductor, and $\mathbf{J}_s'$ is the current density in the local frame of reference connected with the vortex structure. Taking into account that $\mathbf{J}_s' = (\mathbf{J}_s - q n_s \dot{\mathbf{W}})$, we obtain the equation of motion for the vortex structure in the form

$$\eta(\dot{\mathbf{W}} - \dot{\mathbf{U}}) - \tilde{\eta}(\dot{\mathbf{W}} - \dot{\mathbf{U}}) \times \mathbf{B}_v = (\mathbf{J}_s - q n_s \dot{\mathbf{W}}) \times \mathbf{B}_v, \tag{11}$$

where η and $\tilde{\eta}$ are the longitudinal and transverse viscosity coefficients of the vortex structure, respectively. Here, $\tilde{\eta} = (q/h)\eta'$, where η' is the transverse viscosity coefficient for a single vortex. In a more convenient form, Eq. (11) is represented as follows:

$$\eta(\dot{\mathbf{W}} - \dot{\mathbf{U}}) + \alpha(\dot{\mathbf{W}} - \dot{\mathbf{U}}) \times \dot{\mathbf{B}}_v = \mathbf{J} \times \dot{\mathbf{B}}_v, \tag{12}$$

where $\alpha = q n_s - \tilde{\eta}$.

---

[1] In the case of a bulk superconductor, the condition for the quantity $\mathbf{B}_0$ to be independent of y is expressed as $\mu_0 J c_l / B_0 f \ll 1$. In the case of a film, the vortex structure is accelerated by the London currents and, therefore, a limitation is imposed on the film thickness: it should not exceed λ_L.

Equations (3), (7), (10), and (12) completely describe the motion of the vortex structure. For a complete description of the problem under study, these equations should be complemented with the equation of motion of the ionic lattice of the superconductor:

$$\rho\ddot{\mathbf{U}} = \rho c_t^2 \Delta\mathbf{U} + \rho(c_l^2 - c_t^2)\mathrm{grad\,div}\,\mathbf{U}$$
$$- q n_s \dot{\mathbf{U}} \times \mathbf{B} - q n_s \mathbf{E} + \mathbf{F}_{fr}, \qquad (13)$$

where ρ is the density of the superconductor and c_l and c_t are the velocities of longitudinal and transverse ultrasonic waves in the absence of the vortex structure. In Eq. (13), the third and fourth terms describe the effects of the electric and magnetic fields on the ionic lattice of the superconductor while the fifth term describes the effect of the friction forces. To solve the problem on the interaction of a moving vortex structure with the oscillations of the vortex lattice, it is necessary to determine the relation between the strain vector of the ionic lattice and the strain vector of the vortex lattice. This can be done by linearizing Eq. (11). In contrast to [3–16, 20, 21], we perform the linearization by taking into account the dependence of the viscosity coefficient η on B_v and expand $\eta(B_v)$ in a Taylor series at the point B_0 to the second-order terms in ΔB_v: $\eta = \eta_0 + \eta_{,B}\Delta B_v$, where $\eta_0 = \eta(B_0)$ is the zero-order term of the expansion of the viscosity coefficient in the vortex structure density oscillations and $\eta_{,B} = d\eta(B_v)/dB_v|_{B_0}$. Now, we consider the case of a contaminated superconductor and assume that the Magnus force is compensated for by the transverse friction forces: $\alpha = q n_s - \tilde{\eta} = 0$ (this assumption means that we ignore the Hall effect). As a result, we obtain two equations:

$$\eta_0 \mathbf{V} = \mathbf{J}_0 \times \mathbf{B}_0, \qquad (14)$$

$$\eta_0(\dot{\mathbf{W}}' - \dot{\mathbf{U}}) + \eta_B \Delta B \cdot \mathbf{V} = \mathbf{J} \times \mathbf{B}_0 + \mathbf{J}_0 \times \Delta\mathbf{B}_v. \quad (15)$$

Equation (14) allows one to determine the current that should be passed through the superconductor to accelerate the vortex structure to the velocity V. Equation (15) describes the oscillations of the vortex structure and its interaction with the ultrasonic wave. Using the local continuity equation, it is possible to determine $\Delta\mathbf{B}_v$:

$$\Delta\mathbf{B}_v = -\frac{i\omega \mathbf{k}(\mathbf{W}' - \mathbf{U})}{\omega - Vk}\mathbf{B}_0. \qquad (16)$$

Substituting Eq. (16) into Eqs. (15) and (10) and substituting Eq. (10) into Eq. (15), we obtain

$$\eta_0(\dot{\mathbf{W}}' - \dot{\mathbf{U}}) = -Dk^2\mathbf{W}'$$
$$+ \frac{1}{i\omega}\frac{Vk}{\omega - Vk}(Dk^2 + i\omega\beta\eta_0)(\dot{\mathbf{W}}' - \dot{\mathbf{U}}). \qquad (17)$$

Here, $D = B_0^2/\mu_0(1 + \lambda_L^2 k^2)$ and $\beta = 1 - \eta_{,B}B_0/\eta_0$; note that $D \approx C_{11}$, where C_{11} is the longitudinal elastic mod-

ulus of the vortex lattice [6]. If we set $V = 0$, Eq. (17) will coincide with the equation of motion of the vortex structure that was proposed in [6] and, hence, it will coincide with the dispersion law for the eigenmodes of the vortex lattice, which were obtained in [11, 13].

Solving Eq. (17) together with the linearized Eq. (13) and Eqs. (3)–(5), we obtain the expressions for the relative velocity variation $\Delta c_l/c_l$ and additional attenuation α_{at} that occur in the longitudinal wave because of the interaction with the vortex structure:

$$\frac{\Delta c_l}{c_l} = \frac{1}{2}\left(1 - \beta\frac{V}{c_l}\right)\left(1 - 2\gamma\frac{V}{c_l}\right)\frac{\omega^2}{\rho c_l^2}$$
$$\times \frac{D}{\left(1 - 2\gamma\frac{V}{c_l}\right)^2\omega^2 + X^2}, \qquad (18)$$

$$\alpha_{at} = \frac{1}{2}\frac{\omega^2}{\rho c_l^3}\left(1 - \beta\frac{V}{c_l}\right)D\frac{X}{\left(1 - 2\gamma\frac{V}{c_l}\right)^2\omega^2 + X^2}, \quad (19)$$

where

$$X = \frac{D}{\eta_0}k^2, \quad D = B_0^2/\mu_0(1 + \lambda_L^2 k^2), \quad \gamma = 1 + \frac{1}{2}\frac{\eta_{,B}B_0}{\eta_0}.$$

From expressions (18) and (19), one can see that both the attenuation coefficient and the relative variation of the sound velocity have two anomalous points: $V = \frac{c_l}{2\gamma}$ and $V = \frac{c_l}{\beta}$. At $V = \frac{c_l}{2\gamma}$, a change of sign occurs in the relative variation of the sound velocity and an anomalous attenuation takes place because of the interaction with the vortex structure. These effects are related to the appearance of a new collective mode of the vortex structure. The new mode exists only for the vortex structure in motion. When the velocity of the vortex structure exceeds the critical velocity $V_c = \frac{c_l}{\beta}$, the amplification of ultrasonic waves is observed. A generation arises as a result of the amplification of longitudinal ultrasonic waves caused by thermal fluctuations. The effect of the longitudinal ultrasonic wave generation manifests itself, in particular, as a plateau in the current–voltage characteristic when the vortex structure reaches this velocity. The comparison of the results obtained above with the results reported in [3–16, 20, 21] shows that the inclusion of the dependence of the viscosity coefficient on the vortex structure density in the consideration leads to a renormalization of both the velocity of the vortex structure at which the anomalous increase in the attenuation of ultrasound is observed and the critical velocity of the vortex structure at which the amplification of ultrasound is possible. As follows from the results of this study, the sign of the difference between the critical velocity of the vortex struc-

ture and the velocity of the ultrasonic waves in the superconductor depends on the sign of the derivative of the viscosity coefficient. In particular, in the field and temperature region where the viscosity coefficient is proportional to B_v, the amplification (generation) of ultrasonic waves is absent. From physical considerations, one can expect that the derivative of the viscosity coefficient should be negative when either the density of the vortex structure or its velocity is sufficiently high. Therefore, the critical velocity at which the aforementioned effects are observed will be less than the speed of sound.

In a series of publications (see, e.g., [4, 5]), the authors reported on the observation of a plateau in the current–voltage characteristics of both low-temperature [4] and high-T_c superconducting films. The plateau appeared when the velocity of the vortex structure reached a certain critical value. This phenomenon was interpreted on the basis of the Larkin–Ovchinnikov effect [22]. According to the above consideration, when the velocity of the vortex structure exceeds the value of c_l/β, the vortex structure begins generating ultrasonic waves. This effect should also manifest itself as a considerable decrease in the slope of the current–voltage characteristic of a given superconductor. Therefore, it is possible that, in some of the experiments on measuring the current–voltage characteristics, the effect proposed in this paper manifests itself together with the Larkin–Ovchinnikov effect [22]. To verify this hypothesis experimentally, it is necessary to measure the current–voltage characteristic and simultaneously measure the acoustic emission, which should accompany the flattening of the current–voltage characteristic and the appearance of the plateau.

Below, for illustration, let us interpret the results of the experimental study [5] from the standpoint of the proposed hypothesis. In this experiment, the current–voltage characteristic was measured for a YBaCuO film bridge on an MgO substrate. We assume that the plateau of the current–voltage characteristic begins as soon as the critical velocity of the vortex structure coincides with the velocity of the surface acoustic wave (SAW) propagating over the substrate. We estimate the critical velocity and compare the result with the experimental value of the critical velocity. For estimating, we use the Tinkham empirical formula [23] for the conductivity of a YBaCuO superconductor in the mixed state:

$r = r_0 I_0^{-2} (\gamma_0/2)$, where $\gamma_0 = 1/2 \times 10^3 (1 - t)^{3/2} B^{-1}$ and $t = T/T_c$; here, T is the absolute temperature, T_c is the superconducting transition temperature, and the viscosity coefficient in the TAFF regime has the form $\eta = B^2/r$. The velocity of the SAW in MgO is 5×10^3 m/s [24]. For the external magnetic field, we chose a value of 1.8 T. The dots in the figure show the experimental values of the critical velocity [5]. In view of the fact that the calculation was performed using the empirical conductivity value, which was obtained for a bulk superconduc-
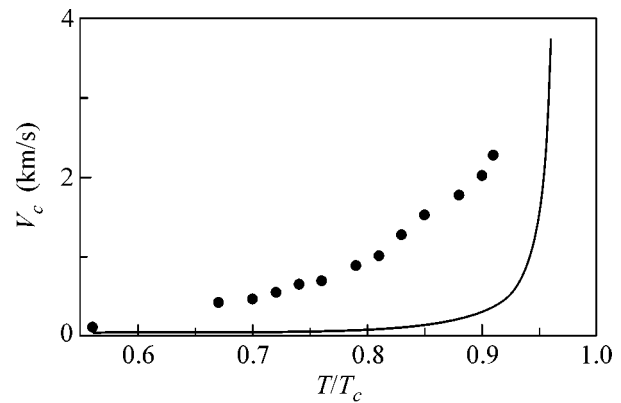
Relative-temperature dependence of the critical velocity of the vortex structure at a magnetic field induction of 1.8 T. The experimental data shown by points are taken from [5], and the solid line represents the calculation.

tor with a vortex structure moving with a low velocity, the agreement with the experiment can be considered as satisfactory.

Thus, the above consideration suggests the following conclusions: (i) a moving vortex structure can amplify or generate ultrasonic waves when the velocity of its motion is much smaller than the velocity of ultrasonic waves, and this velocity of motion is determined by the logarithmic derivative of the viscosity coefficient of the vortex structure with respect to magnetic induction, unlike the result obtained in [3]; (ii) this effect can manifest itself in the form of a plateau in the current–voltage characteristic of a superconducting film in the mixed state, and, possibly, such a manifestation already was observed in [5]; (iii) starting from the instant when the plateau of the current–voltage characteristic is reached, an acoustic emission should be observed.

REFERENCES

1. D. I. Trubetskov and A. E. Hramov, *Lectures on Microwave Electronics for Physicists* (Fizmatlit, Moscow, 2003) [in Russian].

2. A. R. Hutson, J. H. Mc Fee, and D. L. White, Phys. Rev. Lett. **7**, 237 (1961).

3. E. D. Gutliansky, Phys. Rev. B **66**, 52 511 (2002).

4. L. E. Musienko, I. M. Dmitrienko, and V. G. Volotskaya, Pis'ma Zh. Éksp. Teor. Fiz. **31**, 603 (1980) [JETP Lett. **31**, 567 (1980)].

5. S. G. Doettinger, R. P. Huebener, R. Gerdemann, *et al.*, Phys. Rev. Lett. **73**, 1691 (1994).

6. J. Pankert *et al.*, Phys. Rev. Lett. **65**, 3052 (1990).

7. E. D. Gutliansky, Fiz. Nizk. Temp. **18**, 428 (1992) [Sov. J. Low Temp. Phys. **18**, 290 (1992)].

8. E. D. Gutliansky, Pis'ma Zh. Éksp. Teor. Fiz. **59**, 459 (1994) [JETP Lett. **59**, 480 (1994)].

9. E. D. Gutliansky, Physica C (Amsterdam) **235–240**, 2080 (1994).

10. E. D. Gutliansky and T. V. Kolesnikova, Physica C (Amsterdam) **235–240**, 2078 (1994).

11. G. Blatter and B. Ivlev, Phys. Rev. B **52**, 4588 (1995).

12. D. Dominguez, B. Bulaevskii, B. Ivlev, *et al.*, Phys. Rev. Lett. **74**, 2579 (1995).

13. D. Dominguez, B. Bulaevskii, B. Ivlev, *et al.*, Phys. Rev. B **51**, 15 649 (1995).

14. D. Dominguez, B. Bulaevskii, B. Ivlev, *et al.*, Phys. Rev. B **53**, 6682 (1996).

15. E. D. Gutliansky, Fiz. Tverd. Tela (St. Petersburg) **38**, 1341 (1996) [Phys. Solid State **38**, 743 (1996)].

16. E. D. Gutliansky, Fiz. Tverd. Tela (St. Petersburg) **45**, 774 (2003) [Phys. Solid State **45**, 812 (2003)].

17. N. V. Zavaritskiĭ, Pis'ma Zh. Éksp. Teor. Fiz. **57**, 695 (1993) [JETP Lett. **57**, 707 (1993)].

18. Yu. V. Ilisavskiĭ, É. Z. Yakhkind, E. K. Gol'man, and A. P. Mitrofanov, Pis'ma Zh. Éksp. Teor. Fiz. **52**, 1138 (1990) [JETP Lett. **52**, 542 (1990)].

19. Yu. V. Ilisavskiĭ, É. Z. Yakhkind, E. K. Gol'man, and S. F. Karmanenko, Fiz. Tverd. Tela (Leningrad) **33**, 824 (1991) [Sov. Phys. Solid State **33**, 469 (1991)].

20. E. D. Gutliansky, Pis'ma Zh. Éksp. Teor. Fiz. **67**, 222 (1998) [JETP Lett. **67**, 239 (1998)].

21. E. B. Sonin, Phys. Rev. B **55**, 485 (1997).

22. A. I. Larkin and Yu. N. Ovchinnikov, Zh. Éksp. Teor. Fiz. **68**, 1915 (1975) [Sov. Phys. JETP **41**, 960 (1975)].

23. M. Tinkham, Phys. Rev. Lett. **61**, 1658 (1988).

24. A. A. Blistanov, V. S. Bondarenko, N. V. Perelomova, F. N. Strizhevskaya, V. V. Chkalova, and M. N. Shaskol'skaya, *Acoustic Crystals: Handbook* (Nauka, Moscow, 1982) [in Russian].

Translated by E. Golyamina

A Strongly Asymmetric Single-Electron Transistor Operating as a Zero-Biased Electrometer¶

V. A. Krupenin[1, *], D. E. Presnov[2], V. O. Zalunin[1], S. A. Vasenko[1], and A. B. Zorin[2, 3]

[1] Laboratory of Cryoelectronics, Moscow State University, Moscow, 119899 Russia
*e-mail: vkrup@cryoc49a.phys.msu.ru
[2] Nuclear Physics Institute, Moscow State University, Moscow, 119899 Russia
[3] Physikalisch-Technische Bundesanstalt, Braunschweig, 38116 Germany
Received June 6, 2005

We have studied a strongly asymmetric Al single-electron transistor with $R_1 \ll R_2$ and $C_1 \gg C_2$, where $R_{1,2}$ and $C_{1,2}$ are the tunnel resistances and capacitances of the first and second junction respectively. Due to the asymmetry in its electric parameters leading to strong asymmetry of the nonlinear I–V curve at zero bias ($V = 0$), the transistor demonstrated a remarkable current response to an AC signal at the values of the gate charge Q_0 close to $(n + 1/2)e$, where n is integer. A rather delicate regime of the transistor operation ($V \ll e/C_\Sigma$) being important for unperturbed measurements was examined. The measured curves are in good agreement with a model based on the orthodox theory of single electron tunneling. This specific zero bias regime of an asymmetric transistor opens new opportunities for a single-electron transistor as an ultrasensitive charge/field sensor. © 2005 Pleiades Publishing, Inc.

PACS numbers: 73.23.Hk, 73.40.Rw

INTRODUCTION

The single-electron tunneling (SET) transistor is a device consisting of two small tunnel junctions connected in series. Due to the close location of these junctions, they form a small common electrode (island), which is equipped with a capacitively coupled gate electrode [1]. Due to the remarkable correlation of the SET events in these junctions, which are governed by the Coulomb blockade effect, the current through the transistor periodically (the period is equal to the elementary charge *e*) depends on the charge induced on its island; consequently, the SET transistor can be used as an extremely sensitive electrometer (see, e.g., [1, 2]). Due to requirement of high yield in their manufacture, the metallic SET transistors are usually fabricated with tunnel junctions having almost equal areas; as a result, the transistors are nominally symmetric.

Recently, some useful features of asymmetric SET transistors were found experimentally by Weis *et al.* [3] and Walliser [4], who modeled the behavior of such transistors using numerical methods. One of these useful features is the possibility for an asymmetric transistor to operate as a sensitive electrometer even without any DC voltage bias when a current response is generated by an AC or *noise* signal. In this paper, we applied a special technique for the fabrication of strongly asymmetric SET transistors [5] allowing formation of the transistor junctions not only with different areas but also with different transparencies of their barriers.

Using this technology, we fabricated and measured an asymmetric Al/AlO$_x$/Al SET transistor in the regimes of small DC and AC bias which are important for delicate measurements. We modeled the transistor behavior applying the orthodox theory of SET [6]. Some of the transistor characteristics are expressed in a simple analytical form, while others are calculated numerically and presented graphically.
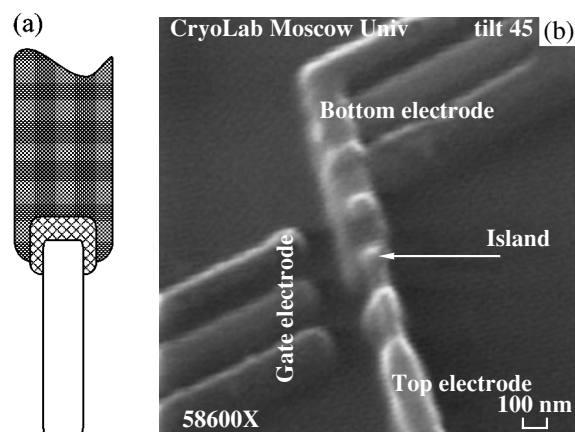
Fig. 1. Asymmetric Al SET transistor manufactured by the three angle shadow evaporation technique. (a) Top view: arrangement of the metallic layers forming the bottom electrode (gray), island (light gray) and top counter-electrode (white); (b) SEM microphotograph of the transistor structure.

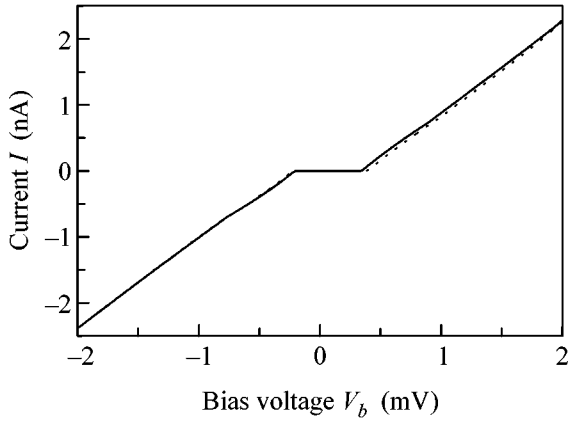¶This article was submitted by the authors in English.

Fig. 2. Experimental *I–V* curve of the studied transistor (solid line) and its theoretical fit with the parameters presented in the text.
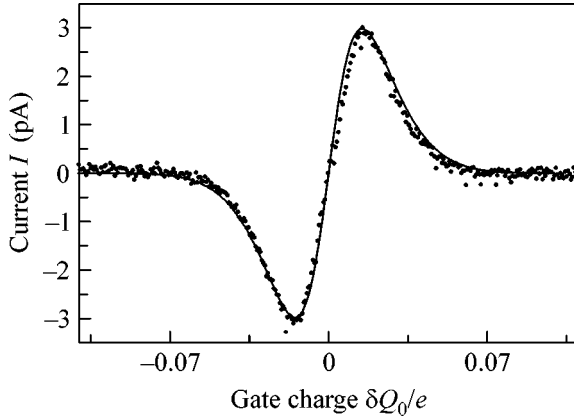

Fig. 3. Experimental (points) response curve of the asymmetric SET transistor at an harmonic voltage bias with the amplitude $V_{ac} = 20\ \mu V$. The fitting curve (solid line) was calculated for the experimentally evaluated parameters of the transistor and a signal amplitude of 23 μV. The effective electron temperature T was assumed to be 40 mK.

1. SAMPLE FABRICATION

The Al structures (Fig. 1) were fabricated on a Si substrate buffered by a sputtered 200 nm thick AlO_x layer. The traditional shadow evaporation technique and *e*-beam lithography were used in the fabrication process. The suspended mask was used to perform three successive depositions of Al at different angles *in situ*: first for the bottom electrode, second for the island, and third for the counter electrode. Two oxidation processes were performed in between to form tunnel barriers (see for details [5]). The design of the structures was nearly the same as that developed earlier for the stacked SET transistors, which demonstrated very low noise of the background charge [5]. In this paper,

the efforts were focused on the study of the operation characteristics of a device with strongly unequal junctions. Since the junctions were formed at different fabrication steps, the effect of shrinking the orifices and slits in the mask after each evaporation step resulted in a reduction in area of the second (top) tunnel junction, as shown in Fig. 1a.

2. RESULTS AND DISCUSSION

All the measurements were carried out in a dilution refrigerator at a temperature of $T_{bath} = 25$ mK. A magnetic field of 1 T was applied to the sample in order to suppress the superconductivity in the Al electrodes of the transistor. The parameters of the transistor were evaluated as follows: $R_1 = 60$ kΩ, $R_2 = 0.6$ MΩ, $C_1 = 0.26$ fF, and $C_2 = 0.03$ fF. Its *I–V* curve is shown in Fig. 2. In this strongly asymmetric sample ($R_1 \ll R_2$ and $C_1 \gg C_2 \gg C_g$, where $G_g = 0.2$ aF is the gate capacitance) at zero voltage bias and around the gate charge $Q_0 = C_g V_g \approx e/2 + en$ (*n* is integer and V_g is the gate voltage), we observed the DC current response as small antisymmetric peaks. These peaks can be explained by the effect of rectification of the unavoidable voltage noise due to the strong asymmetry of the transistor *I–V* characteristic at $V = 0$ (see also [3]). A similar behavior of the transistor was observed when an AC signal, $V = V_{ac}\sin\omega t$, was applied to the transistor. Moreover, the amplitude of the current peaks strongly depended on the degree of asymmetry (R_2/R_1 and C_1/C_2) and on the amplitude V_{ac} of the AC signal. The transistor current response measured in such a regime at $V_{ac} = 20\ \mu V$ and at a frequency of $\omega/2\pi = 500$ Hz is shown in Fig. 3. Some small discrepancy between the experimental and fitted curves in Fig. 3 can be explained by the presence of the nonzero voltage noise applied to the transistor. This means that, in the experimental case, we measured the total action of the applied AC and *noise* signals; the effective noise level V_{noise} can be estimated to be about of 10 μV. Analogous measured and calculated responses in the DC voltage bias regime for the studied transistor at the same value of Q_0 are shown in Fig. 4.

To fit the experimental curve for slow AC signals ($\omega \ll I/e$, where *I* is the SET current), we applied the orthodox theory of SET [6]. Presenting the gate charge Q_0 in the form $Q_0 = e/2 + en + \delta Q_0$, we expressed the appropriate tunneling rates $\Gamma_i^{\pm}$ through the ith junction in the positive (+) and negative (–) directions as

$$\Gamma_i^+ = \frac{k_B T}{e^2 R_i} \frac{\gamma_i}{e^{\gamma_i} - 1}, \quad \Gamma_i^- = e^{\gamma_i}\Gamma_i^+, \quad i = 1 \text{ and } 2,$$

where

$$\gamma_{1,2} = \frac{e}{C_\Sigma k_B T}(\delta Q_0 \mp C_{2,1} V_{ac}\sin\omega t),$$

and $C_\Sigma = C_1 + C_2 + C_g$ are the total capacitance of the island.

The SET current across the transistor in the two-charge-state approximation, which is applicable in our case of not very large signals, is expressed as (see, e.g., [7])

$$I = \frac{\Gamma_2^- \Gamma_1^+ - \Gamma_2^+ \Gamma_1^-}{\Gamma_1^+ + \Gamma_2^+ + \Gamma_1^- + \Gamma_2^-} e.$$

Assuming that $|\gamma_i| \gg 1$, i.e., a sufficiently low temperature T, we simplify the expression for the current, which finally reads

$$I = \frac{k_B T}{e} \frac{\gamma_1 \gamma_2}{\gamma_1 R_2 + \gamma_2 R_1} [\exp(-|\gamma_1|) - \exp(-|\gamma_2|)].$$

The DC component $\langle I(\delta Q_0) \rangle$ of the SET current I is obtained by averaging this equation over the voltage $v = v_{ac} \sin \omega t$ with the weight

$$P(v) = \frac{1}{\pi \sqrt{v_{ac}^2 - v^2}}.$$

Notice that the weight function $P(v)$, which can be considered as a probability density to find a value of the voltage within the interval $(v, v + dv)$, equals the ratio of the time-interval $dt = 2dv/v_0 \omega \cos \omega t$, when this event happens, to the period $2\pi/\omega$. The resulting dependence is shown by the solid line in Fig. 3. One can see good agreement between the experimental data and the theoretical fit.

The observed features of an asymmetric SET transistor demonstrates that it can be used as a noise level sensor for the bias and signal lines of a measuring setup. For example, the sensitivity of the studied transistor to the noise signal in the bias lines was roughly estimated as 20 nV/Hz$^{1/2}$ in the frequency range from $\Delta f = 0.1$–10 kHz. The amplitude of the observed current peaks in our setup was about 0.1 pA, i.e., limited by the resolution of the current preamplifier.

Moreover, the asymmetric SET transistor can also be used as a radio frequency driven electrometer operating in a linear regime. The maximum current-to-charge ratio of the device, $\eta = |d\delta I(Q_0 = 0)/d\delta Q_0|$, for a given sample and $V_{ac} = 20$ μV (see Fig. 3) is about 0.3 nA/e. This value is of the same order as that of typical SET electrometers. For example, in the traditional regime of the same amplitude of the DC bias ($V_{dc} = 20$ μV), this electrometer has a slightly better value of η, i.e., 0.7 nA/e at $I = 8$ pA (see Fig. 4). The current-to-charge ratio η can also be found from the analytical expression for $\langle I(\delta Q_0) \rangle$ as the corresponding derivative of $\langle (\partial I(\delta Q_0)/\partial \delta Q_0)_{\delta Q_0 = 0} \rangle$. The analytical expression for this average is rather cumbersome but easy for numerical calculations. In this way, we found the current-to-charge ratio numerically as a function of T and the dimensionless parameter of asymmetry C_2/C_Σ. Fig-
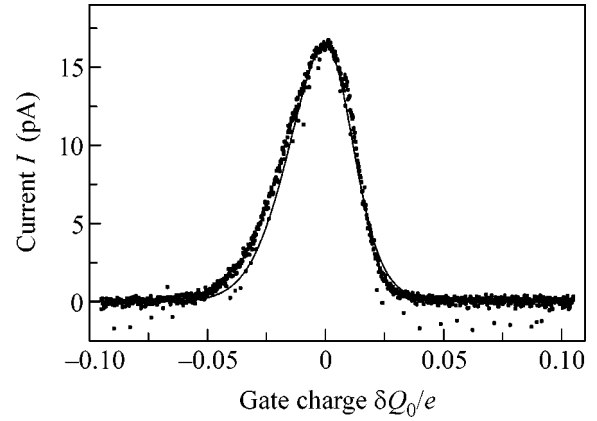
Fig. 4. Experimental (points) and calculated (solid line) modulation curves of the asymmetric SET transistor in the DC bias regime at $V_{dc} = 20$ μV.
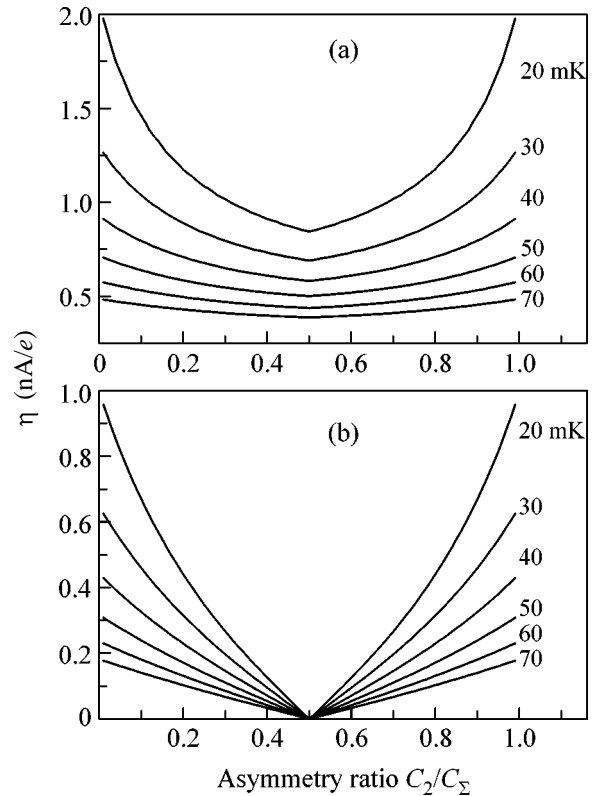
Fig. 5. Current-to-charge transfer coefficient η in the SET transistor versus the asymmetry ratio at different temperatures. $V_{ac} = V_{dc} = 20$ μV. (a) DC regime; (b) AC regime.

ure 5 shows the dependence of η on the value of C_2/C_Σ calculated for several values of the transistor temperature in AC and DC regimes. The lower current-to-charge ratio in the AC regime can be understood from the fact that the effective action of the AC signal on η is

more than two times weaker than the action of the DC signal of the same amplitude.

In some experimental situations (for example, with an RF-SET sensor), the zero bias regime with AC or *noise* pumping can be considered as more convenient for a SET transistor operating as an electrometer. Such a regime of the electrometer operation presumably has weak back action on the background charges located in the dielectric around the island [8]; therefore, the device is less subject to the drift of the offset charge bias.

3. SUMMARY

In this paper, we explored a rather delicate regime ($V \ll e/C_\Sigma$) of the transistor operation, which is important for unperturbed measurements. The results obtained demonstrate the remarkable nonlinear characteristics of the strongly asymmetric SET transistor, which can operate either as a linear electrometer or as a sensitive nonlinear noise detector useful for characterization of an experimental setup. Further investigations of such SET transistors in different regimes and especially their noise characteristics are clearly needed. The available technology makes it possible to fabricate these transistors with a very high degree of asymmetry.

REFERENCES

1. K. K. Likharev, IEEE Trans. Magn. **23**, 1142 (1987).
2. T. A. Fulton and G. D. Dolan, Phys. Rev. Lett. **59**, 109 (1987).
3. J. Weis, R. J. Haug, K. von Klitzing, and K. Ploog, Semicond. Sci. Technol. **10**, 877 (1995).
4. C. Walliser, Dissertation (Forschungszentrum Karlsruhe GmbH, Karlsruhe, 2002).
5. V. A. Krupenin, D. E. Presnov, A. B. Zorin, and J. Niemeyer, J. Low Temp. Phys. **118**, 287 (2000).
6. D. V. Averin and K. K. Likharev, in *Mesoscopic Phenomena in Solids*, Ed. by B. L. Altshuler, P. A. Lee, and R. Webb (Elsevier, Amsterdam, 1991), p. 175.
7. G. L. Ingold and Yu. V. Nazarov, in *Single Charge Tunneling*, Ed. by H. Grabert and M. H. Devoret (Plenum, New York, 1992), Chap. 2.
8. A. B. Zorin, F.-J. Ahlers, J. Niemeyer, *et al.*, Phys. Rev. B **53**, 13682 (1996).

Knight Shift in Superconducting Oxides
BaPb$_{1-x}$Bi$_x$O$_3$ ($x < 0.35$)

V. V. Ogloblichev[1], A. V. Pogudin[1], Yu. V. Piskunov[1], S. V. Verkhovskiĭ[1],
A. Yu. Yakubovsky[2], and A. Trokiner[3]

[1] *Institute of Metal Physics, Ural Division, Russian Academy of Sciences, ul. S. Kovalevskoĭ 18, Yekaterinburg, 620219 Russia*
e-mail: pogudin@imp.uran.ru
[2] *Russian Research Centre Kurchatov Institute, pl. Akademika Kurchatova 1, Moscow, 123182 Russia*
[3] *Laboratorie de Physique du Solide, E.S.P.C.I., 75231 Paris, France*
Received June 6, 2005

The Knight shift $^{207}K_s$ for the ^{207}Pb nuclei in the metal phase of the oxides BaPb$_{1-x}$Bi$_x$O$_3$ ($x < 0.35$) has been analyzed as a function of the concentration. The shift, which is proportional to the density of states near the Fermi energy: $^{207}K_s \sim N(E_F)$, reaches a maximum for an oxide with the maximum superconducting transition temperature T_c ($x \approx 0.25$) = 12 K. A significant increase in the width of the shift distribution with the Bi concentration testifies to the formation of a nonuniform state of the electronic system in the conduction band of superconducting oxides, which is accompanied by an increase in short-wavelength contributions to the spin susceptibility. To detect the ^{207}Pb NMR spectra in superconducting oxides with $x > 0.2$, the ^{17}O–^{207}Pb spin-echo double-resonance method is used, which provides successful detection of the ^{207}Pb NMR signal with an anomalously high rate of spin–spin relaxation $T_2^{-1} > 500$ ms^{-1}. Thus, fundamental restrictions arising in investigations of rapidly relaxing ^{207}Pb nuclei, which are "unobservable" in superconducting oxides BaPb$_{1-x}$Bi$_x$O$_3$ when they are studied by traditional single-resonance methods of pulse NMR spectroscopy, have been overcome. © 2005 Pleiades Publishing, Inc.

PACS numbers: 74.70.–b, 76.60.–k

After the discovery of superconductivity in the BaPb$_{1-x}$Bi$_x$O$_3$ system (BPBO) [1], numerous investigations were devoted to the features of electronic states in the conduction band of the oxide that are responsible for the anomalously high superconducting transition temperature $T_{c, max}(x \approx 0.25)$ = 12 K. The superconducting content range is near the metal–semiconductor concentration transition ($x_{cr} \approx 0.35$) occurring with an increase in the bismuth atom concentration. Estimates of the critical temperature T_c with the use of electron specific heat data on the density of states near the Fermi energy $N(E_F)$ and the Debye approximation for the phonon spectrum are much lower than the experimentally observed value [2–4].

According to x-ray and photoelectron spectroscopy data [5–7], the electron spectrum of oxides with $x \geq 0.2$ contains a pseudogap singularity near E_F whose development in semiconducting oxides completes with the formation of the real gap on wavenumbers $q \sim \pi/a$, where a is the parameter of the pseudocubic unit cell of perovskite. The comparatively low density of current carriers ($n \sim 10^{21}$ cm^{-3}) and charge fluctuations associated with the multiplicity of the valence state of bismuth ions (Bi$^{4+\delta}$/Bi$^{4-\delta}$) can promote the development of the instability of the electron system state that is uni-

form over the crystal in metal-phase oxides [8]. In view of this circumstance, many researchers point to an important role of short wavelength charge fluctuations of the antiferroelectric type for the enhancement of the electron–phonon interaction in the metal phase of the oxide.

According to measurements of the low-temperature specific heat $c_p(T)$ [2], magnetic susceptibility χ [9, 10], and the shifts of the ^{207}Pb [11–13] and ^{17}O [11, 14] NMR lines, $N(E_F)$ increases monotonically with transition to superconducting contents near $T_{c, max}$. The reliability of estimates of $N(E_F)$ is much lower in the pretransition bismuth-concentration range $0.2 < x < 0.35$, which is most actively discussed. With approaching the metal–superconductor transition, the temperature interval where $c_p(T)$ increases linearly narrows sharply, and the extraction of spin contributions to χ and ^{17}K requires additional, insufficiently justified assumptions on the concentration dependence of the corresponding nonspin contributions to the static magnetic susceptibility and shift of the ^{17}O NMR line. In this respect, estimates of $N(E_F)$ using the measured shift of the ^{207}Pb NMR line seem to be most reliable.

As was decisively shown in [11–13], the dominant contribution to the shift of the ^{207}Pb NMR line is the
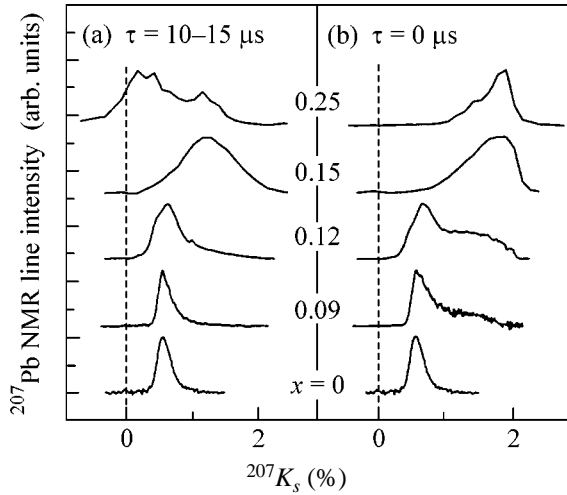
Fig. 1. ^{207}Pb NMR spectra in the BaPb$_{1-x}$Bi$_x$O$_3$ oxide in a magnetic field of 9 T for temperatures of 5–20 K: (a) as measured by the spin echo technique with various time intervals τ between pulses and (b) as reconstructed to the instant $\tau = 0$ according to the known law of irreversible echo decay.

Knight shift associated with the contact Fermi interaction of the lead nuclei with 6s electrons involved in the formation of the conduction band of BPBO oxides:

$$^{207}K_s = 1/\mu_B H_{FC}\chi_s = 2\mu_B H_{FC}N(E_F), \qquad (1)$$

where $H_{FC} = 4200$ kE/μ_B is the hyperfine field created on the nucleus by an unpaired electron of the conduction band and $N(E_F) = \chi_s/2\mu_B^2$ is the density of electronic states on the Fermi level.

Measurements of ^{207}Pb NMR spectra with the subsequent analysis of the $^{207}g(\nu)$ line shape make it possible to determine the concentration dependence of the uniform contribution to the spin susceptibility of oxides $\chi_s(q = 0)$:

$$\chi_s(q = 0) = \mu_B\langle^{207}K_s\rangle/H_{FC}$$
$$= \mu_B/H_{FC}\{1/\nu_0\int(\nu - \nu_0)^{207}g(\nu)d\nu\}. \qquad (2)$$

The average Knight shift $\langle^{207}K_s\rangle$ is determined as the first moment of the resonance line $^{207}g(\nu)$. Analyzing details of the fine structure of the ^{207}Pb NMR spectrum, one can reveal the substantial singularities of the spatial dispersion of $\chi_s(q)$ that are associated with the nonuniform distribution of the electron density over the crystal in the metal phase of BPBO oxides [11].

Data on the concentration dependence $\langle^{207}K_s\rangle$ that were presented in [11] for BaPb$_{1-x}$Bi$_x$O$_3$ oxides were obtained for a wide range of metal phase contents $0 \leq x \leq 0.25$. The ^{207}Pb NMR spectra (Fig. 1a) were measured using the spin echo technique traditionally used when detecting inhomogeneously broadened lines. In

this method, the spin echo signal $M(2\tau; \nu)$ is detected after its excitation at the spectrometer working frequency ν by a pair of high-power rf pulses following the time interval τ: $(\pi/2) - \tau - (\pi) - \tau - M(2\tau; \nu)$. The spectral intensity $^{207}J(\nu)$ shown in Fig. 1b was determined using the amplitude of the echo signal $M(2\tau; \nu)$ that was extrapolated to the instant $\tau = 0$ according to the known law of irreversible echo decay. The main restriction of the spin echo technique in application to the detection of ^{207}Pb NMR spectra is associated with the existence of the minimum possible time interval between pulses $\tau_{min} \sim 10\ \mu$s, which is determined by the process of the recovery of the linear regime in the enhancement of the receiving circuit of the spectrometer after exciting an rf pulse. The existence of τ_{min} significantly reduces the reliability of the reconstructed spectral intensity $^{207}J(\nu)$ that is attributed to contributions from lead nuclei with the characteristic spin–spin relaxation times $T_2(\nu) < \tau_{min}$. This situation arises when the spin-echo single-resonance technique is applied to detect ^{207}Pb NMR spectra in superconducting oxides BaPb$_{1-x}$Bi$_x$O$_3$ ($x > 0.2$), where the rate of the irreversible damping of the ^{207}Pb echo signal increases significantly with approaching the superconducting metal–semiconductor concentration transition: $^{207}T_2^{-1} > 500$ ms^{-1}.

In this paper, we report on ^{207}Pb NMR spectra measured for BaPb$_{1-x}$Bi$_x$O$_3$ oxides over the entire range of the existence of the metal phase, $x < x_{cr}$, with the use of the ^{17}O–^{207}Pb spin-echo double-resonance technique (SEDOR technique [15]). The experiments were carried out in a magnetic field of 9 T at a temperature of 20 K with ^{17}O-enriched polycrystalline samples of the oxide. The features of the synthesis and structural certification, as well as detailed analysis of the ^{17}O NMR spectra, of the BPBO samples under investigation were given in [12].

One of the applications of the spin-echo double-resonance technique is the observation of the heteronuclear coupling between "magnetically nonequivalent" nuclei, whose NMR spectra do not overlap with each other. In a magnetic field of about 9 T, the ^{17}O NMR spectrum lies in a frequency range of 51–57 MHz, whereas the ^{207}Pb NMR spectrum lies in a frequency range of 81–85 MHz. The basic idea of SEDOR experiments is the modulation of the static part of the heteronuclear interaction H_{IS} of the oxygen ion ^{17}O ($I = 5/2$) with the N surrounding lead ions ^{207}Pb ($S = 1/2$) [16]:

$$H_{IS} = \Sigma_n^{17-207}a_nI_zS_{nz}. \qquad (3)$$

Figure 2 shows the sequence of the SEDOR experiment, which was conducted in two stages. At the first stage, the sequence of radio pulses $(\pi/2)_I - \tau - (\pi)_I$ excites an echo signal at the frequency ν_I of the central transition ($m_I = -1/2 \longleftrightarrow +1/2$) of the nuclear spin sys-

tem I and the spin-echo amplitude $M_0(2\tau)$ is measured at time 2τ. If Hamiltonian (3) has no explicit time dependence in an interval of $(0, 2\tau)$, the action of the π_I pulse leads to $H_{IS}(\tau - 0) = -H_{IS}(\tau + 0)$. In this case, the defocusing of the nuclear magnetization of spins I in static local fields $\Sigma_n^{17-207} a_n I_z S_{nz}$ of spins S in an interval of $(0, \tau)$ is accompanied by the subsequent refocusing of the nuclear magnetization of spins I in the interval $(\tau, 2\tau)$ preceding the formation of the echo signal. At the second stage, simultaneously with the π_I pulse, an additional π_S pulse (with duration t_S) is applied at the resonance frequency ν_S of ^{207}Pb nuclei. The latter pulse inverts the direction of the local fields from spins S and conserves the sign of Hamiltonian (3) during the evolution time 2τ: $H_{IS}(\tau - 0) = H_{IS}(\tau + 0)$. As a result, the spin-echo amplitude $M(2\tau)$ at the time 2τ necessarily decreases as compared to $M_0(2\tau)$ due to additional damping associated with the heteronuclear contribution H_{IS}. The relative difference $M(\nu_S) = \{M_0(2\tau) - M(2\tau)\}/M_0(2\tau)$ is proportional to the number of ^{207}Pb nuclei that are excited in the frequency band $\nu_S \pm (1/4t_S)$ by the pulse π_S and introduce damping to the echo amplitude of ^{17}O nuclei. Measuring the difference $M(\nu_S)$ in a series of SEDOR experiments with different frequencies of the π_S pulse, we thereby obtain the ^{207}Pb NMR spectrum whose spectral intensity is $^{207}J(\nu_S) \sim M(\nu_S)$.

We emphasize that the spin–lattice relaxation time T_1 of ^{207}Pb nuclei during which the local field $\Sigma_n^{17-207} a_n I_z S_{nz}$ can be considered as time independent plays an important role in SEDOR experiments. In BPBO oxides of the metal phase, the spin–lattice relaxation time of lead nuclei follows the Korringa law $^{207}T_1 \sim T^{-1}$ [11] and $^{207}T_1 > 1$ ms for temperatures below 100 K. This behavior significantly extends the possibilities of detecting NMR signals of nuclei with anomalously short spin–spin relaxation times.

In the initial oxide BaPbO$_3$, a single symmetric line close to a Gaussian is observed. The line peak position is independent of the temperature and corresponds to the Knight shift $^{207}K_s = 0.55(5)\%$.

Figure 3 shows ^{207}Pb NMR spectra measured in BaPb$_{1-x}$Bi$_x$O$_3$ oxides using the ^{17}O–^{207}Pb SEDOR technique ($x = 0.09, 0.21, 0.27, 0.33$) and ^{207}Pb spin echo technique ($x = 0.00, 0.09, 0.12$). For the BaPb$_{0.91}$Bi$_{0.09}$O$_3$ oxide, the spectral intensity $^{207}J(\nu)$ measured using two methods is shown. The solid line is the spectrum obtained using the traditional spin-echo single-resonance technique ($\tau = 10$ μs) with the subsequent reconstruction of the signal amplitude at the instant $\tau = 0$ [17]. The points are the $^{207}J(\nu_S)$ measured using the ^{17}O–^{207}Pb SEDOR technique. The reconstructed spectrum coincides with the SEDOR spectrum. Satisfactory agreement between spectra corrobo-
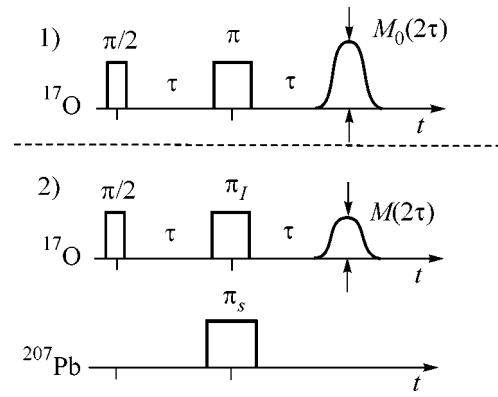

Fig. 2. Sequence of radio pulses for experiments on ^{17}O–^{207}Pb spin echo double resonance (SEDOR).
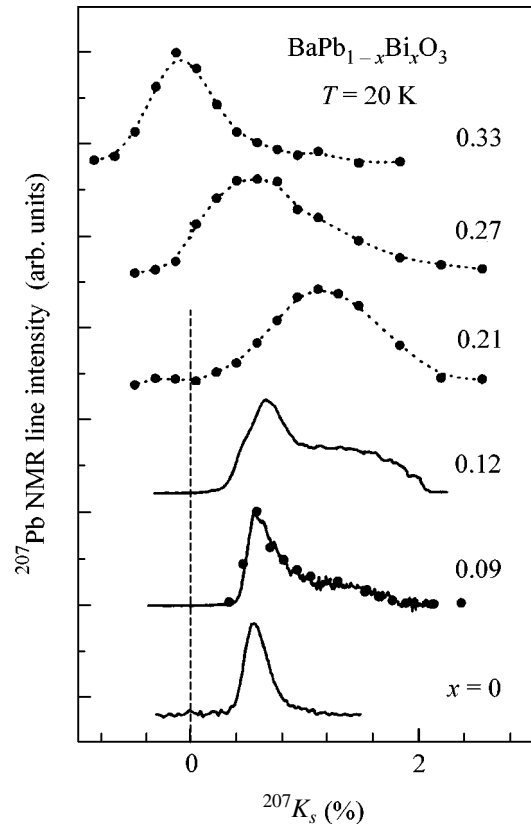

Fig. 3. ^{207}Pb NMR spectra in the BaPb$_{1-x}$Bi$_x$O$_3$ oxide (solid lines) as obtained using the spin-echo single-resonance technique with subsequent reconstruction to the instant $\tau = 0$ and (points) as measured for $^{207}J(\nu_S)$ using the ^{17}O–^{207}Pb SEDOR.

rates that the procedure previously used in [11] to reconstruct the ^{207}Pb spectrum is applicable for $x < 0.2$. Moreover, this agreement demonstrates the evident advantages of the ^{17}O–^{207}Pb SEDOR technique, which
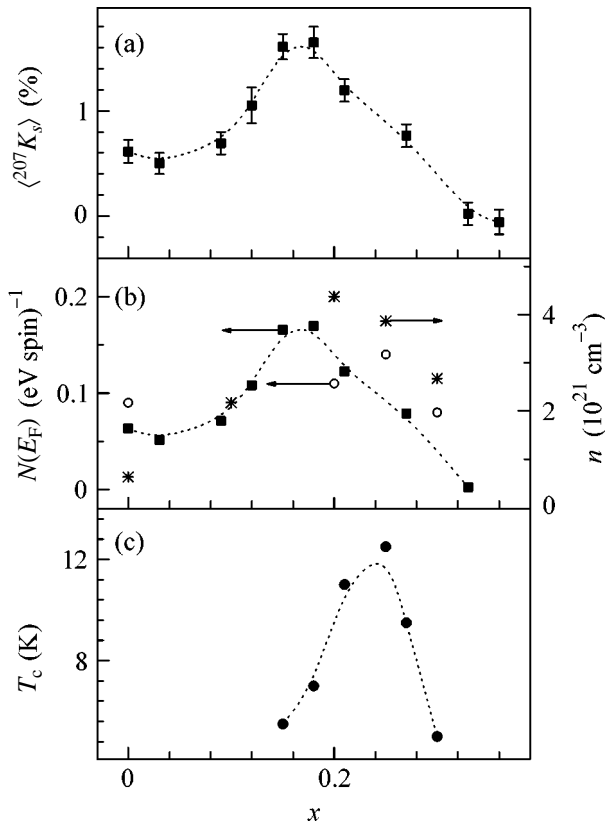
Fig. 4. Concentration dependences in $BaPb_{1-x}Bi_xO_3$ oxides for (a) the average ^{207}Pb Knight shift $\langle ^{207}K_s \rangle$; (b) the density of states at the Fermi level $\langle N(E_F) \rangle$ according to (■) ^{207}Pb NMR, (○) the electron contribution to the specific heat [2], and (∗) the charge carrier density [21]; and (c) the superconducting-transition temperature T_c.

ensures certain detection of contributions to the spectral intensity both from "observable" ^{207}Pb nuclei and from ^{207}Pb nuclei with an anomalously short time T_2.

According to the detailed analysis of the magnetic broadening of the NMR lines as a function of the concentration x, the fine structure of the spectra in Bi-containing oxides with $x < 0.15$ testifies to an anomalous increase in the spin susceptibility χ_s ($^{207}K_s > 1\%$) in domains that contain Bi atoms and have characteristic sizes on the order of the double parameter of the pseudocubic unit cell of perovskite [11]. Overlapping of such microdomains is expected for $x > 0.12$, which indicates that the ordinary metal–superconductor concentration transition is likely of percolation type in $BaPb_{1-x}Bi_xO_3$ oxides. The experiments on the relaxation of the spin echo of ^{207}Pb nuclei [16] provided direct evidence of the microscopic character of the inhomogeneous state of the electron system in bismuth-containing oxides where the attributes of macroscopic phase separation are absent according to x-ray diffraction data [18].

For the content near the maximum T_c (Fig. 4c), the spectrum is formed near the maximum Knight shift. The concentration dependence of the average Knight shift $\langle ^{207}K_s \rangle$ and the corresponding density of one-electron states $N(E_F) = \chi_s/2\mu_B^2$ are shown in Figs. 4a (by squares) and 4b, respectively. We emphasize that, for such low $N(E_F)$ values and 3D motion of conduction electrons in oxides, corrections associated with the exchange enhancement of the spin susceptibility $\chi_s = 2\mu_B^2 N(E_F)/(1 - JN(E_F))$ are immaterial. Using the procedure that was proposed in [19] for estimating the exchange integral J, one can show that the Stoner factor $JN(E_F)$ for the oxide with $x = 0.21$ does not exceed 0.12. In view of this circumstance, it is not surprising that the position of the peak in the density of states at $x = 0.21$ coincides with the maximum in the concentration dependence of the charge carrier density (shown by asterisks) obtained from measurements of the Hall effect in a series of superconducting oxides $BaPb_{1-x}Bi_xO_3$ [20]. Figure 4b shows (∗) estimates obtained for $\langle N(E_F) \rangle$ from measurements of the electron contribution to specific heat [2]. Similar to the dependence of (○), these data present the bismuth-concentration dependence of the crystal-averaged density of electronic states at the Fermi level $N(E_F)$. According to NMR estimates, the density of states reaches the maximum $N(E_F) \approx 0.16$ (eV spin)$^{-1}$ in oxides with $x \approx 0.21$, which is close to the value $x = 0.25$ corresponding to the maximum T_c. With a further increase in the Bi concentration, the Knight shift $\langle ^{207}K_s \rangle \sim \langle N(E_F) \rangle$ decreases sharply and becomes negligibly small, which indicates that the energy gap appears in the low temperature region for the boundary composition $x = 0.33 \approx x_{cr}$ of the metal phase.

It is interesting that the domain with $K_s \approx 0$ arises even in the ^{207}Pb NMR spectrum of the superconducting oxide with $x = 0.27$ ($T_c = 7$ K). This behavior can testify to the local formation of microdomains with extremely low density of mobile charge carriers. To justify this assumption, additional NMR experiments are evidently necessary in order to reveal the short-wavelength singularities of the spatial dispersion of the spin susceptibility near ^{207}Pb nuclei that contribute to the intensity of the low-frequency part of the spectrum in oxides near $x \sim x_{cr}$. It is worth noting that such a possibility of a pseudogap arising near the Fermi energy in superconducting oxides $BaPb_{1-x}Bi_xO_3$ with $x \geq 0.2$ is considered when discussing anomalies in photoemission spectra in these oxides [5–7].

In summary, the concentration dependence has been analyzed for the Knight shift $^{207}K_s$ in ^{207}Pb nuclei in the metal phase of $BaPb_{1-x}Bi_xO_3$ oxides with $x < 0.35$. The shift proportional to the density of states near the Fermi energy, $^{207}K_s \sim N(E_F)$, reaches a maximum near a content with the maximum superconducting transition tem-

perature $T_c(x \approx 0.25) = 12$ K. To detect ^{207}Pb NMR spectra, we used the ^{17}O–^{207}Pb spin-echo double-resonance technique, which has evident advantages when detecting NMR signals from nuclei that cannot be detected by traditional single-resonance methods due to an anomalously high rate of the spin–spin relaxation.

REFERENCES

1. A. W. Sleight, Solid State Commun. **17**, 27 (1975).
2. B. Batlogg, Physica B (Amsterdam) **126**, 275 (1984).
3. S. Ushida, Phase Transit. **8**, 95 (1987).
4. T. Itoh, J. Phys. Soc. Jpn. **53**, 2668 (1984).
5. H. Namatame, A. Fujimori, H. Takagi, *et al.*, Phys. Rev. B **48**, 16917 (1993).
6. H. Sakamoto, J. Phys. Soc. Jpn. **56**, 365 (1987).
7. S. Tajima, S. Uchida, A. Masaki, *et al.*, Phys. Rev. B **35**, 696 (1987).
8. K. Machida, Physica C (Amsterdam) **156**, 276 (1988).
9. T. M. Rice and L. Sneddon, Phys. Rev. Lett. **47**, 689 (1981).
10. S. Uchida *et al.*, Physica C (Amsterdam) **156**, 157 (1988).
11. Yu. Piskunov, A. Gerashenko, A. Pogudin, *et al.*, Phys. Rev. B **65**, 134518 (2002).
12. T. Tsuda, J. Phys. Soc. Jpn. **56**, 3032 (1988).
13. F. J. M. Benschop *et al.*, Physica C (Amsterdam) **235–240**, 2527 (1994).
14. E. Oldfield *et al.*, Phys. Rev. B **41**, 1289 (1990).
15. C. P. Slichter, *Principles of Magnetic Resonance*, 3rd ed. (Springer, New York, 1996).
16. A. V. Pogudin, V. V. Ogloblichev, Yu. V. Piskunov, *et al.*, Pis'ma Zh. Éksp. Teor. Fiz. **80**, 124 (2004) [JETP Lett. **80**, 114 (2004)].
17. In oxides with $x < 0.2$ for the lead nuclei with $^{207}S = 1/2$, the basic contribution to the rate T_2^{-1} of the irreversible damping of the echo signal comes from the indirect interaction $^{207}J_{ij}S_{zi}S_{zj}$ via the conduction electron system of the oxide with the constant $^{207}J_{ij} \sim {}^{207}K$. Except the oscillating character of the initial damping section, the amplitude of the echo signal decreases according to the exponential dependence $M(2\tau; \nu) \sim \exp(-2\tau/T_2(\nu))$, where the characteristic time of the transverse relaxation of the nuclear magnetization is $T_2(\nu) \sim ({}^{207}K)^{-1}$.
18. K. Kumagai, Yu. Piskunov, A. Yakubovskii, *et al.*, Physica C (Amsterdam) **274**, 209 (1997).
19. A. M. Clogston, Phys. Rev. **136**, A8 (1964).
20. T. D. Thanh, A. Koma, and S. Tanaka, Appl. Phys. A **22**, 205 (1980).

Translated by R. Tyapaev

Electron–Phonon Interaction in Boron-Doped Silicon Nanocrystals: Effect of Fano Interference on the Raman Spectrum

V. A. Volodin and M. D. Efremov

Institute of Semiconductor Physics, Siberian Division, Russian Academy of Sciences, Novosibirsk, 630090 Russia
e-mail: volodin@isp.nsc.ru

Raman spectroscopy is employed for studying silicon nanocrystal arrays in boron-doped amorphous silicon films. The nanocrystals were formed in the initial amorphous films by the pulsed impact of an excimer laser. The electron–phonon interaction effects are observed experimentally in the heterostructure formed by a silicon nanocrystal and an amorphous matrix. These effects can be described in the framework of the familiar Fano interference model. © 2005 Pleiades Publishing, Inc.

PACS numbers: 61.46.+w, 63.20.Kr, 63.22.+m, 78.30.–j

Since the discovery of effective photoluminescence in porous silicon [1] and silicon nanocrystals in insulator films [2], research aimed at obtaining a silicon nanostructure with new electronic and optical properties has rapidly developed. Doping with a shallow impurity is known to affect the optical and electrophysical properties of nanocrystals embedded in a silicon dioxide matrix [3]. The possibility of controlled doping will considerably extend the range of experiments with nanocrystals. It is well known that, for a hole concentration in silicon single crystals equal to or exceeding 5×10^{18} cm^{-3}, the interaction between optical phonons and the continuum of electron transitions between the light hole band and the heavy hole band becomes appreciable (in a broader sense, this effect is known as Fano interference [4]). This effect leads to a decrease in the frequency as well as to broadening and asymmetry of the peak of Raman scattering from optical phonons [5, 6]. However, we are aware of only two publications in which the authors studied the effect of doping with a shallow impurity on the Raman spectra of silicon nanocrystals [7, 8]. In those works, the authors investigated boron-doped silicon nanocrystals in SiO$_2$, where the shift of the Raman peak was only 1–2 cm^{-1} for various doping levels, although the effect of doping in the absorption spectra in the IR region was noticeable (according to the authors of those publications, due to the absorption of photons at free charge carriers). In this connection, it is important to analyze the effect of the electron–phonon interaction on the Raman spectra of silicon nanocrystals for various doping levels and sizes of nanocrystals.

Our samples were prepared as follows. Amorphous silicon films 100 nm in thickness were grown using plasmachemical deposition on glass substrates at a temperature of 250°C. The film thickness was monitored using ellipsometric data. Initially undoped films were subjected to boron ion implantation with doses of 3×10^{14} and 3×10^{15} cm^{-2}. The ion energy was 10 keV, the average mean free path of the ions was 50 nm, and the peak of the ion concentration distribution was at the middle of the film. During implantation, a part of each film was covered with a screen and remained undoped (for comparison). Both implanted and nonimplanted regions of the structures were treated by pulsed laser radiation with a wavelength (XeCl laser) of 308 nm and a pulse duration shorter than 25 ns. We used two modes of treatment with different pulse energy densities. The first mode had an energy density lower than the melting threshold of the film and 10 pulses with a frequency of 1 Hz, while the second mode was characterized by an energy density near the melting threshold of the entire film and only one pulse. Since the main effect produced by the laser on the film is thermal, such a treatment can be called laser annealing (in the subsequent analysis, these modes will be referred to as Ann1 and Ann2, respectively). According to the reference data, the threshold energy density for melting amorphous silicon is 120–150 mJ/cm^2 [9]. It should be noted that the approach used here makes it possible to vary the average size of the nanocrystals [10] and to carry out the crystallization of thin films of amorphous silicon on non-refractory (even plastic) substrates [11, 12]. Raman spectra were recorded at room temperature in the quasibackscattering geometry; a 514.5-nm line from an Ar$^+$ laser was used for the excitation.

Figure 1 shows the Raman spectra of samples subjected to the Ann1 treatment. All the spectra display two peaks, viz., a broad peak with a maximum near 480 cm^{-1} and a narrower peak shifted towards higher
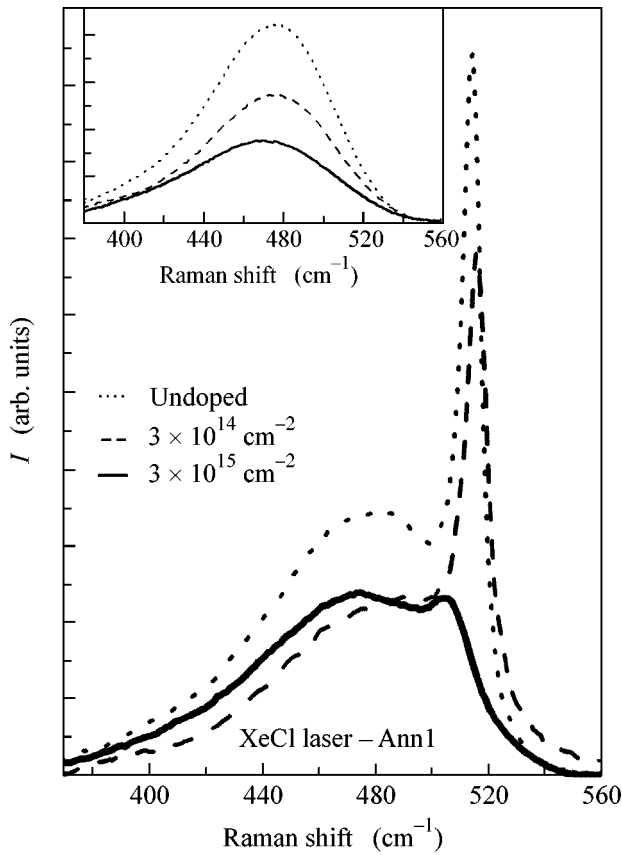
Fig. 1. Raman spectra of a-Si films with silicon nanocrystals formed by laser treatment in the Ann1 mode. The inset shows the Raman spectra of the original films.
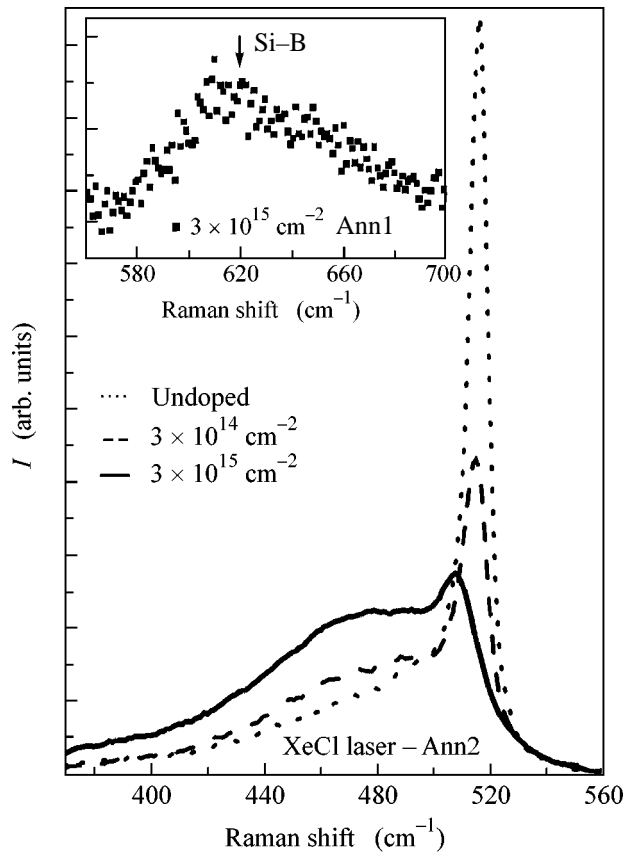

Fig. 2. Raman spectra of a-Si films with silicon nanocrystals formed by laser treatment in the Ann2 mode. The inset shows the Raman spectra in the region of local vibrations of Si–B bonds.

frequencies. Due to the absence of translational symmetry, optical transitions in amorphous silicon are not limited by the quasimomentum conservation law. For this reason, its Raman spectrum is characterized by the effective density of vibrational states and has the shape of a broad peak with a maximum near 480 cm^{-1} [6]. The natural vibrational modes of silicon nanocrystals are spatially localized. For this reason, the Raman spectrum of nanocrystals is characterized by a peak whose position depends on their sizes; as the size increases to more than 50 nm, the position of the peak is almost the same as the position of the Raman peak for monocrystalline silicon (520 cm^{-1}) [13]. For undoped films, the peak width is determined by the size dispersion of nanocrystals, as well as by the uncertainty relation for the energy and wavenumber in view of the finite lifetime of phonons and their spatial localization. The intensity of the "nanocrystal" peak is proportional to the fraction of the nanocrystalline phase. The inset in Fig. 1 shows that the initial films did not contain nanocrystals. Implantation of boron ions reduced the Raman intensity.

Let us now consider the effect of doping of nanocrystals (and, consequently, the electron–phonon interaction) on the Raman spectra. It can be seen that the peak of Raman scattering from silicon nanocrystals is

noticeably displaced in strongly doped films: the position of the peak is 505 cm^{-1} as compared to 515 cm^{-1} for undoped and weakly doped films. Figure 2 shows a similar pattern (for samples subjected to the Ann2 treatment). It is seen that the maximum of the nanocrystal peak for undoped films corresponds to 517 cm^{-1}, which means that the average size of the nanocrystals in the case of the Ann2 treatment is slightly larger than the value in the case of the Ann1 treatment. The inset in Fig. 2 also shows the Raman spectrum for a doped sample in the frequency range corresponding to vibrations of the Si–B bonds (610–615 cm^{-1} for the ^{11}B isotope [14]). It can be seen that laser treatment led to embedding of boron into the silicon lattice and, accordingly, to the electric activation of boron.

For a more detailed analysis, we subtracted the spectrum of amorphous silicon from the Raman spectra of the films doped to the maximum possible level. The results are shown in Fig. 3. The experimental spectra were approximated by the lines of the Fano profile defined by the formula [4, 5]

$$I(\omega) = \left(q + \frac{w - \Omega - \delta\Omega}{\Gamma}\right)^2 \Big/ \left[1 + \left(\frac{w - \Omega - \delta\Omega}{\Gamma}\right)^2\right].$$
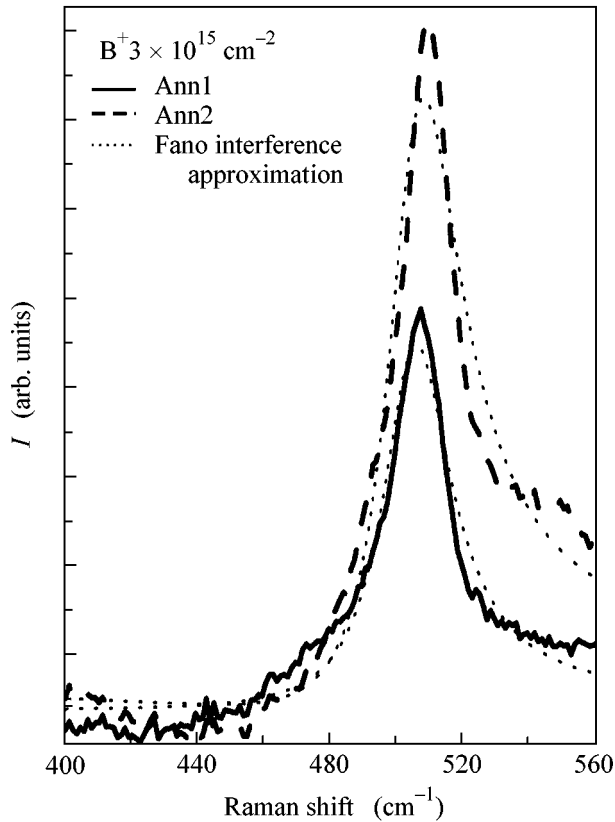
Fig. 3. Comparison of experimental Raman spectra (the contribution from the amorphous matrix is subtracted) with calculated spectra taking into account Fano interference.

Here, Γ is a parameter determining the linewidth and proportional to the squared matrix element of the electron–phonon interaction, q is a parameter describing the line asymmetry, q^2 is equal to the ratio of the intensities of Raman scattering from phonons and electrons divided by Γ, $\delta\Omega$ is the peak shift (due to the strong decay of optical phonons as a result of their interaction with the electron subsystem), and Ω is the frequency of an optical phonon disregarding the electron–phonon interaction [5]. Approximation of experimental spectra by theoretical spectra (dotted curve in Fig. 3) was used to determine the parameters q, Γ, and $\delta\Omega$. Knowing these parameters, we can find the hole concentration [5]. Estimating the hole concentration in silicon nanocrystals using the model applicable for bulk silicon, we obtain values ranging from 5×10^{19} to 2.5×10^{20} cm^{-3}. Obviously, results with higher accuracy can be obtained only by developing a microscopic model taking into account the nanoscale of the objects. Let us consider such a model qualitatively. A silicon nanocrystal in an amorphous matrix presents a potential well for holes [15]. An optical phonon with a certain frequency modulates the parameters of this well, causing a change in the energy of the localized states (the analog of the polaron effect). The effect of interference between Raman scattering from optical phonons localized in nanocrystals and electron Raman scattering at transitions between a localized hole and the continuum of hole states in the amorphous matrix is analogous to interference in monocrystalline silicon, but this analogy is insufficient for quantitative analysis.

Thus, using Raman spectroscopy, we have discovered the effects of the electron–phonon interaction in a heterostructure of a silicon nanocrystal/amorphous matrix. Analysis of the electron–phonon interaction in the framework of Fano interference can be used for estimating the charge carrier concentration in semiconductor nanostructures. The main advantage of the proposed approach is that it is a contactless method. For measurements of the charge carrier concentration with a higher accuracy, a quantitative model of the electron–phonon interaction in nanocrystals is required.

REFERENCES

1. L. T. Canham, Appl. Phys. Lett. **57**, 1046 (1990).
2. T. Shimizu-Iwayama, S. Nakao, and K. Saitoh, Appl. Phys. Lett. **65**, 1814 (1994).
3. G. A. Kachurin, S. G. Yanovskaya, D. I. Tetel'baum, *et al.*, Fiz. Tekh. Poluprovodn. (St. Petersburg) **37**, 738 (2003) [Semiconductors **37**, 713 (2003)].
4. U. Fano, Phys. Rev. **124**, 1866 (1961).
5. F. Cerdeira, T. A. Fjeldly, and M. Cardona, Phys. Rev. B **8**, 4734 (1973).
6. *Light Scattering in Solids*, Ed. by M. Cardona (Springer, Berlin, 1975; Mir, Moscow, 1979), p. 204.
7. Y. Kanzawa, M. Fujii, and S. Hayashi, Solid State Commun. **100**, 227 (1996).
8. Y. Kanzawa, M. Fujii, and S. Hayashi, Mater. Sci. Eng., A **217–218**, 155 (1996).
9. T. Sameshima and S. Usui, J. Appl. Phys. **70**, 1281 (1991).
10. M. D. Efremov, V. V. Bolotov, V. A. Volodin, *et al.*, J. Phys.: Condens. Matter **8**, 273 (1996).
11. M. D. Efremov, V. A. Volodin, L. I. Fedina, *et al.*, Pis'ma Zh. Tekh. Fiz. **29** (13), 89 (2003) [Tech. Phys. Lett. **29**, 569 (2003)].
12. M. D. Efremov, V. A. Volodin, S. A. Arzhannikova, *et al.*, Pis'ma Zh. Tekh. Fiz. **31** (2), 86 (2005) [Tech. Phys. Lett. **31**, 128 (2005)].
13. V. Pailard, P. Puech, M. A. Laguna, *et al.*, J. Appl. Phys. **86**, 1921 (1999).
14. F. Cerdeira, T. A. Fjeldly, and M. Cardona, Phys. Rev. B **9**, 4344 (1974).
15. M. D. Efremov, S. A. Arzhannikova, V. A. Volodin, *et al.*, in *Proceedings of 12th International Symposium on Nanostructures: Physics and Technology* (St. Petersburg, Russia, 2004).

Translated by N. Wadhwa

Amplitude of Aharonov–Bohm Oscillations in a Small Semiconductor Ring Interferometer in the Tunneling Regime

D. V. Nomokonov and A. A. Bykov

Institute of Semiconductor Physics, Siberian Division, Russian Academy of Sciences, Novosibirsk, 630090 Russia
e-mail: bykov@thermo.isp.nsc.ru
Received June 16, 2005

The amplitude g_{AB} of Aharonov–Bohm oscillations in a small semiconductor ring interferometer is studied as a function of the average conductance G_{AV}. Experimentally, it is found that, in the tunneling regime, the relative amplitude g_{AB}/G_{AV} of h/e oscillations is constant in the rings under investigation and smaller than unity. The small value of g_{AB}/G_{AV} in ring interferometers in the tunneling regime at low temperatures is explained by the difference in the amplitudes of the interfering electron waves. © 2005 Pleiades Publishing, Inc.

PACS numbers: 73.23.–b, 73.40.Gk

An important feature that distinguishes the ring interferometers fabricated on the basis of 2D electron gas in modulated semiconductor structures [1] from similar metal-based devices [2] consists in that the dimensions of the conducting regions of a semiconductor interferometer are not only preset by lithography but also depend on the size of the lateral depletion regions formed along the boundaries of the conducting channels. In relatively "large" semiconductor rings, whose effective radius satisfies the inequality $r_{eff} = (r_{in} + r_{ext})/2 \gg w_d$, where r_{in} and r_{ext} are the lithographically determined internal and external radii of the ring and w_d is the width of the depletion regions formed along the etching boundaries, the width of the electron channels is approximately the same, w_e, in the branching regions at the input and output of the ring and in the interferometer arms. In "small" rings fabricated on the basis of semiconductor structures with a high density of a 2D electron gas [3], when $r_{eff} \sim w_d$, the lateral dimensions and the energy "depth" of the conducting regions at the input and output of the interferometer and in its arms are noticeably different. As a result, in the tunneling regime, a small ring interferometer falls into two triangular quantum dots connected with each other and with the source (S) and drain (D) regions by tunneling channels [4].

The interest in studying the electron properties of such mesoscopic devices is primarily related to the fact that the tunneling coupling of the two quantum dots may provide the basis for the realization of qubits [5–7]. Earlier, it was shown that the periodic oscillations of conductance as a function of gate voltage that occur in small rings in the tunneling regime are caused by the single-electron charging of the triangular quantum dots formed in the branching regions at the input and output

of the ring [4, 8]. It was also found that, in small rings in the tunneling regime, the Aharonov–Bohm effect also manifests itself. However, the mechanisms that determine the amplitude of the h/e oscillations in these devices in the presence of both Coulomb blockade and coherent processes are still poorly investigated. In this paper, we report on the experimental and theoretical studies of the amplitude of Aharonov–Bohm oscillations, g_{AB}, as a function of the average conductance G_{AV} of a small ring interferometer. We show that, in the tunneling regime, $g_{AB} \propto G_{AV}$.

The interferometers studied in the experiment were fabricated on the basis of a selectively doped GaAs/AlGaAs heterojunction grown by molecular beam epitaxy. A specific feature of the heterostructure was the small spacer thickness of 3 nm. Owing to this spacer thickness, the concentration of the 2D electron gas in the initial heterostructure reached $n_e = 1.45 \times 10^{12}$ cm^{-2} and the electron mobility was $\mu = 3.4 \times 10^4$ cm^2/V s at $T = 4.2$ K. The geometry of the interferometer was determined by electron beam lithography with a subsequent dry etching. The resistance was measured by the two-terminal method with an ac current of frequency 7 to 800 Hz. The magnitude of the current was chosen so that the source–drain voltage did not exceed $k_B T/e$, where e is the electron charge. Figure 1a shows the image of the interferometer that was obtained with a scanning electron microscope. Figure 1b schematically represents the conducting regions of the small ring interferometer in the tunneling regime. One can see that, with allowance for the depletion regions whose width is $w_d = (r_{ext} - r_{in})/2$, the ring is separated by four constrictions into two triangular conducting regions lying at the branch points of the ring. The
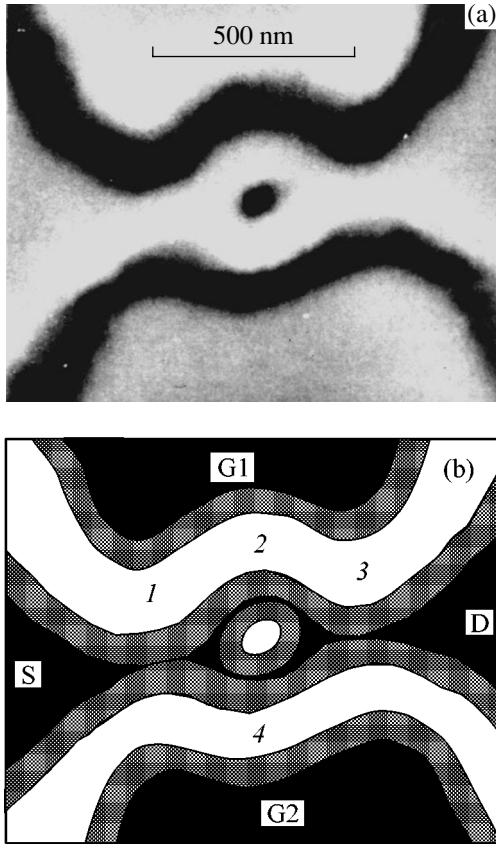
Fig. 1. (a) Ring interferometer image obtained with a scanning electron microscope. The dark areas represent the etching regions. (b) Schematic representation of the ring interferometer in the tunneling regime. The dark areas represent the conducting regions, the grey areas show the depletion regions, and the white areas correspond to the etching regions, G1 and G2 denote the split gate, and S and D are the source and drain regions.

Fig. 2. (a) Experimentally measured conductance of a ring interferometer vs. the gate voltage in zero magnetic field at $T = 1.3$ K. (b) Magnetic field dependences of (solid line) the conductance G_{SD} and (dashed line) the average conductance G_{AV}.

regions occupied by the 2D electron gas are denoted as G1 and G2 and serve as the split gate.

Figure 2a shows the conductance of the ring interferometer, G_{SD}, as a function of the gate voltage V_G, which is simultaneously supplied to G1 and G2. The $G_{SD}(V_G)$ dependence exhibits oscillations with the period $\Delta V_G = 6$ mV; these oscillations are caused by the single-electron charging of the triangular quantum dots of the interferometer [4, 8]. Figure 2b shows the dependence of G_{SD} on the magnetic field B. The period $\Delta B = 73$ mT of the oscillations observed in the $G_{SD}(B)$ dependence corresponds to the condition $\pi r_{\text{eff}}^2 \Delta B = \Phi_0$, where $r_{\text{eff}} = 130$ nm and Φ_0 is the magnetic flux quantum. From Fig. 2b, one can see that the Aharonov–Bohm oscillations are close to sinusoid in shape and their amplitude is much smaller than the average conductance G_{AV}. The manifestation of oscillations in both $G_{SD}(V_G)$ and $G_{SD}(B)$ dependences suggests that, in the small ring under study, the tunneling processes, which lead to the charging of the quantum dots, coexist with

the coherent circular motion, which leads to the Aharonov–Bohm oscillations. Figure 3a shows the dependence of the amplitude of the h/e oscillations, g_{AB}, on G_{AV}. In the experiment, the value of G_{AV} was varied by the gate voltage and the magnetic field. The experimental dependences presented in Fig. 3 show that the amplitude of the Aharonov–Bohm oscillations, g_{AB}, increase with increasing G_{AV}, while its relative value g_{AB}/G_{AV} remains constant, retaining its maximum value of 0.1 up to $G_{AV} \sim e^2/h$.

From the numerical analysis of the processes of single-electron charging of the triangular quantum dots in small ring interferometers, it was found that a high resistance can be achieved in them not only when the ring is separated by four tunneling barriers into two quantum dots but also when these quantum dots are connected with each other and with the reservoirs by single-mode quantum wires [8]. In the most realistic situation of this kind, the quantum dots are connected with each other by single-mode quantum wires and with the source and drain regions by tunneling barriers.

The simplest model of a ring interferometer is a one-dimensional quantum ring [9, 10]. One-dimensional models are widely used, because they are relatively

simple and make it possible to express the main properties of structures in an explicit analytical form by ignoring the details of secondary importance. The cited papers [9, 10] consider the simplest case, which assumes that the coupling coefficients at the input and output of the ring interferometer are identical and that the electron wave is split into two identical parts at the branch points. However, with this model, it is impossible to explain the small value of g_{AB}/G_{AV} that was observed in the ring interferometers under study in the tunneling regime.

To analyze the experimental data, we consider a more general case of a ring interferometer with an asymmetric amplitude division at its input and output (see the inset in Fig. 3a). We assume that the branching at the input is identical with that at the output and is described by the unitary S matrix

$$\hat{S}_B = \begin{pmatrix} -c & \sqrt{\varepsilon} & \sqrt{\eta} \\ \sqrt{\varepsilon} & a & b \\ \sqrt{\eta} & b & \alpha \end{pmatrix}, \qquad (1)$$

where

$$c = \sqrt{1 - \varepsilon - \eta}, \quad a = \frac{\varepsilon c - \eta}{\varepsilon + \eta},$$

$$\alpha = \frac{\eta c - \varepsilon}{\varepsilon + \eta}, \quad b = \sqrt{\varepsilon\eta}\frac{c + 1}{\varepsilon + \eta},$$

and ε and η are the coupling coefficients between the wire and the upper and lower arms of the ring structure, respectively. The splitter described by this S matrix divides the amplitude of the incident electron wave in the $(\varepsilon/\eta)^{-1/2}$ ratio. Following the approach used in [9, 10], we perform simple calculations to obtain the transmission factor for the system under consideration:

$$T_{AB}(\theta, \phi, \delta) = \frac{8\varepsilon\eta\sin(\phi+\delta)\sin(\phi-\delta)\cos 2\theta + 4\varepsilon^2\sin^2(\phi+\delta) + 4\eta^2\sin^2(\phi-\delta)}{[2b^2\cos 2\theta + (a^2+\alpha^2)\cos 2\delta - (2-\varepsilon-\eta)\cos 2\phi]^2 + [(\varepsilon+\eta)\sin 2\phi + (\varepsilon-\eta)\sin 2\delta]^2}, \qquad (2)$$

where $\theta \equiv \pi\Phi/\Phi_0$, Φ is the magnetic flux through the ring area, Φ_0 is the magnetic flux quantum, $\phi \equiv k_F(L_1 + L_2)/2$ is the average phase shift acquired by an electron when it propagates through the ring from input to output, and $\delta \equiv k_F(L_1 - L_2)/2$ is the difference in the phase shifts associated with the propagation through the upper and lower parts of the ring from input to output ($L_1 + L_2 = 2\pi r$, r is the ring radius). Formula (2) is the generalization of the expression obtained by Butticker *et al.* [9] for the conductance of a one-dimensional single-mode ring to the case of an asymmetric division of the electron wave amplitude at the input and output branch points. One can easily verify that, at $\varepsilon = \eta$, Eq. (2) is reduced to the formula given in [9].

In our experiment, we observed a small relative amplitude of h/e oscillations. At low temperatures, when $L_\phi \gg r$, this result can only be explained by the difference in the amplitudes of the interfering waves. In the framework of our model, this means the difference in the values of ε and η. In the case of a strong asymmetry of the amplitude division at the branch points, e.g., when $\varepsilon \ll \eta$, Eq. (2) yields

$$T_{AB}(\theta, \phi, \delta) \qquad (3)$$

$$\approx \frac{2\varepsilon\eta\sin(\phi+\delta)\sin(\phi-\delta)\cos 2\theta + \eta^2\sin^2(\phi-\delta)}{\left[4\frac{\varepsilon}{\eta}\cos 2\theta + \cos 2\delta - \cos 2\phi\right]^2 + \frac{\eta^2}{4}[\sin 2\phi - \sin 2\delta]^2}.$$

When $(\cos 2\delta - \cos 2\phi)^2 \gg \eta^2$, Eq. (3) yields a useful approximate expression for the relative value of the Aharonov–Bohm oscillation amplitude:

$$\frac{g_{AB}}{G_{AV}} \equiv 2\frac{T_{max} - T_{min}}{T_{max} + T_{min}} = 4\frac{\varepsilon}{\eta}\frac{2 - \sin^2(\phi+\delta)}{\sin(\phi+\delta)\sin(\phi-\delta)}. \qquad (4)$$

Expression (4) shows that the relative amplitude of the h/e oscillations is small and proportional to the degree of asymmetry of the amplitude division, i.e., to ε/η. Thus, in the tunneling regime, in the presence of a noticeable asymmetry of propagation through the upper and lower arms, the Aharonov–Bohm oscillations have the form of harmonic oscillations rather than a periodic sequence of sharp resonance peaks, as in the case of identical amplitudes in the arms, $\varepsilon = \eta$ [9, 10]. The relative amplitude of the Aharonov–Bohm oscillations in the asymmetric case is determined by the ratio ε/η. The model of a perfect one-dimensional quantum ring is a fairly strong simplification. A real semiconductor ring has a finite width and an imperfect shape of the boundaries. In addition, the comparison with the experiment requires taking into account the dependences of the parameters ε and η on the magnetic field. Nevertheless, in the framework of the accepted simplification, we obtained a qualitative agreement between the theory and experiment.

Thus, we generalized the expression for the conductance of a one-dimensional single-mode ballistic ring to the case of an asymmetric amplitude division at the input and output of the ring. On the basis of this expression, we analyzed the behavior of the relative amplitude of h/e oscillations and found that this amplitude depends on the degree of asymmetry of the amplitude division. This result qualitatively agrees with the results of the numerical analysis performed for a small ring
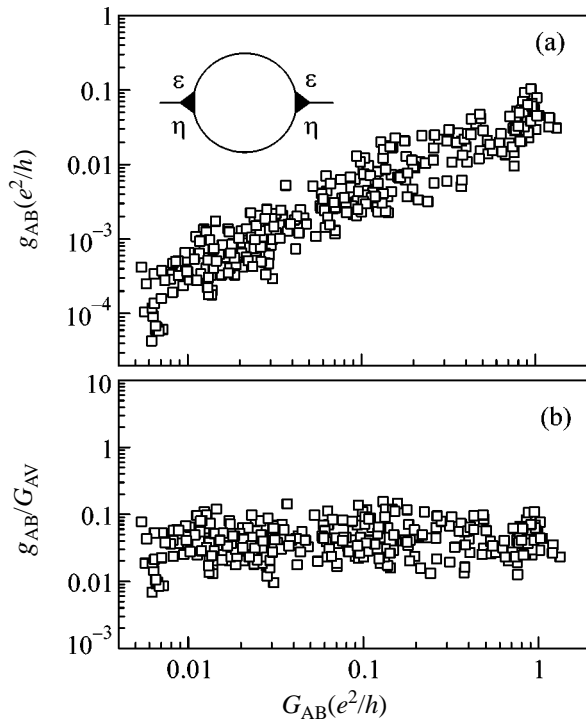
Superconductivity at Normal Pressure in κ-(BEDT-TTF)₂Cu[N(CN)₂]Cl Crystals

E. B. Yagubskii*, N. D. Kushch*, A. V. Kazakova*, L. I. Buravov*, V. N. Zverev**, A. I. Manakov**, S. S. Khasanov**, and R. P. Shibaeva**

* Institute of Problems of Chemical Physics, Russian Academy of Sciences, Chernogolovka, Moscow region, 142432 Russia
** Institute of Solid State Physics, Russian Academy of Sciences, Chernogolovka, Moscow region, 142432 Russia
e-mail: zverev@issp.ac.ru
Received June 16, 2005

Single crystals of the κ-(BEDT-TTF)₂Cu[N(CN)₂]Cl cation-radical salt are obtained. These crystals exhibit metallic properties and pass to a superconducting state with $T_c = 11.5$ K at ambient pressure. © *2005 Pleiades Publishing, Inc.*

PACS numbers: 61.10.Nz, 72.80.Le, 74.70.Kn

Isostructural cation-radical salts of the κ-(BEDT–TTF)₂Cu[N(CN)₂]X family, where BEDT–TTF is the organic π donor bis(ethylenedithio)tetrathiafulvalene, (X = Br, Cl, I, $Br_{1-x}Cl_x$, and $Br_{1-x}I_x$) have been the subject of numerous investigations in recent years [1–14]. These compounds exhibit a wide diversity of electronic properties in spite of the similarity of their crystal structures. These are layered materials constructed of conducting BEDT–TTF cation-radical layers alternating with insulating layers of singly charged {Cu[N(CN)₂]X}⁻ anions (Fig. 1a). The anionic layer consists of polymer zigzag chains stretched along direction **a** and including a planar three-coordinate Cu^{1+} atom with two bridging [(NC)N(CN)]⁻ dicyanamido groups and a terminal halogen atom X. The cation-radical layer is formed from pairs of BEDT–TTF molecules with an average charge of +0.5 per molecule packed in the crystal perpendicularly to each other (Fig. 1b). The overlapping of molecular orbitals of donor molecules in the layers leads to the formation of broad electron energy bands in the crystal. According to the theoretical band-structure calculations [1–3], these materials must be metals. It has been found that the cation-radical salts with X = Br, $Br_{0.5}Cl_{0.5}$, and $Br_{0.7}Cl_{0.3}$ are organic superconductors at ambient pressure with $T_c = 11.6$ K [2, 5], while the salts with X = Cl and $Br_{0.9}I_{0.1}$ [4, 5] undergo a transition to a superconducting state at a pressure of 0.3 kbar with $T_c = 12.8$ and 3.5 K, respectively, and the salt with X = I passes to a superconducting state at a pressure of 1.2 kbar with $T_c \approx 8$ K [6, 7]. At ambient pressure, the cation-radical salt with X = Cl (designate it as κ-Cl) retains its semiconducting properties to a temperature below 100 K. A transition to an insulating state, which is identified as an antiferromagnetic transition, occurs in the region of 40 K, and weak ferromagnetism is detected in these crystals

below 22 K [4, 8, 9]. When the pressure is varied above several hundreds of bars, crystals of the κ-Cl salt demonstrate a rich phase diagram with paramagnetic insulating, antiferromagnetic insulating, metallic, and superconducting phases [8–12]. In addition, it was found by x-ray diffraction that two structural phase transitions occur in these crystals at a high pressure and room temperature: a reversible transition with a reduction of symmetry at a pressure of 8.8 kbar and the second transition at 12 kbar characterized by the disappearance of Bragg reflections and possibly associated with amorphization under pressure [13].

In this work, it is shown that new intriguing properties are added to the whole diversity of the properties of the Cl–cation radical salt: single crystals of this salt (designate it as κ'-Cl) have been obtained, which, as distinct from the κ-Cl Mott dielectric described above, have metallic properties and pass to a superconducting state with $T_c = 11.5$ K at ambient pressure. An x-ray diffraction study of these crystals has been performed, and their transport properties have been investigated.

The measurements of the electrical resistance were performed with a 20-Hz alternating current using a four-contact method with a synchronous detector. The samples were made as thin plates with characteristic sizes of $1 \times 0.3 \times 0.02$ mm whose surface was oriented along the conducting layers (the ac plane). A couple of contacts were made on each of the two opposite surfaces of the sample using a conducting carbon paste. The resistance of the sample was measured by passing a current both along (J ∥ (ac)) and across (J ∥ b) of the conducting layers. The magnitude of the current J passing through the sample was fixed and did not exceed 10 μA. For experiments in a magnetic field, a superconducting solenoid creating a field of up to 17 T was used.
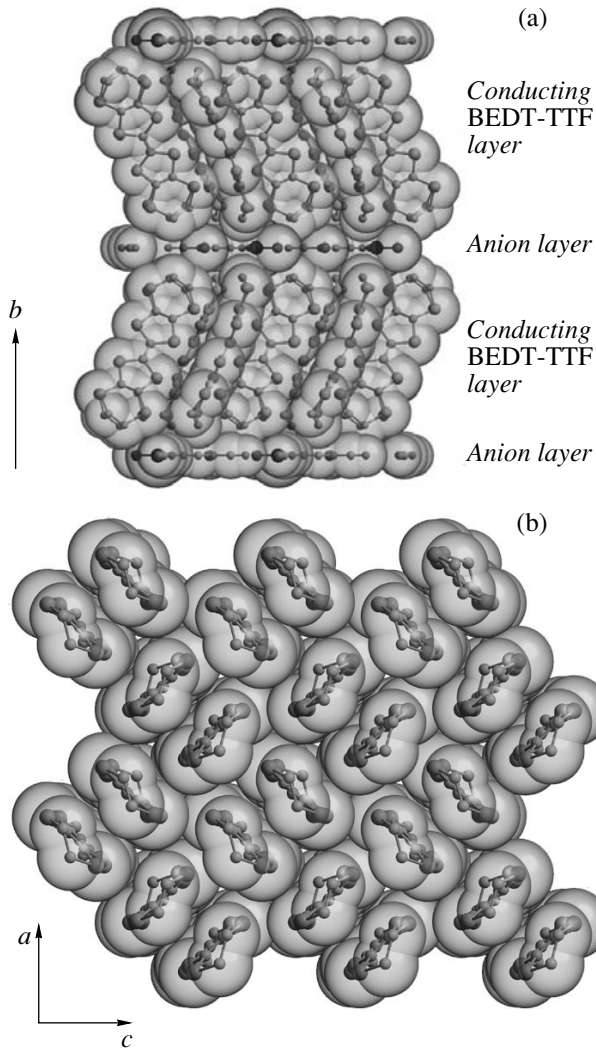
Fig. 1. Structure of κ-(BEDT-TTF)$_2$Cu[N(CN)$_2$]Cl crystals: (a) a view along the layers and (b) a conducting cation-radical layer.

In test experiments, the dynamic susceptibility at a frequency of 100 kHz was also studied.

The resistivity anisotropy (ρ_b/ρ_{ac}) calculated by the modified Montgomery method [14] was in the range 200–400 at $T = 300$ K for various samples and increased monotonically with decreasing temperature, reaching values of 1000–1400 at $T \approx 15$ K. The temperature dependence for both longitudinal and transverse resistances had a positive derivative in the entire temperature range below 300 K. A small region with a negative derivative occurred only at a low temperature in the vicinity of the superconducting transition and was more pronounced for a transverse resistance. We investigated several samples obtained in the course of one synthesis. The results obtained with different samples were similar. Given below are the results for one of them.

The dependence $R(T)$ obtained in the case of current passage along the conducting layers and the tempera-
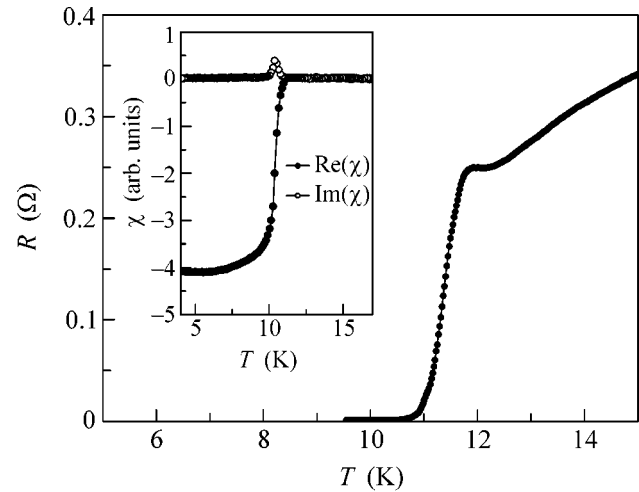

Fig. 2. Superconducting transition detected on a sample of κ'-(BEDT-TTF)$_2$Cu[N(CN)$_2$]Cl by the temperature dependences of the resistance and (inset) dynamic susceptibility.

ture dependence of the dynamic susceptibility at $T < 15$ K are presented in Fig. 2. It is evident in the figure that a transition to a superconducting state with the critical temperature $T_c = 11.5$ K determined by the middle of the transition is observed in the dependence $R(T)$. For the same sample, the transition detected by the dynamic susceptibility starts at approximately 11 K.

The application of a magnetic field led to a decrease in T_c; in this case, a considerable broadening of the superconducting transition occurred in the $J \parallel$ (ac) geometry while the transition at $J \perp$ (ac) did not broaden but displaced to the region of lower temperatures. For this reason, the dependences $H_{c2}(T)$ presented below were constructed by measuring the transverse resistance, that is, for the case when the current was passed along the normal direction to the conducting layers. The absence of a notable broadening in a magnetic field suggests that we are dealing with the dependence $H_{c2}(T)$ rather than with an "irreversibility line." In Fig. 3, the dependence $H_{c2}(T)$ is presented for two orientations of the magnetic field. All the points except one were obtained from the curves $R(T)$ at fixed values of the field H. The last point in the lower curve was obtained from the curve $R(H)$ at the fixed temperature $T = 1.2$ K. Attention is attracted by the positive curvature of the $H_{c2}(T)$ dependences and also by the fact that for $H \parallel b$ the derivative dH_{c2}/dT is close to zero at the point $T = T_c(0)$. For the case when the magnetic field lies in the (ac) plane, this derivative is finite and equal to $dH_{c2}/dT|_{T_c(0)} = -1.36$ T/K.

The main crystallographic data are as follows: rhombic (C$_{10}$H$_8$S$_8$)$_2$Cu[N(CN)$_2$]Cl crystals, sp. gr. *Pnma*, $a = 12.932(2)$ Å, $b = 29.877(5)$ Å, $c = 8.458(1)$ Å, $V = 3267.8(9)$ Å^3, and $Z = 4$. Experimental data for 4567 independent reflections with $I \geq 2\sigma(I)$ were
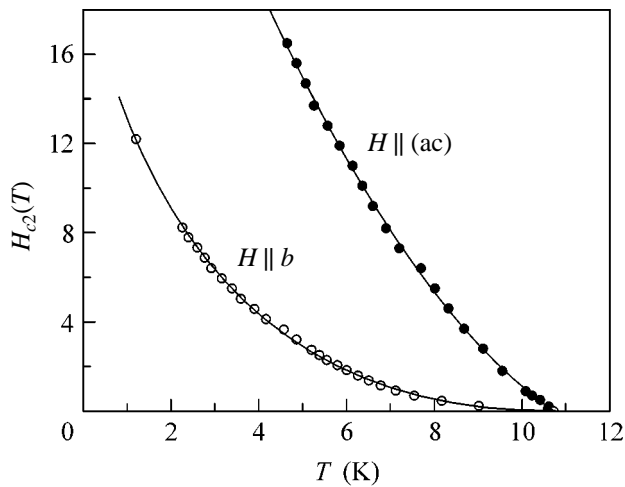
Fig. 3. Dependences $H_{c2}(T)$ for the magnetic field orientation in the plane of the conducting layers and along the normal to these layers.

obtained on an Enraf-Nonius CAD4 diffractometer (MoKa radiation, ω scan, $2\theta_{max} = 50°$, the size of the crystal was $0.5 \times 0.2 \times 0.02$ mm, absorption correction was introduced). The structure was determined by the direct method and was refined by the least-squares method in an anisotropic approximation to $R_1 = 0.056$. Crystals of the organic metal κ'-Cl exhibit almost the same structure as the Mott dielectric κ-Cl [4].

A preliminary analysis of the κ'-Cl crystal structure at room temperature showed the following differences between κ'-Cl and κ-Cl:

1. It is found that certain disorder exists at room temperature in κ-Cl crystals caused by the fact that the presence of two conformations (eclipsed and staggered) of terminal ethylene groups in the BEDT–TTF molecule is equiprobable. At a low temperature, these groups become fully ordered and the BEDT–TTF molecule assumes only the eclipsed conformation [15]. The ratio of the eclipsed and staggered conformations in κ'-Cl crystals equals 0.8 : 0.2; that is, the proportion of the eclipsed conformer, which is the conformer typical of the low-temperature state of κ-Cl crystals, is larger in the case of κ'-Cl crystals even at room temperature.

2. The volume of the unit cell in κ'-Cl crystals $V = 3267.8(9)$ Å^3 is smaller than that in κ-Cl crystals $V = 3299(1)$ Å^3 [4] and even smaller than the corresponding volume in the latter crystals $V = 3285.2(8)$ Å^3 under a pressure of 1.2 kbar [13]. Correspondingly, all the intermolecular S…S contacts in the conducting layer are shorter, which enhances intermolecular interactions and, as a consequence, increases the width of the conduction band. This effect is equivalent to chemical compression.

3. In the refinement of the structure, an incomplete occupation of the position of the copper atom was revealed (a deficit of ~5%) with the complete occupa-

tion of the positions of the other atoms. This may indirectly indicate that the anionic layer contains Cu^{2+} along with Cu^{1+}. Then, it might be suggested that the superconductivity of κ'-Cl crystals occurs through the doping of carriers into the κ-Cl Mott dielectric. A similar situation was observed in the case of the κ-(BEDT–TTF)$_2$Cu$_2$(CN)$_3$ cation-radical salt [16].

Subsequently, we plan to perform detailed synthetic, structural, and physical investigations with the aim of tracing the structure–property relationships and elucidating the nature of the superconducting state in these crystals.

REFERENCES

1. T. Ishiguro, K. Yamaji, and G. Saito, *Organic Superconductors*, Ed. by P. Fulde, 2nd ed. (Springer, Berlin, 1998), Springer Ser. Solid-State Sci., Vol. 88.
2. A. M. Kini, U. Geiser, H. H. Wang, *et al.*, Inorg. Chem. **29**, 2555 (1990).
3. H. H. Wang, K. D. Carlson, U. Geiser, *et al.*, Synth. Met. **41–43**, 1983 (1991).
4. J. M. Williams, A. M. Kini, H. H. Wang, *et al.*, Inorg. Chem. **29**, 3272 (1990).
5. R. P. Shibaeva, S. S. Khasanov, N. D. Kushch, *et al.*, in *Supramolecular Engineering of Synthetic Metallic Materials, Conductors and Magnets*, Ed. by J. Veciana, C. Rovira, and D. B. Amabilino (Kluwer Academic, Dordrecht, 1999), NATO ASI Ser., Ser. C, Vol. 518, p. 409.
6. N. D. Kushch, M. A. Tanatar, E. B. Yagubskii, and T. Ishiguro, JETP Lett. **73**, 429 (2001).
7. M. A. Tanatar, T. Ishiguro, S. Kagoshima, *et al.*, Phys. Rev. B **65**, 064516 (2002).
8. J. E. Schirber, D. L. Overmyer, K. D. Carlson, *et al.*, Phys. Rev. B **44**, 4666 (1991).
9. U. Welp, S. Fleshler, W. K. Kwok, *et al.*, Phys. Rev. Lett. **69**, 840 (1992).
10. H. Ito, T. Ishiguro, M. Kubota, and G. Saito, J. Phys. Soc. Jpn. **65**, 2987 (1996).
11. P. Limelette, P. Wzietek, S. Florens, *et al.*, Phys. Rev. Lett. **91**, 016401 (2003).
12. F. Kagawa, T. Itou, K. Miyagawa, and K. Kanoda, Phys. Rev. B **69**, 064511 (2004).
13. A. J. Schultz, U. Geiser, H. H. Wang, *et al.*, Physica C (Amsterdam) **208**, 277 (1993).
14. L. I. Buravov, Zh. Tekh. Fiz. **59** (4), 138 (1989) [Sov. Phys. Tech. Phys. **34**, 464 (1989)].
15. U. Geiser, A. J. Schultz, H. H. Wang, *et al.*, Physica C (Amsterdam) **174**, 475 (1991).
16. T. Komatsu, N. Matsukawa, T. Inoue, and G. Saito, J. Phys. Soc. Jpn. **65**, 1340 (1996).

Translated by A. Bagatur'yants

Phonon–Plasmon Coupled Modes in Hetero-Superlattices

L. A. Falkovsky[1] and E. G. Mishchenko[1, 2]

[1] *Landau Institute for Theoretical Physics, Russian Academy of Sciences, Moscow, 117334 Russia*
[2] *Department of Physics, University of Utah, Salt Lake City, UT 84112, USA*
Received May 26, 2005; in final form, June 20, 2005

The spectrum of coupled phonon–plasmon modes is considered in a mesoscopic system of thin conducting planes separated by insulating layers. The reflectance of such a sample in the infrared region is calculated. Reflectance minima are determined by the longitudinal and transverse phonon frequencies in the insulating interlayers and by the van Hove singularities of the coupled modes. Measuring the differential Raman cross section allows the spectrum of these modes to be found directly. © 2005 Pleiades Publishing, Inc.

PACS numbers: 63.20.–e, 78.30.–j

Longstanding interest in crystalline systems with artificially grown superlattices is caused, in particular, by their unusual electronic properties. Because the frequency of direct electronic transitions in the most popular GaAs-based material equals 1.5 eV, that is, lies in the optical region, the vast majority of experimental works are devoted to electronic and excitonic states just in this region (see, e.g., [1]).

However, Bose branches of the spectrum also exhibit unusual properties, which is due to the two-dimensional character of these systems [2]. Thus, their plasmon spectrum has no gap and must intersect optical phonon branches. This determines the strong interaction of phonon and plasmon branches. The properties of these branches are manifested most brightly in infrared optics in the range corresponding to the optical phonon frequency, that is, about 40 meV. These branches can also be studied in Raman scattering of laser radiation. Even though plasmon and coupled phonon–plasmon modes are observed in common Raman experiments [3], the same experiments with superlattices are unknown. An exception is provided by work [4], in which infrared transmittance was studied for a sample with a GaAs/AlAs superlattice in a magnetic field.

In this work, simple equations were obtained for the reflectance and the Raman cross section of a model periodic structure in which electronic layers can be considered as conducting planes that are thin as compared to both the thickness of the insulating interlayers and the electron wavelength. We assume here that charge carriers occupy only one of the subsurface quantization subbands (the effects of electron density smearing were discussed in [5]) and transitions to other subbands do not change the pattern under consideration significantly.

1. Spectrum of coupled phonon–plasmon modes. Now, consider a dielectric of the GaAs type in which parallel thin conducting planes are included at equal distances d. In practice, such planes are created by means of a GaAs/AlGaAs heterojunction. The dielectric contains two atoms per unit cell and, hence, two transverse optical modes with the frequency ω_{TO} at the center of the Brillouin zone and one longitudinal ω_{LO}. We will neglect the dispersion of these modes, because we are interested in wave vectors that are small as compared with the band sizes. In this case, the longitudinal component of the dielectric permittivity is expressed as

$$\varepsilon(\omega) = \varepsilon_\infty \frac{\omega_{LO}^2 - \omega^2 - i\omega\Gamma}{\omega_{TO}^2 - \omega^2 - i\omega\Gamma},$$

where the optical phonon width is of the order $\Gamma \sim 10^{-2}\omega_{LO}$.

The Maxwell equation for the system under consideration is written in the form

$$\mathrm{curl}\,\mathrm{curl}\,\mathbf{E} = \frac{\omega^2}{c^2}\varepsilon(\omega)\mathbf{E} + \frac{4\pi i\omega}{c^2}\mathbf{j}. \qquad (1)$$

Only the x component parallel to the layers exists for the current

$$j_x(\omega, k_x, z) = \frac{-i\alpha(\omega, k_x)\omega}{4\pi k_x}\sum_n \delta(z - nd)E_x(\omega, k_x, z),$$

and the E_x and E_z components exist for the field; it is assumed that the z axis is perpendicular to the layers. We consider the case of p polarization, when the field in the real space depends on the x and z coordinates; therefore, we expanded the current and the field into the Fourier integral with respect to the coordinate x.

The electronic polarizability of the layers $\alpha(\omega, k_x)$ can be calculated using either RPA [6] or, for $kv \ll \omega$ and $k \ll p_F$ (here, we will restrict ourselves to this case), the kinetic equation

$$\alpha(\omega, k_x) = -\kappa_0\varepsilon_\infty k_x v^2/\omega^2.$$

Here, $\kappa_0 = 2\pi e^2 v/\varepsilon_\infty$ is the screening length, v is the Fermi velocity, and $v = m/\pi$ is the density of states. The electron collision frequency γ can be taken into account qualitatively by the substitution $\omega \longrightarrow \omega + i\gamma$.

The Maxwell equation is rewritten for the x component of the field in the form

$$\left(\frac{d^2}{dz^2} - \kappa^2 - C\sum_n \delta(z - nd) \right) E_x(\omega, k_x, z) = 0, \quad (2)$$

where

$$C = \frac{\kappa^2 \alpha(\omega, k_x)}{k_x \varepsilon(\omega)}, \quad \kappa = \sqrt{k_x^2 - \omega^2 \varepsilon(\omega)/c^2}.$$

The two independent solutions of this differential equation can be written in the Bloch form

$$f_{1,2}(z) = e^{\pm ik_z nd} \{ \sinh \kappa(z - nd) \\ - e^{\mp ik_z d} \sinh \kappa[z - (n+1)d] \} \quad (3)$$

in the region $nd < z < (n+1)d$. The quasimomentum k_z is determined from the dispersion equation

$$\cos k_z d = \cosh \kappa d + \frac{C}{2\kappa} \sinh \kappa d, \quad (4)$$

and, for real parameters, it is sufficient to take its values from the half of the first Brillouin zone $0 < k_z < \pi/d$. Because we take into account phonon and electron attenuations, we fix the choice of the eigenfunctions in Eq. (3) by the condition $\mathrm{Im}\, k_z > 0$ so that f_1 decreases in the direction z.

The eigenfrequencies of the coupled phonon–plasmon modes are shown in Fig. 1 as a function of k_x for two fixed values $k_z = 0$ and π/d. We emphasize that it is evident in the figure that the point $k_z = k_x = 0$ is a saddle point: both eigenfrequencies in the vicinity of this point grow as functions of k_x and decrease with increasing k_z.

2. Reflectance from a lattice of heterojunctions. Let us calculate the reflectance for radiation incident from a vacuum on a semi-infinite system of layers. We will assume that the boundary of the sample is parallel to the layers and intersects the z axis at point z_0 lying between 0 and d. The field inside the sample must be described by the decreasing solution f_1 and the field outside the sample, by a sum of the incident and reflected waves with a fixed value of the wave vector k_x parallel to the layers. From the continuity condition for the tangent components of the electric and magnetic fields, we find that the reflectance

$$R = |A|^2 = \left| \frac{\kappa^2 Z - ik_z^i \varepsilon(\omega)}{\kappa^2 Z + ik_z^i \varepsilon(\omega)} \right|^2$$
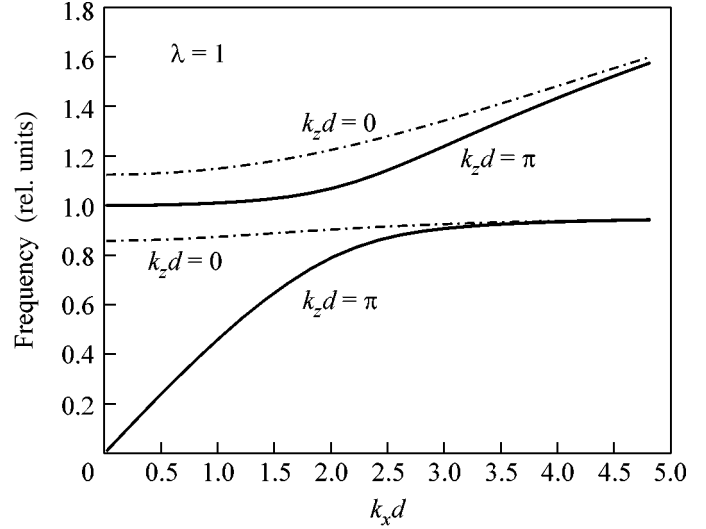
Fig. 1. Dispersion of phonon–plasmon coupled modes in a system of conducting planes separated by insulating interlayers; the phonon–plasmon coupling constant is selected as $\lambda = (\kappa_0 v^2/d)^{1/2}/\omega_{LO} = 1$. The frequency (in ω_{LO} units) is presented as a function of the wave vector k_x in the plane of layers at two values of the quasi-momentum k_z. The values of the parameters known for GaAs are used as follows: $\omega_{LO} = 36.5$ meV, $\omega_{TO} = 33.6$ meV, and $\kappa_0 = 2.5 \times 10^6$ cm^{-1}. The lattice period is taken as $d = 1/\kappa_0$.

is expressed through the impedance determined by the ratio of the filed and its derivative on the inner surface of the sample

$$Z = E_x(z_0+)/E_x'(z_0+),$$

k_z^i is the projection of the wave vector of the incident wave in a vacuum.

The solution f_1 in Eq. (3) gives

$$Z = f_1(z_0+)/f_1'(z_0+)$$

$$= \frac{\sinh \kappa z_0 - e^{-ik_z d} \sinh \kappa(z_0 - d)}{\kappa[\cosh \kappa z_0 - e^{-ik_z d} \cosh \kappa(z_0 - d)]}.$$

The calculated reflectance is shown in Figs. 2 and 3 for two lattices with different periods. The characteristic values of the parameter $\kappa \sim \omega_{LO}/c$ turn out to be small for the frequencies under consideration as compared to $1/d$. Therefore, the wavelength $\lambda \sim 2\pi/k_z$ is as large as compared to the lattice period. It is natural that the reflectance in this case is independent of the position of the sample boundary z_0. The reflectance for a sample without conducting planes is shown by a dot-and-dash curve, which exhibits a singularity at ω_{LO}. A similar dependence was observed in [7]. For $d = 1/\kappa_0$ and an intermediate electron concentration in the layer (dashed line), a sample with conducting planes turns out to be more transparent in two regions: at high fre-
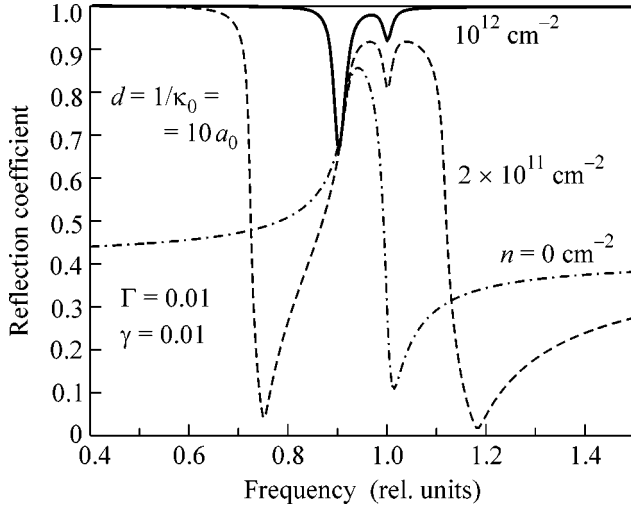
Fig. 2. Reflectance from the superlattice vs. the frequency (in ω_{LO} units) at the angle of incidence $\pi/4$. The electron concentration in the conducting heterojunction is indicated at the curves, the lattice period is taken as $d = 1/\kappa_0 = 4 \times 10^{-7}$ cm, Γ is the phonon width (in ω_{LO} units), and γ is the carrier relaxation frequency.
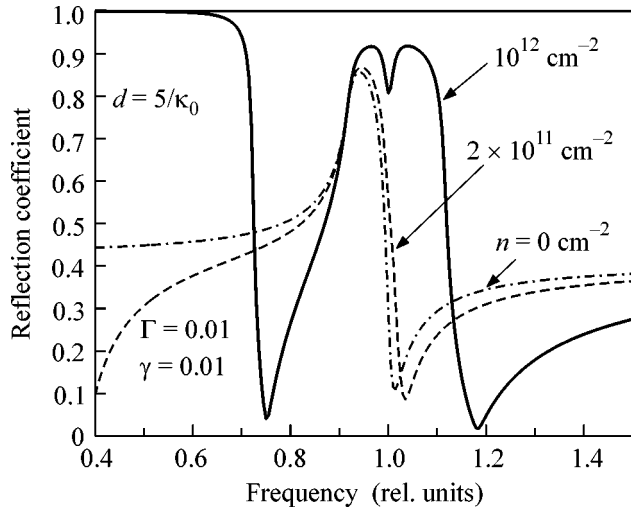

Fig. 3. Same as in Fig. 2, but for a larger lattice period.

quencies and below $\omega_{TO} = 0.9\omega_{LO}$. This is the effect of coupled modes, and the minima here correspond to saddle points of each mode. For a larger electron concentration (upper solid curve), the reflection is not total only in a narrow range restricted by the singularities at ω_{TO} and ω_{LO}. Finally, the reflectance at low frequencies tends to unity, because the skin depth grows and the sample acquires metallic properties. In a lattice with a large period $d = 5/\kappa_0$ (see Fig. 3), the effect of carriers is more pronounced at their larger concentration.

3. Raman scattering from a superlattice. Consider now the Raman scattering of radiation incident from a vacuum with the vector potential $\mathbf{A}^i$ and the wave vector $\mathbf{k}^i$. The corresponding quantities in the scattered wave will be designated as $\mathbf{A}^s$ and $\mathbf{k}^s$.

Besides these two fields, the longitudinal optical vibrations $\mathbf{u}$ in polar crystals are associated with the field $\mathbf{E}$ of the same frequency ω. These quantities ($\mathbf{u}$ and $\mathbf{E}$) describe plasmon and phonon excitations upon inelastic scattering and correspond to two tensor quantities g_{ijk}^u and g_{ijk}^E in the Hamiltonian of Raman scattering

$$\mathcal{H} = \int d^3 r \mathcal{N}_{jk}(t, \mathbf{r}) A_j^s(t, \mathbf{r}) A_k^i(t, \mathbf{r}). \qquad (5)$$

The operator

$$\mathcal{N}_{jk}(t, \mathbf{r}) = g_{ijk}^u \hat{u}_i(t, \mathbf{r}) + g_{ijk}^E E_i(t, \mathbf{r}) \qquad (6)$$

is linear with respect to the phonon and photon operators $\mathbf{u}$ and $\mathbf{E}$.

The scattering amplitude represents a matrix element of the Hamiltonian (5), and the cross section is given by its square averaged over the ground state. Here, it is most simple to use the fluctuation–dissipation theorem, according to which this average is expressed through the response of the system to a generalized force that is given by the product

$$A_j^s(\omega^s, k^s, z) A_k^i(\omega^i, k^i, z)$$
$$= U_{jk}(\omega = \omega^i - \omega^s, k = k^i - k^s, z) \sim e^{iq_z z},$$

where $q_z = k_z^i + k_z^s$. Terms proportional to this force appear in the equations of motion. For example, these terms arise in addition to the force from the field $E_i(w, k_x, z)$ in the equations

$$(-\omega^2 + \omega_{TO}^2 - i\omega\Gamma)u_i(\omega, k_x, z)$$
$$= \frac{Z}{\rho} E_i(\omega, k_x, z) - \frac{g_{ijk}^u}{\rho} U_{jk}(\omega, k_x, z) \qquad (7)$$

describing the phonon system; here, ρ is the density of the reduced mass and Z is the effective charge.

A similar term but with the vertex g_{ijk}^E also appears in the Maxwell equation (2). This equation can be substantially simplified in the case under consideration when k_x, k_z, and $q_z \sim \omega^i/c$ are determined by the frequency of the incident radiation and the imparted frequency is small $\omega \ll \omega^i$. By virtue of this fact, in the response calculations, we will neglect the terms ω/c compared to k and introduce the potential $\mathbf{E} = -\nabla\phi$. For the potential, we obtain Eq. (2), in the right-hand side of which a driving force arises

$$-4\pi i(k_x \tilde{g}_{xjk} + k_z \tilde{g}_{zjk}) U_{jk}(\omega, k_x, z),$$

where

$$\tilde{g}_{ijk} = g^E_{ijk} + \frac{g^u_{ijk}Z/\rho}{\omega^2_{TO} - \omega^2 - i\omega\Gamma}.$$

A solution of this equation is written using a Green's function $G(z, z')$

$$\phi(\omega, k_x, z) = -4\pi i(k_x\tilde{g}_{xjk} + k_z\tilde{g}_{zjk})$$

$$\times \int\limits_{z_0}^{\infty} dz' G(z, z')U_{jk}(\omega, k_x, z'), \qquad (8)$$

which is expressed in terms of solutions given by Eq. (3)

$$G(z, z') = \frac{i}{2\kappa\sin(k_z d)\sinh(\kappa d)}$$

$$\times \begin{cases} f_1(z)f_2(z'), & z > z' \\ f_2(z)f_1(z'), & z < z', \end{cases} \qquad (9)$$

and, in our approximation, $\kappa = k_x$.

Now, we will take into account that a third-rank tensor in a crystal with the T_d symmetry has only two independent components (in the crystal symmetry axes): g_{xxx} and g_{xyz}. Let the incident field propagate in the direction z and be polarized along x; the xz plane is the scattering plane. Then, the x component of the scattered field is excited (because of the g_{xxx} vertex) by phonon–plasmon vibrations also polarized in the direction x; scattering geometry (a). On the contrary, for the scattered field directed along the y axis, the vibrations along z are active (because of the g_{xyz} vertex). This is geometry (b). Thus, for the generalized susceptibility $\chi_{jk}(k_x, \omega, z, z')$ determined by the relationship

$$\langle \mathcal{N}_{jk}(\omega, k_x, z)\rangle = -\int\limits_{z_0}^{\infty} dz'\chi_{jk}(\omega, k_x, z, z')U_{jk}(\omega, k_x, z'),$$

an explicit expression is obtained with the use of Eqs. (6)–(9). To find the cross section, the susceptibility must be integrated over z and z' with the weight factor $U^*_{jk}(\omega, k_x, z)U_{jk}(\omega, k_x, z')$.

We present the final result for the most interesting case when the wavelength of the excited modes is large as compared to the period of the structure and small as compared to the sample size. In this case, only the main Bragg term is observed for each of the coupled modes. Its intensity in geometry (a) is proportional to

$$\text{Int}_{xx}(\omega, k_x) = \text{Im}\left\{ \frac{g^{u2}_{xxx}/\rho}{\omega^2_{TO} - \omega^2 - i\omega\Gamma}\right.$$

$$\left. + \left(g^E_{xxx} + \frac{g^u_{xxx}Z/\rho}{\omega^2_{TO} - \omega^2 - i\omega\Gamma}\right)^2 \frac{4\pi k^2_x}{(k^2_z - q^2_z)\varepsilon(\omega)}\right\} \qquad (10)$$
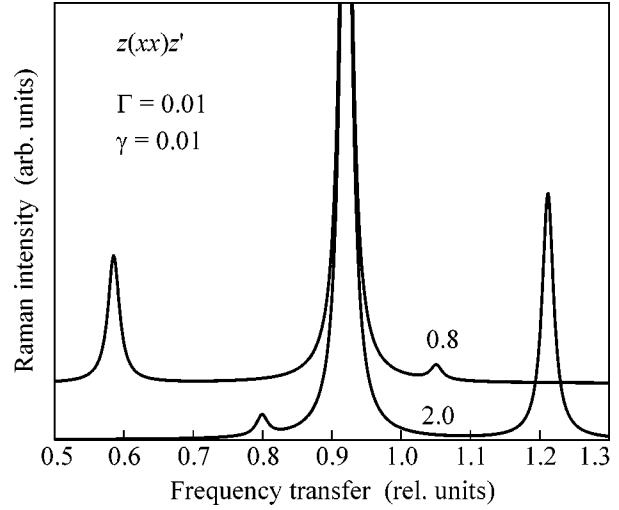
Fig. 4. Raman cross section vs. the frequency transfer (in ω_{LO} units) in the $z(xx)z'$ geometry for two values of the carrier concentration; z and z' are the propagation directions of the incident and scattered radiations, respectively; $.(xx).$ is their polarization; and the direction z' makes an angle of $\pi/4$ with the direction $-z$. The values of the other parameters are the same as in Fig. 1. The concentration n is indicated at the curves in units of 10^{11} cm^{-2}.

and shown in Fig. 4 for two values of the charge carrier concentration in the layer. The value of k_z must be taken from spectrum (4) at fixed values of the imparted frequency and the wave vector k_x determined by the scattering angles. For example, at normal incidence and the angle of scattered radiation θ, $k_x = \omega^i\sin\theta/c$ and $q_z = (\sqrt{\varepsilon(\omega^i)} + \sqrt{\varepsilon(\omega^i) - \sin^2\theta})\omega^i/c$. In Eq. (10), we dropped slowly varying factors depending on the properties of the incident and scattered radiations, for example, the depth of penetration into the sample and the temperature factor $1/[1 + \exp(-\omega/T)]$. The cross section for geometry (b) differs by the substitution of q_z for k_x and vertices g_{xyz} for g_{xxx}. It is shown in Fig. 5 for various values of the scattering angle from 0 (bottom) to $\pi/2$ (top) spaced at an interval of $\pi/10$. In the numerical calculations, we used the relationship between the vertices known from experiment and given by the Faust–Henry constant $K_{FH} = g^u Z/g^E\rho\omega^2_{TO} = -0.5$.

Note that, for the case of normal propagation of both incident and scattered radiation, $k_x = 0$, the second term in Eq. (10) vanishes and the Raman peak at parallel polarizations (geometry (a)) lies at ω_{TO}. The other peaks in Fig. 4 correspond to scattering with phonon–plasmon excitation. At the same time, at crossed polarizations (geometry (b)) and $k_x = 0$, Eq. (4) gives $k_z = ik_x$. Hence, using the equation for Int_{xy} and the relationship $\omega^2_{LO} - \omega^2_{TO} = 4\pi Z^2/\varepsilon_\infty\rho$, which relates the frequencies of the longitudinal and transverse phonons, we see that
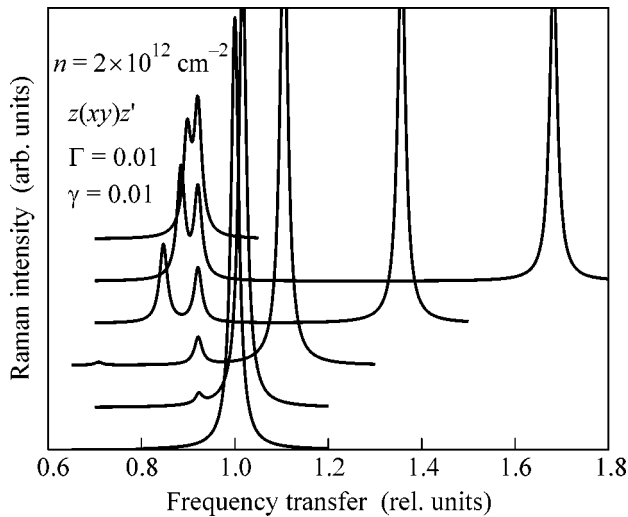
Fig. 5. Raman cross section vs. the frequency transfer (in ω_{LO} units) in the $z(xy)z'$ geometry for the angles of incidence varying from (bottom) 0 to (top) $\pi/2$ with a step of $\pi/10$.

the peak arises only at ω_{LO}, because the terms with a pole at ω_{TO} are cancelled. At different scattering angles, a peak appears at ω_{TO} (independently of the scattering angle). The two other peaks in each curve in Fig. 5 correspond to scattering with phonon–plasmon excitation.

In conclusion, we emphasize that the reflectance and the Raman cross section calculated in this work are very sensitive to both the carrier concentrations and the frequency parameters. Our results allow the corresponding experiment to be modeled.

REFERENCES

1. E. L. Ivchenko and G. E. Pikus, *Superlattices and Other Heterostructures: Symmetry and Optical Phenomena*, 2nd ed. (Springer, Berlin, 1997).

2. E. G. Mishchenko, M. Yu. Reizer, and L. I. Glazman, Phys. Rev. B **69**, 195302 (2004).

3. A. Mooradian and G. B. Wright, Phys. Rev. Lett. **16**, 999 (1966); A. Mooradian and A. L. McWhorter, Phys. Rev. Lett. **19**, 849 (1967).

4. C. Faugeras, G. Martinez, A. Riedel, *et al.*, Phys. Rev. Lett. **92**, 107403 (2004); Yu. Bychkov, C. Faugeras, and G. Martinez, Phys. Rev. B **70**, 085306 (2004).

5. V. L. Gurevich and K. E. Shtengel, Phys. Rev. B **44**, 8825 (1991).

6. S. Das Sarma and J. J. Quinn, Phys. Rev. B **25**, 7603 (1982); A. C. Tselis and J. J. Quinn, Phys. Rev. B **29**, 2021 (1984); Phys. Rev. B **29**, 3318 (1984).

7. W. Limmer, M. Glunk, S. Mascheck, *et al.*, Phys. Rev. B **66**, 205209 (2002).

Translated by A. Bagatur'yants